Improving the Capabilities of Swath Bathymetry Sidescan Using Transmit Beamforming and Pulse Coding

by

Marek Butowski

BASc, University of British Columbia, 2002

A Thesis Submitted in Partial Fulfillment of the
Requirements for the Degree of

Master of Applied Science

in the Department of Electrical and Computer Engineering

University of Victoria

Improving the Capabilities of Swath Bathymetry Sidescan Using Transmit Beamforming and Pulse Coding

by

Marek Butowski

BASc, University of British Columbia, 2002

Supervisory Committee

Dr. P. Kraeutner, Co-supervisor (Department of Electrical and Computer Engineering)

Dr. A. Zielinski, Co-supervisor (Department of Electrical and Computer Engineering)

Supervisory Committee

Dr. P. Kraeutner, Co-supervisor (Department of Electrical and Computer Engineering)

Dr. A. Zielinski, Co-supervisor (Department of Electrical and Computer Engineering)

Abstract

Swath bathymetry sidescan (SBS) sonar and the angle-of-arrival processing that underlies these systems has the capability to produce much higher resolution three dimensional imagery and bathymetry than traditional beamformed approaches. However, the performance of these high resolution systems is limited by signal-to-noise ratio (SNR) and they are also susceptible to multipath interference.

This thesis explores two methods for increasing SNR and mitigating multipath interference for SBS systems. The first, binary coded pulse transmission and pulse compression is shown to increase the SNR and in turn provide reduced angle variance in SBS systems. The second, transmit beamforming, and more specifically steering and shading, is shown to increase both acoustic power in the water and directivity of the transmitted acoustic radiation. The transmit beamforming benefits are achieved by making use of the 8-element linear angle-of-arrival array typical in SBS sonars, but previously not utilized for transmit.

Both simulations and real world SBS experiments are devised and conducted and it is shown that in practice pulse compression increases the SNR, and that transmit beamforming increases backscatter intensity and reduces the intensity of interfering multipaths.

The improvement in achievable SNR and the reduction in multipath interference provided by the contributions in this thesis further strengthens the importance of SBS systems and angle-of-arrival based processing, as an alternative to beamforming, in underwater three dimensional imaging and mapping.

Contents

List of Tables

List of Figures

List of Symbols

c	speed of sound in water
d	element spacing
k	acoustic wave number
λ	acoustic wavelength
M	number of solutions sought
N	number of array elements
θ	physical angle of arrival
ϕ	electrical phase
s_n	signal on element n
$\mathbf{S}$	sample matrix
τ_{01}	time delay
τ_P	pulse length
$\mathbf{w}$	null steering weigh vector

List of Abbreviations

ACF	auto-correlation function
AOA	angle-of-arrival
API	application processing interface
AWGN	additive white Gaussian noise
CAATI	computed angle-of-arrival transient imaging
ISL	integrated sidelobe level
LFM	linear frequency modulation
LPG	loss in processing gain
MF	merrit factor
OLS	ordinary least squares
PSL	peak sidelobe level
SARA	small aperture range and angle
SBS	swath bathymetry sidescan
SNR	signal-to-noise ratio
TLS	total least squares

Acknowledgements

First and foremost, I would like to thank my supervisors, Dr. Paul Kraeutner and Dr. Adam Zielinski, for providing advice, support, and encouragement during my time at UVic. They have been kind enough to patiently pass on their expertise, which has been invaluable to my academic development.

I would like to thank the Department of Electrical and Computer Engineering and the Department of Mechanical Engineering at UVic for partial funding support over the years. Thank you to Ping DSP Inc. for providing a sonar ideally suited to validating the proposed methods.

I've made many friends and had fantastic roommates for which I am grateful for they made my time at UVic very enjoyable and it flew by too quickly. Thank you to them for everything.

A big thank you to my girlfriend Victoria for being so supportive and to her family for devising clever incentives for getting me to write, and for providing a quiet working area away from home.

To my sister Joanne, you have been nothing but supportive throughout my entire life and even though you are younger I feel like you are the older sibling. Thank you!

To my mom Barbara, I would not be here if not for you. You alone brought us here to Canada, and even though money was always tight you supported me with my first soldering iron and my first computer. Thank you!

And last but not least, thank you to my aunts and uncles back in Poland, and especially to my uncle Darek who taught me to read resistor colour codes at a very young age.

Chapter 1

Introduction

SONAR is the underwater use of acoustic waves for the purpose of SOunding, NAvigation, and Ranging. The term was introduced in 1942 by F.V. Ted Hunt, the director of the Harvard Underwater Sound Laboratory, as a complement to radar and has since been widely adopted. It is now an umbrella term that includes the fields of underwater communication, imaging, bathymetry, and a multitude of means of underwater navigation.

Water, and even more so salt water, forms a challenging propagation environment where light scatters and absorbs quickly, and electromagnetic waves attenuate even more drastically. This has left scientists and engineers with sound as the preferred means for propagating energy and information in the underwater environment.

1.1 The Beginnings of Sonar

In 1822 on Lake Geneva, Jean-Daniel Colladon began the first experiments into underwater acoustics. He used an underwater bell and a listening device, each on a separate dingy a known distance apart, to measure the speed at which sound propagates in water. In these experiments, illustrated in Figure 1.1, Colladon was able to measure the speed of sound to be $1435\,\mathrm{m\,s^{-1}}$, a measurement only $4\,\mathrm{m\,s^{-1}}$

Figure 1.1: Illustration of Daniel Colladon's experiments to determine speed of sound in water. [2]

from the nominal accepted value for his experimental conditions.[1]

Although this was pioneering work, the first application of underwater sound did not come until 1902 when the *Submarine Signal Company* of Boston produced a crude navigation system. Similar to Colladon's apparatus, this system featured a pneumatic bell to generate sound; however, the electronic advances of the previous 80 years allowed for the sound to be received by underwater microphones. A ship was equipped with two microphones, one on each bow, which would listen for a bell struck on another ship. The listener would alternate between the port and starboard microphones and could roughly estimate the bearing to the signalling ship [3]. The low frequency of the bell made operation difficult as it was interfered with by various ship noises, and the system was ultimately abandoned.

At this point sonar was in its infancy and it would take two events to spark the need, interest, and funding required for the development of early sonar systems: the sinking of the Titanic in 1912 by an iceberg and the increased U-boat threat faced by the allies in World War I. In 1913, a Canadian, Reginald Fessenden, a consultant

---

[1] Nominal speed of sound in fresh water at 8 °C is $1439\,\mathrm{m\,s^{-1}}$ [1].

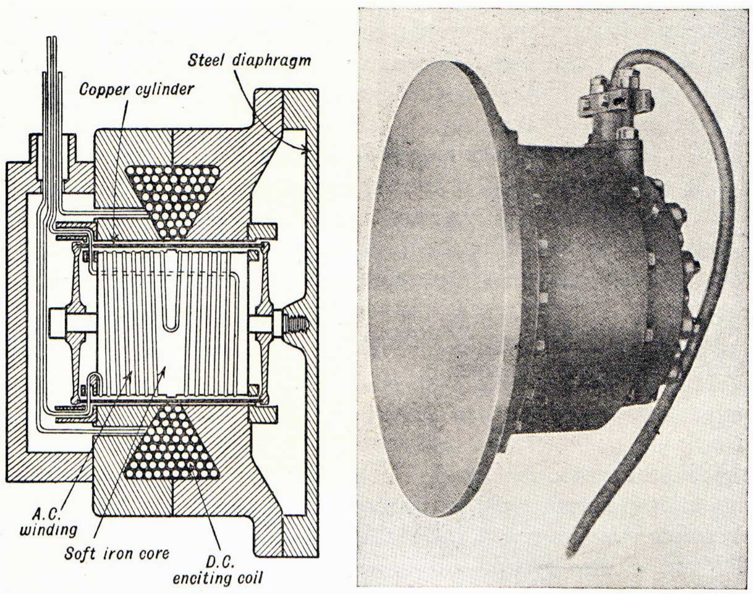

Figure 1.2: The Fessenden Oscillator: The earliest underwater transducer. [5]

for the *Submarine Signal Company* (SSC), invented the first underwater acoustic transducer [4]. A transducer is a device capable of both generating underwater sound, and listening to the resulting echoes by converting electrical energy to acoustic and vice versa.

Known as the Fessenden oscillator, the transducer was an electrodynamically driven circular plate that operated at 540 Hz and had a diameter of 75 cm [4]. In 1913, Fessenden and other SSC engineers demonstrated the use of the oscillator as an underwater telegraph; the team transmitted Morse messages between two tugboats several miles apart in the Boston Harbor. A year later off the coast of Newfoundland, Fessenden and two SSC engineers spent several days aboard the US Revenue Cutter Miami and demonstrated that the oscillator could determine the range to an iceberg 3.2 km away, and that it could be used to measure depth. During these trials they energized the oscillator for a fraction of a second, then reversed its operation to use it as a microphone, listened to the echo, and determined the time of flight using a stopwatch [4, 6]. The system was not capable of determining the bearing to the iceberg due to its small size relative to the wavelength it operated at; the Fessenden oscillator was omnidirectional [7]. Fessenden had trouble convincing SSC to pursue echo ranging, and instead SSC chose to use the oscillator as an underwater telegraph.

The French Physicist, Paul Langevin, took the next revolutionary step in underwater detection. In his development of "echo location to detect submarines", he invented the first transducer which used the piezoelectric effect. It was 20cm across and used 4mm thick piezoelectric quartz sandwiched between two 3cm steel plates; the transducer resonated at approximately 40kHz [3, 8]. The much higher frequency and similar size of Langevin's transducer meant it was directional and this allowed a bearing to be determined from the direction in which the transducer was pointed. A second key contribution from Langevin was his receiver which included a valve or tube amplifier. The amplifier was required because of the much lower return signal level generated by the quartz transducer [7]. In 1918, in cooperation with the French Navy, a prototype system was successfully demonstrated in the waters off Toulon. It was able to determine both range and bearing to a target up to a distance of several hundred feet according to [3, 6] or even more than 600 metres according to [8].

Sonar arrived too late to have an impact in World War I, but did result in the creation of a combined British and French effort to develop sonar systems coined ASDIC, an acronym for Allied Submarine Detection Investigation Committee. This effort added the expertise of British and American scientists who had thus far been primarily concentrating on passive detection through the use of underwater microphones, an effort plagued by self-noise and an inability to determine range. After the war, SSC continued to concentrate on the underwater telegraph using the Fessenden oscillator, while the British and French co-operation focused on further development of quartz transducer based systems. In the early 1920s sonars, now known as ASDICs, were developed and operated over the frequency range of 20 to 50 kHz. In 1924, after several other depth sounders were demonstrated, SSC produced the "Fathometer", an early depth sounder that used the Fessenden oscillator to generate an acoustic

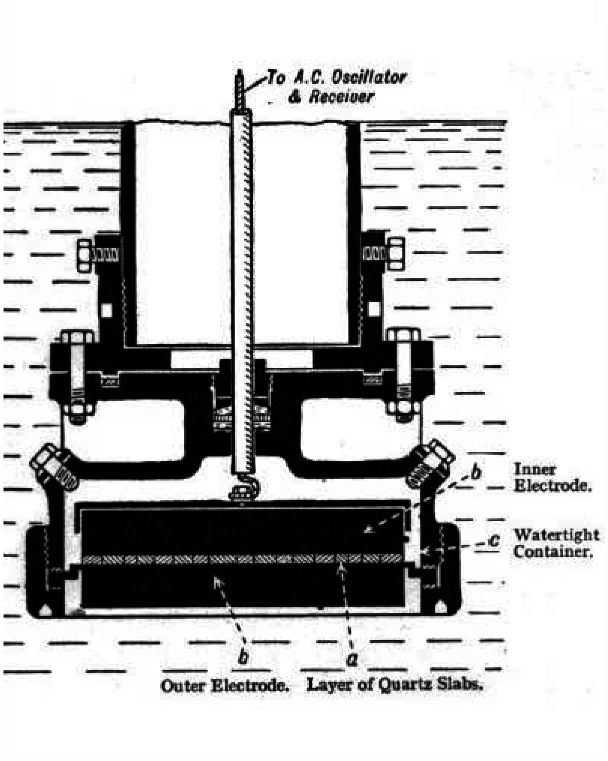

Figure 1.3: Langevin's Quartz Transducer: The first underwater transducer to use the piezoelectric effect. [9]

wave and a button type microphone for receiving [3].

Early in the 1930s, quartz was replaced by Rochelle Salt Crystals which were more sensitive [3]. World War II saw the use of flat faced arrays, operating at 20kHz or below and installed in spherical housings that were mechanically steered in azimuth to determine the bearing to the target.

1.2 The History of Commercial Sidescan

The need to detect submarines during World War 2 led to the further development of ASDICs and defence technologies that paved the way for sidescan sonar. The late 1950s and early 1960s saw the first academic description and application of what is now known as sidescan sonar.

Sidescan uses a linear element with a fan shaped directional response as opposed to the omnidirectional response of the Fessenden transducer or the conical response of Langevin's transducer. The transducer is driven to produce a burst of acoustic waves in the water, which propagate, hit a target, and scatter. Some of this acoustic energy, called *backscatter*, makes it back to the sonar, and its intensity is plotted against time. The sidescan sonar is then moved forward, typically the vessel on which it is mounted is in forward motion, and the process is repeated. This repeated process generates a 2D intensity image across a swath extending to either side of the vessel.

An academic sidescan sonar was first described in [10] and used aboard the RRS Discovery II to conduct a sea-floor survey near Plymouth in April 1958. The sonar operated at a frequency of 37 kHz and had a beamwidth of 1.8° alongtrack and 11° crosstrack with multiple sidelobes. The results of this survey were published in [11] and showed the first sidescan image. Although the image lacked any significant bottom features it showed innovation in how it presented sea floor backscatter.

The Kelvin-Hughes Transit Sonar was the first commercially developed sidescan sonar. It was a one sided, single channel, pole mounted unit introduced in the early 1960s [12]. Beginning in 1953 Professor Harold (Doc) Edgerton at the Massachusetts Institute of Technology (MIT) began experimenting with sonar and in 1960 was a co-author of the first US publication which discussed sidescan sonar [13]. Doc Edgerton previously founded Edgerton, Germeshausen & Grier with two MIT graduate students, a company who's Marine Instruments division would go on to become EdgeTech, which is still one of the predominant sidescan companies. Between 1963 and 1966, EG&G developed the first commercial dual channel sidescan, which imaged both port and starboard, and was enclosed in a water tight housing with fins to be towed behind a vessel. The whole assembly was aptly named a tow-fish. The lead designer for this first system was Martin Klein, an MIT student, who worked at Doc Edgerton's MIT lab and later at EG&G. These early EG&G sidescans were used to

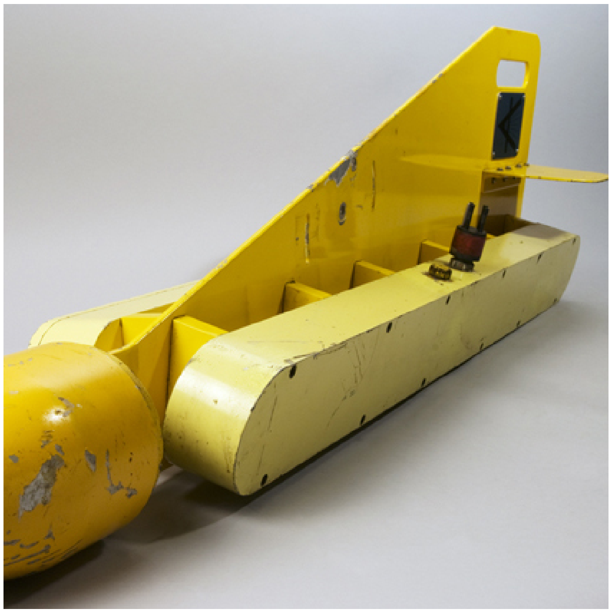

Figure 1.4: A 1970s Klein Associates Inc model MK-300 tow-fish sidescan sonar. [14]

accomplish a number of impressive feats including locating the 16th century carrack HMS Mary Rose. EG&G sidescans were also used in the search for the lost U.S. Navy nuclear submarine USS Thresher [14]. Martin Klein left EG&G in 1968 to form Klein Associates Inc, a company dedicated to the new commercial field of high frequency sidescan sonar. Starting out in his basement, Klein produced the model MK-300 sidescan in 1970, seen in Figure 1.4, which operated at 50 kHz. In 1975, two War of 1812 ships, the Hamilton and Scourge, were found in Lake Ontario using the MK-300 [14].

Both EG&G and Klein would go on to further develop modern sidescan with innovations such as narrowed alongtrack beamwidth to under 0.5°, increased frequency to achieve high crosstrack resolution, and dual simultaneous frequency operation. Further development of sidescan, first pursued academically and then commercially, was the development of a bathymetric capability to augment the 2D sidescan image.

1.3 Development of Swath Bathymetric Sidescan

In [15], the author Denbigh proposed a novel system which featured two parallel linear elements. The electrical phase difference of the received signal between these two elements could be used to determine the physical angle from which the acoustic backscatter originated; a method termed *interferometry*. The first interferometric system of this type was designed and demonstrated by Denbigh, and featured two elements spaced 3λ apart, where λ is the acoustic wavelength, and an element width of slightly less than 3λ each. An independent transmit array was operated at 410 kHz [16, 17]. While the large spacing made this transducer easier to prototype, it had the negative side effect of ambiguous measurements at angles greater than ±9.6° from broadside [18]. Denbigh somewhat alleviated this problem through the use of a baffle designed to prevent arrivals from directions that produce ambiguous solutions. His Mark II system reduced the spacing between elements to 1.1λ with an element width of 0.7λ. This had the effect of increasing the unambiguous arrival sector to ±27°.

Besides Denbigh's academic system, several others were also developed. In 1982, the Continental Shelf Institute (IKU) in Norway developed a 160 kHz interferometric sonar with two elements spaced by 2λ. The IKU sonar, coined TOPO-SSS, was integrated into a tow-fish which was capable of measuring its inertial position, specifically depth, roll and yaw. This allowed the sonar to correct for motion, of which roll was the most influential. Another system of interest, developed at the University of Bath, used three regular sidescan linear transducers designed to operate at 303 kHz and create a beam 1° by 50°. The three transducers were placed at 13λ and 14λ wavelengths apart, creating a total baseline of 27λ. The system cleverly used the slightly different spacing between the two sets of elements to reduce the ambiguity to that of a 1λ spaced transducer, while maintaining the fine resolution of a widely space pair [19].

The mid 1980s saw the introduction of several commercial systems one of which was a spin-off from the University of Bath. The Bathyscan 300, produced by Bathymetrics Ltd, was a reduced baseline version of the Bath system with a spacing of 10λ and 11λ [17]. At the same time, International Submarine Technology Ltd introduced a low frequency, 11 kHz for the port side and 12 kHz for starboard, interferometric system called SeaMARC II. The system featured two linear elements spaced by $\lambda/2$ and a 2° by 45° beamwidth [20].

1.4 Beyond Interferometry

A major limitation of interferometry is its reliance on there being only a single arrival at any one time; if multiple simultaneous arrivals from differing directions are seen on the same interferometric pair of elements their phase difference becomes meaningless and interferometry breaks down. To address just this issue Kraeutner and Bird extended interferometry with addition of more linear array elements to solve for multiple arrivals [21]. Their method, *Computed Angle-of-Arrival Transient Imaging* (CAATI), uses N linear elements to solve for up to $N-1$ plane-wave arrival angles and amplitudes, and in the very simplest case of $N=2$ simplifies to interferometry [22].

Kraeutner and Bird created an experimental prototype *Small Aperture Range and Angle* (SARA) sonar which featured six 40λ long elements, spaced 0.7λ apart, and operated at 300 kHz. The SARA sonar was used in a set of tank experiments to validate the CAATI method, and then further tested at Loon Lake in British Columbia to qualitatively evaluate the performance of CAATI when applied to a real sea-bottom return [23]. The results were promising and CAATI was patented in October 2000 [24].

This work paved the way for the first commercial multi-element SBS sonar the

Benthos C3D. Similar to the SARA sonar, the C3D uses six $\sim 40\lambda$ elements, however it operates at 200 kHz. The 3DSS-DX-450 was recently introduced by Ping DSP Inc and it features eight $\sim 95\lambda$ elements, operates at 450 kHz, and can solve for up-to four simultaneous arrivals. The system features modern electronics, flexible hardware, and CAATI processing which make it the current state-of-the-art in the commercial SBS world.

1.5 Summary of Thesis

SBS sonars, both interferometric and CAATI[2], are becoming important underwater imaging and mapping tools especially in shallow water where other systems such as multibeam sonars lack efficient swath coverage. Performance of SBS sonars is largely governed by *signal to noise ratio* (SNR) and multipath interference.

In this thesis the two primary avenues of investigation are the improvement of SNR through pulse compression, and the reduction of multipath interference through transmit beam shaping and steering.

The thesis is organized into nine chapters. In Chapter 1, this chapter, the history of the development of sonar, sidescan sonar, and SBS sonar has been presented. In Chapter 2, the mathematics behind interferometry and CAATI are presented. In Chapter 3, the effect of SNR on the variance of angles computed by interferometry and CAATI is simulated and reported. Chapters 4 and 7 present and experimentally verify pulse compression as a means for improving SNR. Chapters 5 and 8 present and experimentally verify transmit beam shaping and steering as a means for improving signal strength and reducing multipath. Chapter 6 describes the prototype SBS sonar used in the experiments conducted in this thesis. Chapter 9 ends the thesis with an example of 3D imagery produced by the prototype SBS sonar, and final conclusions.

---

[2] The terms CAATI and Angle-Of-Arrival (AOA) will be used interchangeably in this thesis.

Chapter 2

Mathematics of Swath Bathymetry Sidescan

Sidescan systems use a transmit waveform that is a simple gated sinusoid several cycles in length at the transducer's resonant frequency. Let $s_t(t)$ be a complex formulation of this transmit waveform,

$$s_t\left(t\right) = \mathrm{rect}\left(\frac{t}{\tau_p}\right) \exp\left(\jmath \omega t\right) \tag{2.1}$$

where τ_p is the length of the pulse, ω is the transducer's resonant frequency, and rect is defined as:

$$\mathrm{rect}(t) = \begin{cases} 1 & \text{for } |t| < \frac{1}{2} \\ \frac{1}{2} & \text{for } |t| = \frac{1}{2} \\ 0 & \text{otherwise} \end{cases} \tag{2.2}$$

As mentioned in the previous chapter, this transmit wave propagates through the water, scatters off a target, and returns to the sidescan sonar. Interferometric sonar utilizes two array elements to receive this signal.

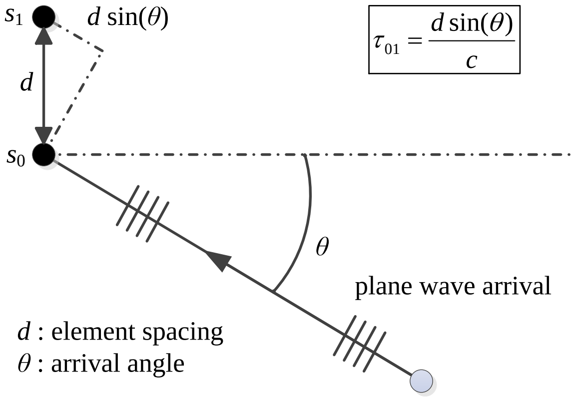

Figure 2.1: The geometry of a single plane wave arrival received on two array elements.

2.1 Interferometric Sonar

Interferometric sonar samples the output of two parallel linear elements spaced a distance, d, apart. At each sample time interferometry makes two assumptions:

1. The signal across the array is the result of a single plane wave arrival from an unknown angle θ, this assumption is referred to as the plane wave assumption.
2. The arrival fully envelopes the two receive elements, referred to as the steady state assumption.

Furthermore, the signal received at the first element, $s_0(t)$, and the signal received at the second element, $s_1(t)$, are time delayed versions of each other, where the delay depends on θ. An illustration of this relationship is shown in Figure 2.1.

From the steady state assumption the signal at the first element can be expressed as

$$s_0(t) = \exp\left(\jmath \omega t\right) \tag{2.3}$$

and the signal at the second element is then

$$s_1(t) = \exp\left(\jmath\,\omega(t - \tau_{01})\right) \tag{2.4}$$

where τ_{01} is the delay between the signal arriving at s_0 and s_1. By examining Figure 2.1 and applying trigonometry with the plane wave assumption (assumption 1), the delay can be expressed as

$$\tau_{01} = \frac{d}{c}\sin\theta \tag{2.5}$$

where c is the speed of sound in water.

The above equations may then be combined to give the phase difference, ϕ_{01}, between $s_0(t)$ and $s_1(t)$:

$$\begin{align}
\phi_{01} &= \arg\left(s_0(t)\, s_1^*(t)\right) \tag{2.6}\\
&= \arg\left(\exp\left(\frac{\jmath\omega d}{c}\sin\theta\right)\right) \tag{2.7}\\
&= \frac{\omega d}{c}\sin\theta \tag{2.8}\\
&= \frac{2\pi d}{\lambda}\sin\theta \tag{2.9}
\end{align}$$

This phase difference is measured across the two elements and can then be used to determine θ provided that d is sufficiently small to ensure uniqueness.

2.1.1 Half Wavelength Interferometry

To ensure an unambiguous solution for arrival angles between −90° and 90°, d is set to:

$$d = \frac{\lambda}{2} \tag{2.10}$$

This assignment very conveniently simplifies ϕ_{01}:

$$\phi_{01} = \frac{\omega\lambda}{2c}\sin\theta \tag{2.11}$$

$$= \pi\sin\theta \tag{2.12}$$

Therefore, for the assumed plane wave arrival the electrical phase difference between the two elements is the result of an arrival from the θ direction (2.12) which can be determined as:

$$\theta = \sin^{-1}\left(\frac{\phi_{01}}{\pi}\right) \tag{2.13}$$

Element spacings larger than $\lambda/2$ produce ambiguous results, and in these cases signals must be prevented from arriving from angles that are ambiguous. One approach that has been used previously is to narrow the response of each element. Another approach is to use a baffle to prevent sound from impinging on the transducer from unwanted angles. Figure 2.2 shows the relationship between the electrical phase difference seen between two elements and the angle of the plane wave arrival for three different element spacings.

Using three elements, one can get a coarse but unambiguous angle estimate using a $\lambda/2$ spacing, and a fine but ambiguous estimate using a spacing of several λ.

2.1.2 Vernier Interferometry

In vernier interferometry three elements are spaced by $n\lambda$ and $(n+\alpha)\,\lambda$ forming a $(2n+\alpha)\,\lambda$ baseline [19]. Independently both phase differences are ambiguous, however when subtracted they form an $\alpha\lambda$ vernier which is less ambiguous, or completely unambiguous if $\alpha \leq 0.5$.

Shown in Figure 2.3, is the 1λ vernier used in the Bathyscan-300. The resulting

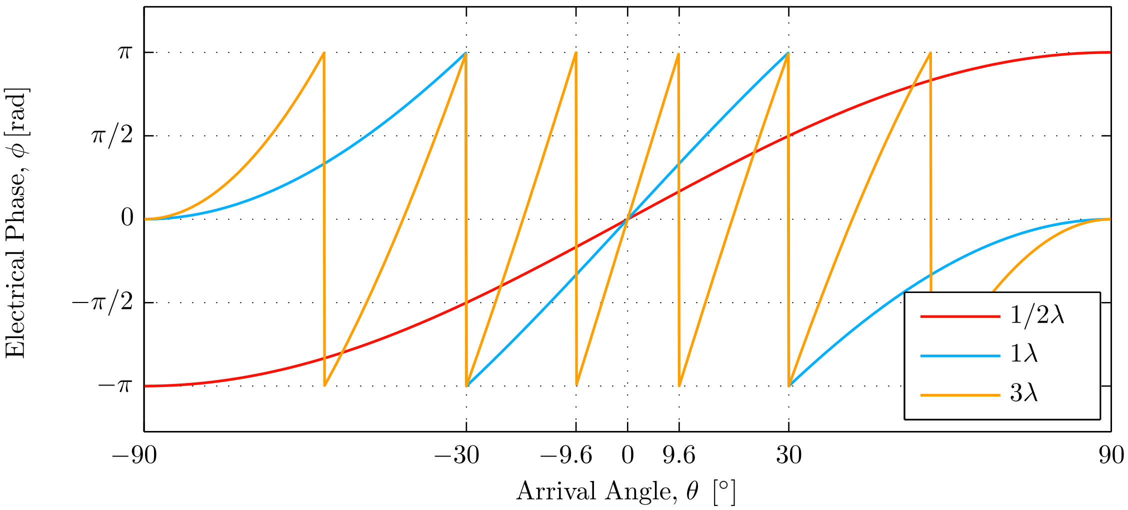

Figure 2.2: Interferometric arrival angle versus electrical phase difference relationship for several element spacings.

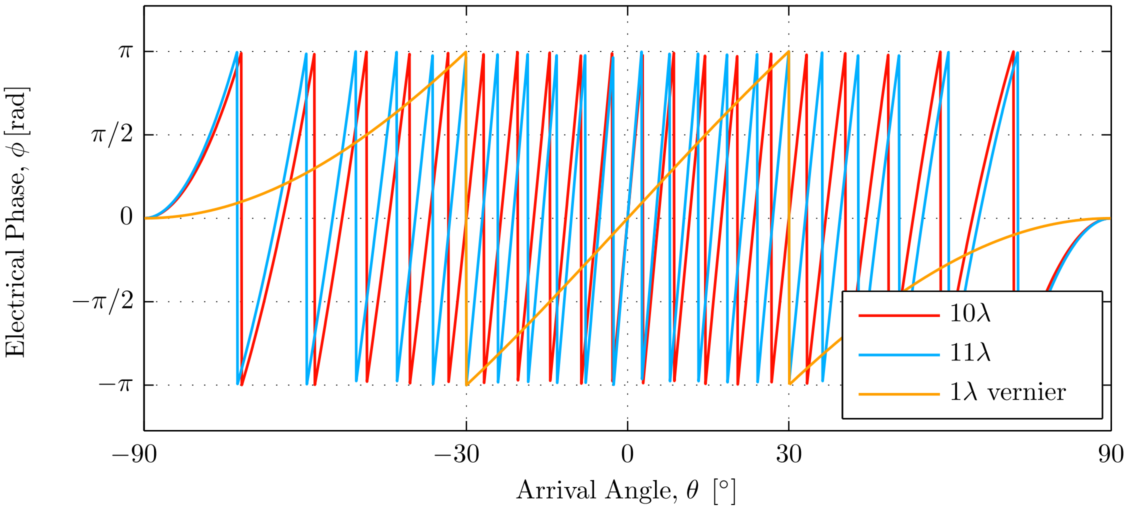

Figure 2.3: Electrical phase difference relationship for the Bathyscan-300 10λ and 11λ element spacing.

interferometric measurement is unambiguous if a baffle is used to suppress arrivals from outside of ±30° or the response of an individual element is limited significantly, for example by $-20\,\mathrm{dB}$ outside ±30°.

2.1.3 Interferometry Expressed As Null Steering

Interferometry can also be expressed in a null steering formulation. Given two complex sampled element signals, s_0 and s_1, and assuming one plane wave arrival, it is possible to find a complex set of weights, w_0 and w_1, which null the output of the array:

$$s_0 w_0 + s_1 w_1 = 0 \tag{2.14}$$

To remove the trivial solution of $w_0 = w_1 = 0$, the first weight is set to a nominal value of 1, $w_0 = 1$. Equation (2.14) can then be re-arranged to obtain a solution for w_1:

$$w_1 = \frac{-s_0}{s_1} \tag{2.15}$$

The signals s_0 and s_1 result from a plane wave arrival and this can be modelled in a general phase form as $s_n = \exp\left(-\jmath n \pi \sin\theta\right)$ at each element $n = 0 \ldots 1$. This form can also be expressed as

$$s_n = z^{-n} \tag{2.16}$$

an exponential form where:

$$z = \exp\left(\jmath \pi \sin\theta\right) = \exp\left(\jmath \phi\right) \tag{2.17}$$

To find the angle of arrival θ, (2.18) is formed from (2.14) - (2.17) and solved:

$$w_0 z^0 + w_1 z^{-1} = 0 \tag{2.18}$$

$$1 + w_1 z^{-1} = 0 \tag{2.19}$$

Re-arranging (2.19) and substituting (2.15), the following is obtained:

$$z = -w_1 \tag{2.20}$$

$$\exp\left(\jmath\phi\right) = \frac{s_0}{s_1} \tag{2.21}$$

Taking the complex argument of both sides reveals the interferometric equation:

$$\phi = \arg\left(\frac{s_0}{s_1}\right) \tag{2.22}$$

$$\theta = \sin^{-1}\left(\frac{\phi}{\pi}\right) \tag{2.23}$$

The polynomial z representation of a plane wave arrival was briefly introduced above to lay the ground work for solving for an arbitrary number of arrivals.

2.2 Angle Of Arrival

One of the most significant problems for interferometric systems is the arrival of more than one plane wave at the same instance in time. Interferometry breaks down for more than one arrival, however a solution has been proposed by [23] in which additional array elements are used to solve for multiple concurrent arrivals. The approach is based on the null steering equation

$$\sum_{n=0}^{N-1} w_n s_n = 0 \tag{2.24}$$

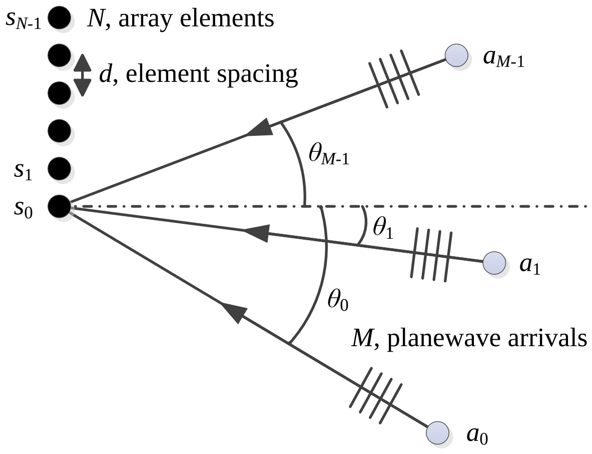

Figure 2.4: Illustration of plane wave model for an N element array and M arrivals.

where s_n is the receive response at each element in the N element linear array shown in Figure 2.4 and w_n are unknown weights used to null the response of the array. Equation (2.24) is a generalization of (2.14). Assuming that a set of weights can be found to satisfy (2.24), consider first the problem of using the weights to find the unknown angles of arrival.

For M incident plane waves of intensity a_m arriving from angles θ_m where $m = 0 \ldots M-1$, the response at each element s_n can be expressed as

$$s_n = \sum_{m=0}^{M-1} a_m \exp\left(-\jmath n \phi_m\right) \tag{2.25}$$

which is similar to equations (2.3) and (2.4) with the number of plane wave arrivals generalized to M and number of array elements generalized to N. In (2.25) ϕ_m is the phase progression caused by the m-th plane wave, and can be computed as

$$\phi_m \quad = \quad kd \sin\theta_m \tag{2.26}$$

where k is the wave number at the acoustic carrier frequency, and d is the element spacing. Then combining (2.24) and (2.25)

$$\sum_{n=0}^{N-1} w_n \sum_{m=0}^{M-1} a_m \exp\left(-\jmath n \phi_m\right) = 0 \tag{2.27}$$

which can be rearranged as

$$\sum_{m=0}^{M-1} a_m \sum_{n=0}^{N-1} w_n \exp\left(-\jmath n \phi_m\right) = 0 \tag{2.28}$$

and finally making the substitution $z_m = \exp\left(\jmath \phi_m\right)$:

$$\sum_{m=0}^{M-1} a_m \sum_{n=0}^{N-1} w_n z^{-n} = 0 \tag{2.29}$$

A realization is now made that the second summation is the same as the definition of the unilateral $\mathcal{Z}$ transform of the weights, w_n:

$$W(z) = \mathcal{Z}\left\{w_n\right\} = \sum_{n=0}^{N-1} w_n \, z^{-n} \tag{2.30}$$

Thus (2.29) can be simplified through the $\mathcal{Z}$ transform of the weights, $W(z)$, which forms a polynomial of order $N-1$:

$$\sum_{m=0}^{M-1} a_m W(z) = 0 \tag{2.31}$$

The polynomial $W(z)$ has $N-1$ complex roots, and substituting any of these roots for z will satisfy (2.31) and the null steering equation regardless of the value of a_m. Each of these roots corresponds to a value for z_m which can be used with $z_m = \exp\left(\jmath \phi_m\right)$ to get ϕ_m and ultimately θ_m.

Thus the null steering equation (2.24) for plane wave arrivals can be interpreted as the $\mathcal{Z}$ transform of the steering weights equated to zero (2.31). Furthermore, the roots of the polynomial in z each represent a linear phase progression across the elements due to a plane wave arrival. The remaining challenge therefore is to determine the null steering weights, w_n which form the $W(z)$ polynomial.

2.2.1 Fully Constrained Null Steering Solution

The solution presented in this section uses the minimum number of array elements necessary to solve for M plane wave arrivals. The solution steers the same nulls, using the same weights w_n, across multiple sub-arrays to satisfy the requirement for sufficient independent equations. Consider the case of two plane wave arrivals (i.e. $M = 2$) as seen by a three element array with element responses s_0, s_1, and s_2.

Applying the null steering equation (2.24) and setting the first weight to 1 (i.e. $w_0 = 1$) to remove the trivial solution (i.e. $w_n = 0$ for all n) yields:

$$1s_0 + w_1 s_1 + w_2 s_2 = 0 \tag{2.32}$$

Thus the result is one linear equation with two unknowns and the system is underdetermined. Next add a fourth element, s_3. Since the arrivals are assumed to be plane waves and the array is assumed to be in steady state, the same set of weights can be used to null out the staggered array defined by s_1, s_2, and s_3:

$$1s_1 + w_1 s_2 + w_2 s_3 = 0 \tag{2.33}$$

With the addition of a fourth element, the two smaller three element sub-arrays provide two independent linear equations and two unknowns, hence a unique solution for the weights can be obtained. The two equations are formed from two overlapping sub-arrays, $[s_0\, s_1\, s_2]$ and $[s_1\, s_2\, s_3]$, derived from the larger four element array, $[s_0\, s_1\, s_2\, s_3]$. This method of adding more elements to obtain more equations in order to produce a unique solution for the null steering weights is called the sub-array method.

A matrix formulation of the sub-array method is

$$\mathbf{S}\mathbf{w} = 0 \tag{2.34}$$

where

$$\mathbf{S} = \begin{bmatrix} s_0 & s_1 & s_2 & \cdots & s_M \\ s_1 & s_2 & s_3 & \cdots & s_{M+1} \\ \vdots & \vdots & \vdots & \ddots & \vdots \\ s_{M-1} & s_M & s_{M+1} & \cdots & s_{2M-1} \end{bmatrix}_{M\times(M+1)} \tag{2.35}$$

$$\mathbf{w} = \begin{bmatrix} 1 & w_1 & w_2 & \cdots & w_M \end{bmatrix}^{\mathbf{T}}_{1\times(M+1)} \tag{2.36}$$

and $^{\mathbf{T}}$ is the transpose of a vector or a matrix (non-Hermitian). A solution to(2.34) is derived through rearrangement; letting $w_0 = 1$ allows the first column of $\mathbf{S}$ to be moved to the right hand side:

$$\overbrace{\begin{bmatrix} s_1 & s_2 & \cdots & s_M \\ s_2 & s_3 & \cdots & s_{M+1} \\ \vdots & \vdots & \ddots & \vdots \\ s_M & s_{M+1} & \cdots & s_{2M-1} \end{bmatrix}_{M\times M}}^{\dot{\mathbf{S}}} \overbrace{\begin{bmatrix} w_1 \\ w_2 \\ \vdots \\ w_M \end{bmatrix}_{M\times 1}}^{\dot{\mathbf{w}}} = \overbrace{\begin{bmatrix} -s_0 \\ -s_1 \\ \vdots \\ -s_{M-1} \end{bmatrix}_{M\times 1}}^{\dot{\mathbf{b}}} \tag{2.37}$$

Assuming that $\dot{\mathbf{S}}$ is an invertible square matrix, $\dot{\mathbf{w}}$ becomes:

$$\dot{\mathbf{w}} = \dot{\mathbf{S}}^{-1}\dot{\mathbf{b}}$$

It is important to note that this formulation requires two elements per arrival thus $N = 2M$, and is fully determined or fully constrained. The case of an overdetermined or over-constrained solution is discussed in the next section.

2.2.2 Over-constrained Null Steering

In the over-constrained case, $N > 2M$, the solution must be approached as a minimization of the null steering problem as an exact solution likely does not exist:

$$\min_{\mathbf{w}} \|\mathbf{S}\mathbf{w}\| \tag{2.38}$$

where $\|\cdot\|$ is the Euclidean norm or L^2 norm, min is a minimization, and

$$\mathbf{S} = \begin{bmatrix} s_0 & s_1 & s_2 & \cdots & s_M \\ s_1 & s_2 & s_3 & \cdots & s_{M+1} \\ \vdots & \vdots & \vdots & \ddots & \vdots \\ s_{N-M-1} & s_{N-M} & s_{N-M+1} & \cdots & s_{N-1} \end{bmatrix}_{(N-M)\times(M+1)} \tag{2.39}$$

$$\mathbf{w} = \begin{bmatrix} w_0 & w_1 & w_2 & \cdots & w_M \end{bmatrix}^{\mathbf{T}}_{1\times(M+1)} \tag{2.40}$$

Since $\mathbf{S}$ is no longer a square matrix it cannot therefore be inverted directly.

Ordinary Least Squares Solution

The *ordinary least squares* (OLS) solution is the first approach chosen to solve the problem. To begin apply the constraint $w_0 = 1$ once more and transform the homogenous minimization (2.38) into:

$$\min_{\ddot{\mathbf{w}}} \left\| \overbrace{\begin{bmatrix} s_1 & s_2 & \cdots & s_M \\ s_2 & s_3 & \cdots & s_{M+1} \\ \vdots & \vdots & \ddots & \vdots \\ s_{N-M} & s_{N-M+1} & \cdots & s_{N-1} \end{bmatrix}}^{\ddot{\mathbf{S}}} \overbrace{\begin{bmatrix} w_1 \\ w_2 \\ \vdots \\ w_M \end{bmatrix}}^{\ddot{\mathbf{w}}} - \overbrace{\begin{bmatrix} -s_0 \\ -s_1 \\ \vdots \\ -s_{N-M-1} \end{bmatrix}}^{\ddot{\mathbf{b}}} \right\| \tag{2.41}$$

The OLS solution to this minimization is to re-write (2.41) as $\ddot{\mathbf{S}}^{\mathbf{H}}\ddot{\mathbf{S}}\ddot{\mathbf{w}} = \ddot{\mathbf{S}}^{\mathbf{H}}\ddot{\mathbf{b}}$, compute the inverse of the normal matrix $\ddot{\mathbf{S}}^{\mathbf{H}}\ddot{\mathbf{S}}$ and apply it both sides [25]:

$$\ddot{\mathbf{w}} = \left(\ddot{\mathbf{S}}^{\mathbf{H}}\ddot{\mathbf{S}}\right)^{-1} \ddot{\mathbf{S}}^{\mathbf{H}}\ddot{\mathbf{b}} \tag{2.42}$$

Recalling that $w_0 = 1$, the solution can be combined to form the polynomial $W(z)$ with coefficients $\begin{bmatrix} 1 & \ddot{w}_1 & \ddot{w}_2 & \cdots & \ddot{w}_M \end{bmatrix}$. This is the null steering polynomial which minimizes the response of the sub-arrays in the OLS sense, and its roots can be used to solve for the angles of arrival. An unfortunate downside to the OLS method its implicit assumption that $\ddot{\mathbf{b}}$ is known exactly and free of measurement errors, and only the sample matrix $\ddot{\mathbf{S}}$ is subject to errors.

In the previous solution the homogenous system (2.34) and (2.38) was transformed into a non-homogenous system using the constraint $w_0 = 1$ in order to apply either an implicit or OLS solution method. In the next section a method is presented which works directly on the homogenous system and distributes measurement errors across all elements.

Total Least Squares Solution

The *total least squares* (TLS) solution is an extension to the OLS method, and in the homogenous case distributes errors throughout $\mathbf{S}$. In the TLS method, *singular value decomposition* (SVD) is used as a means of solving $\min \|\mathbf{Sw}\|$ (2.38). The SVD factorizes the matrix $\mathbf{S}$ into an orthogonal matrix $\mathbf{U}$ of left-singular vectors, a diagonal matrix $\mathbf{\Sigma}$ of positive singular values, and an orthogonal matrix $\mathbf{V}$ of right-singular vectors such that:

$$\mathbf{S} = \mathbf{U}\mathbf{\Sigma}\mathbf{V}^{\mathbf{H}} \tag{2.43}$$

A solution to (2.38) is then found from the right-singular vector corresponding to the smallest non-zero singular value, typically the last column of $\mathbf{V}$

$$\begin{aligned} \mathbf{w} &= \arg\min_{\mathbf{w}} \|\mathbf{Sw}\| && (2.44) \\ &= \mathbf{V} \begin{bmatrix} 0 & \cdots & 0 & 1 \end{bmatrix}^{\mathbf{T}} && (2.45) \end{aligned}$$

with $\|\mathbf{w}\| = 1$.

2.2.3 Root Solving

Thus far several methods of forming the polynomial $W(z)$ have been presented. It has also been shown in (2.31) and (2.29) that the roots of this polynomial, or more specifically the phase of the roots, corresponds to the angle of arrival of plane waves impinging on an N element linear array.

The polynomials associated with the angle-of-arrival problems in this thesis are limited to orders of less than or equal to 4. Furthermore, quadratics, cubics, and quartics are all low order polynomials who's roots have a closed form solution. These closed form solutions, such as the classic $-b \pm \sqrt{b^2 - 4ac}$ for a quadratic, significantly simplify processing and avoid issues related to iterative numerical methods such as convergence, stability, and non-deterministic run-times.

Delving any deeper into root solving is outside of the scope of this thesis, however closed form solutions for quadratics, cubics, and quartics are readily available.

2.2.4 Summary

The chapter began with the introduction of interferometry, and extended interferometry to solve for multiple concurrent angles of arrival in the fully determined case, $N = 2M$. Subsequently, OLS and TLS solutions to the overdetermined case, $N > 2M$, were shown and their merits discussed. Finally, the roots of the $W(z)$ polynomial and angles-of-arrival were shown to be related.

The following is a summary of the steps used throughout this thesis to solve for M angles of arrival present on an N element array, $N \geq 2M$:

1. Construct the sub-array sample matrix $\mathbf{S}$:

$$\mathbf{S} = \begin{bmatrix} s_0 & s_1 & s_2 & \cdots & s_M \\ s_1 & s_2 & s_3 & \cdots & s_{M+1} \\ \vdots & \vdots & \vdots & \ddots & \vdots \\ s_{N-M-1} & s_{N-M} & s_{N-M+1} & \cdots & s_{N-1} \end{bmatrix}_{(N-M)\times(M+1)}$$

2. Decompose the sample matrix $\mathbf{S}$ through SVD :

$$[\mathbf{U}, \mathbf{\Sigma}, \mathbf{V}] = \mathrm{svd}\left(\mathbf{S}\right)$$

3. Take the last column of $\mathbf{V}$ as the solution to $\min_{\mathbf{w}} \|\mathbf{S}\mathbf{w}\|$:

$$\mathbf{w} = \mathbf{V} \left[\begin{array}{cccc} 0 & \cdots & 0 & 1 \end{array}\right]^{\mathbf{T}}$$

4. Compute the complex roots of the polynomial in z with complex coefficients $\mathbf{w}$:

$$\mathbf{r} = \mathrm{roots}\left(\mathbf{w}\right)$$

5. Determine the phase of each root and the resulting angle-of-arrival :

$$\theta_m = \sin^{-1}\left(\frac{\arg\left(r_m\right)}{k\,d}\right)$$

Chapter 3

Investigation of the Effect of Noise on Angle Estimates Through Simulation

The previous section discussed the mathematics of interferometry and angle-of-arrival. The objective of this section is to look at the effect of noise on the angle estimates derived using $\lambda/2$ interferometry, vernier interferometry, and angle of arrival. While beyond the scope of this thesis, analytical investigations of interferometric and angle-of-arrival estimates in the presence of noise is an active area of study in the literature [26]. In this thesis the approach taken is to simulate several sepecific example scenarios that can also then be directly investigated experimentally.

In each scenario, the presence of *additive white Gaussian noise* (AWGN) corrupts the interferometric phase difference or angle-of-arrival estimate in a nonlinear way that varies with the *signal to noise ratio* (SNR). Presented below therefore is a series of MATLAB simulations conducted to compute the variance of the angle estimate as a function of SNR using three different but representative angle measurement strategies.

3.1 Angle Variance for $\lambda/2$ Interferometry.

In this simulation, $s_0(i)$ and $s_1(i)$ are the responses of two $\lambda/2$ spaced elements receiving a continuous plane wave arrival from the angle θ. Complex independent white Guassian noise is added to each element and an angle estimate $\hat{\theta}$ is computed in the presence of the added noise

$$
\begin{aligned}
s_0(i) &= A + n_0(i) && (3.1)\\
s_1(i) &= A\exp(\jmath\pi\sin\theta) + n_1(i) && (3.2)\\
\hat{\theta}_i &= \sin^{-1}\left(\frac{1}{\pi}\arg\left(s_0(i)\,s_1^*(i)\right)\right) && (3.3)
\end{aligned}
$$

where $n(i)$ is white Guassian noise, and A is set to generate a desired signal to noise ratio.

The simulation was performed at 4 different angles, 0°, 30°, 45° and 60° with SNR ranging from 10 dB to 60 dB. The conversion from electrical phase to arrival angle is a nonlinear operation (inverse sine), and it follows that the variance in the angle of arrival estimate depends on the angle of arrival itself.

In the simulation, the SNR is calculated at the input to the phase detector and is the same for both input signals, and the two noise sources are independent AWGN. The importance of SNR is observed in Figure 3.1 where the results of multiple simulation runs show the variance of the angle estimate for different angles of arrival. For example: At an SNR of 26 dB and arrival angle of 30°, the standard deviation in the angle estimate is $\approx 1°$; while for a +11 dB increase in SNR the standard deviation decreases to $\approx 0.3°$. It is therefore concluded that methods for increasing the SNR, such as code-pulse compression as presented in Chapter 4, will be beneficial in reducing the variance of angle-of-arrival estimates. Furthermore, for the case of a single arrival, the simulation results shown in Figure 3.1 provide a quantitative prediction of the variance reduction for a specified SNR improvement.

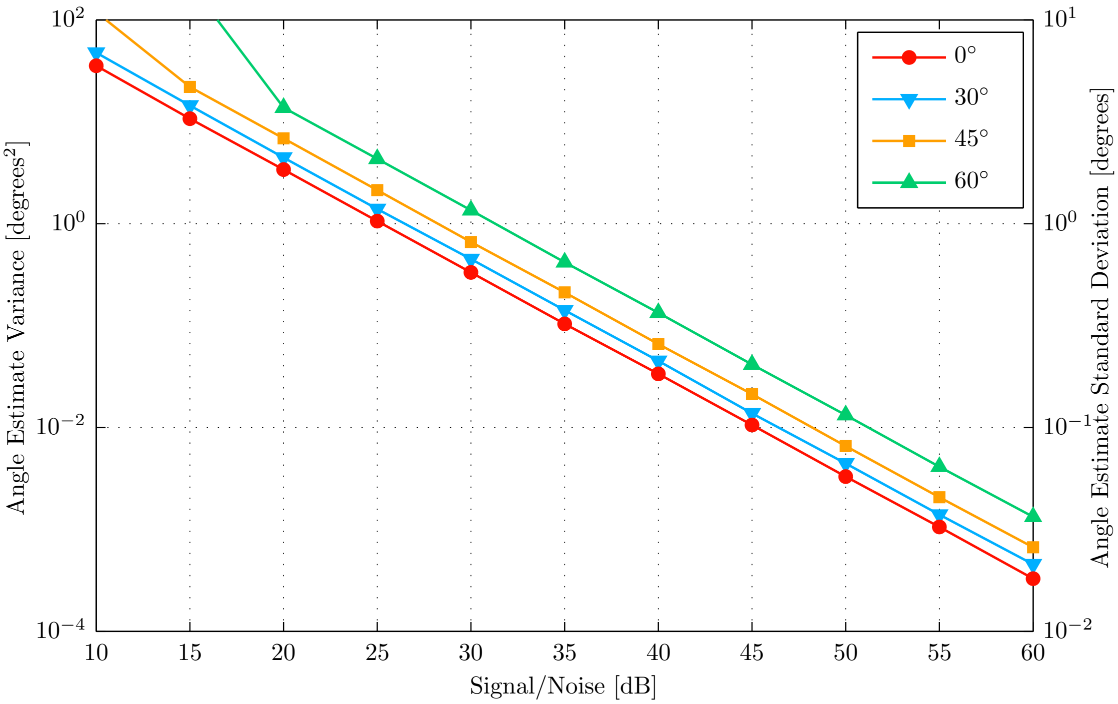

Figure 3.1: Variance in $\lambda/2$ interferometric angle estimate as a function of SNR for 0°, 30°, 45° and 60° arrivals.

3.2 Angle Variance for $7\lambda/2$ Vernier Interferometry.

For vernier interferometry the required SNR for a specified variance is reduced due to the increased element spacings. In the associated simulation, three elements are used to form two interferometric differential phase measurements. One measurement is derived from a $\lambda/2$ spaced pair of elements, while the other measurement is derived from a $7\lambda/2$ element pair. The increased spacing of the $7\lambda/2$ element pair results in electrical phase noise having less of an effect on the computed angle,[1] however the angle solution is also ambiguous. This ambiguity is resolved using the $\lambda/2$ element pair.

The method works well at and above 25 dB as can be observed in Figure 3.2. At

---

[1] Electrical noise has less effect due to the amplified phase differences for similar changes in angle-of-arrival and noise level.

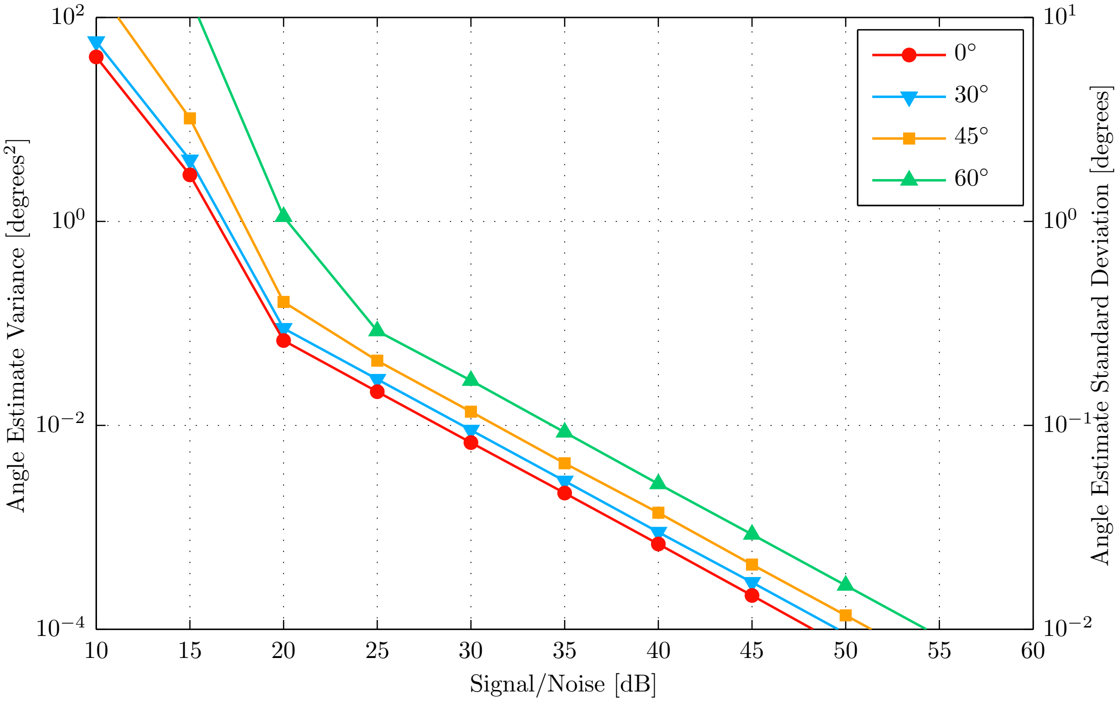

Figure 3.2: Variance in vernier interferometric angle estimate as a function of SNR for 0°, 30°, 45° and 60° arrivals.

an SNR of 26 dB the standard deviation in the angle estimate is $\approx 0.13°$, significantly lower than the $\lambda/2$ interferometry result. However, below 20 dB the phase variance in the $\lambda/2$ element pair is large enough to occasionally cause incorrect ambiguity resolution, and vernier interferometry breaks down with large angle estimation errors.

3.3 Angle Variance for 8-Element TLS AOA With One Arrival.

The 8-element, $\lambda/2$ spaced, TLS AOA method was also evaluated for variance in the presence of one arrival and AWGN. The results are surprisingly very similar to the vernier interferometry example results of the previous section. However, the method no longer breaks down at lower SNRs and has the added benefit of also providing solutions for multiple arrivals, such as those caused by multipaths.

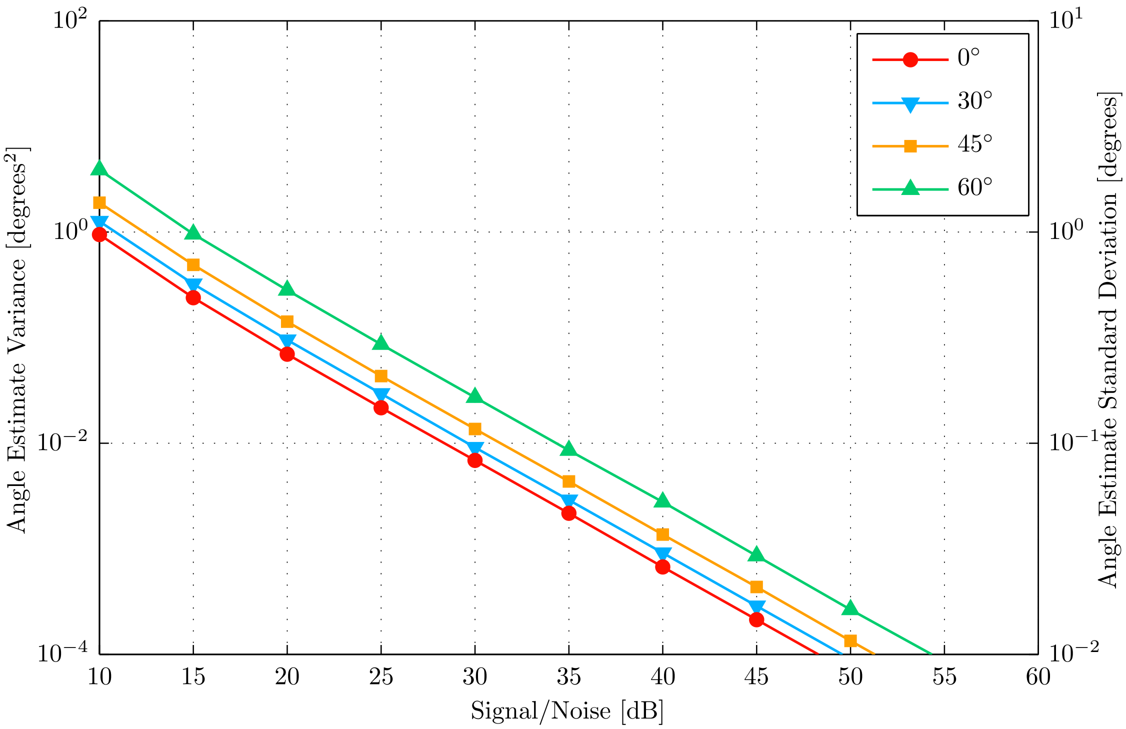

Figure 3.3: Variance in TLS AOA angle estimate as a function of SNR for 0°, 30°, 45° and 60° arrivals.

With an SNR of 26 dB, the TLS AOA method applied over 8-elements has a variance of $\approx 0.13°$, the same as the $7\lambda/2$ vernier interferometry. This similarity can be further observed in Figure 3.3, where four different traces show the change in variance with SNR at different angles of arrival.

3.4 Summary

The variance in the angle estimates for both interferometry and angle-of-arrival processing depends on SNR, together with the incident angle of the plane wave. At angles away from broadside, the angle variance of the solutions is higher due to the non-linear $\sin^{-1}$ transformation when converting from electrical phase ϕ to physical angle of arrival θ.

Chapter 4

Pulse Coding for Increased Signal-to-Noise Ratio

Pulse compression is a method used to increase *the signal to noise ratio* (SNR) of backscatter without sacrificing resolution. An adequate SNR is essential for swath bathymetry, in order to compute a good angle estimate, and an increase in SNR reduces the variance of the received signal. The pulse compressor filter was first described in a wartime patent [27] filed in September 1945, and was initially applied to radar. The pulse compressor is essentially a filter matched to a carefully chosen transmitted waveform, rightfully named a matched filter. On reception, this matched filter is used to time compress the signal and maximize the SNR of the backscatter return. The first example of pulse compressed radar used a *linear frequency modulated* (LFM) pulse, commonly referred to as a chirp. The concept of pulse compression has been developed over time, beginning in the 1950s [28, 29] to cover topics such as processing gain, sidelobe levels, binary coded sequences, poly-phase sequences, and sidelobe suppression methods.

This chapter quantifies the SNR benefits of pulse compression as applied to swath bathymetry and explores implementation details. First, pulse compression is introduced. Second, methods for evaluating the performance of pulse compression are introduced. Finally, specific pulse compression codes are defined, discussed, and evaluated.

4.1 Pulse Compression

In traditional sidescans, the transmitted waveform is a sinusoid pulse of a given duration τ_p and amplitude at the sonar frequency. The received backscatter is either filtered to a specific bandwidth to limit noise, or match filtered with the transmitted waveform to maximize SNR. The latter can be done because the received backscatter consists of time-delayed scaled copies of a known signal, the transmitted waveform. The amount of backscatter energy received is therefore proportional to the energy of the transmitted waveform. The backscatter SNR can therefore be increased by increasing the energy in the transmitted waveform. This can be achieved by illuminating the scatters with a longer duration or a higher amplitude pulse. Unfortunately, increasing the duration of the pulse has the undesired effect of reducing the range resolution Δr, which for a sinusoidal pulse can be expressed as

$$\Delta r = c\,\tau_p/2 \tag{4.1}$$

where c is the speed of sound in water.

On the other hand, increasing the amplitude of the pulse has practical limitations: the transducer's piezoceramic maximum allowable electric field amplitude [30], the transducer's cavitation threshold [31], and the transmitter's electrical component voltage limitations. These amplitude limitations directly motivated the development of pulse compression in radar systems, where the magnetron and other transmitter components were sparking at extremely high voltages [27].

The range resolution of a sonar system, given in (4.1), can also be approximated by the bandwidth of the transmitted waveform or through the examination of the *auto-correlation function* (ACF) of the transmitted waveform.

Let the range resolution be redefined in terms of pulse bandwidth, B_p:

$$\Delta r \approx \frac{c}{2B_p} \tag{4.2}$$

From (4.2), if the bandwidth of the transmitted pulse can be maintained while its time duration is increased, the result will be a higher energy pulse that maintains the same range resolution. The pulse compression filter then combines the backscatter signal energy coherently while *additive white Gaussian noise* (AWGN) combines incoherently; the result is a boost in SNR.

Figure 4.1 shows the baseband representation of four different pulses and their received match filtered responses. The first is a simple short pulse. The other 3 pulses increase the power in the water by increasing the pulse amplitude, increasing the pulse duration, and coding the transmitted pulse. In (b), the amplitude is tripled, although this may not be practical due to the prior stated reasons. In (c), the pulse duration is tripled, which negatively impacts the range resolution. In (d), the pulse duration is also tripled, and the pulse is coded to maintain range resolution.

4.2 Coded-Pulse Compression

In coded-pulse compression, the transmitted waveform consists of a code or sequence $\mathbf{c}$ of a set of symbols $\{c_n\}$

$$\mathbf{c} = \{c_0,\, c_1,\, \ldots\, , c_{N-1}\} \tag{4.3}$$

where each symbol is a complex value, representing both phase and magnitude, by which the carrier frequency is modulated for a given fixed duration τ_s. Let $s_{\mathrm{cp}}(t)$

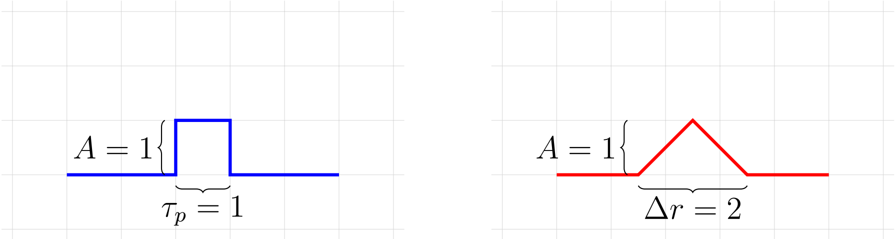

(a) Baseband representation of pulse and its ACF.

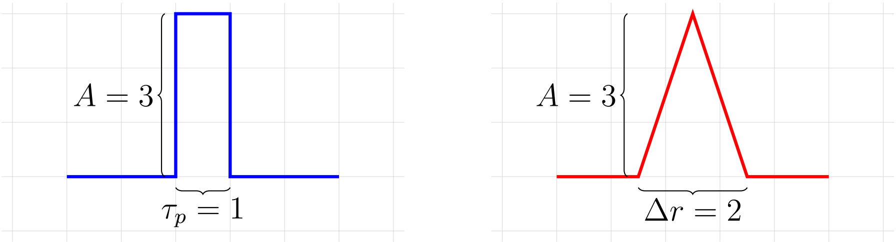

(b) Higher amplitude pulse and its ACF.

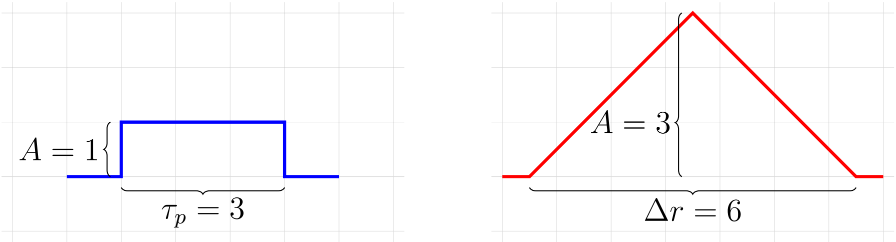

(c) Longer duration pulse and its ACF.

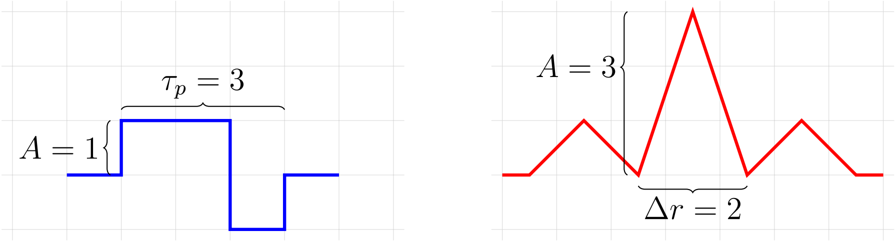

(d) Coded pulse and its ACF.

Figure 4.1: Options for increasing SNR by tailoring the transmitted waveform.

denote the transmitted coded pulse:

$$\begin{aligned} s_{\mathrm{cp}}(t) &= \mathrm{Re}\left\{g_{\mathrm{cp}}(t)\ \mathrm{e}^{j2\pi f_c t}\right\} && (4.4) \\ g_{\mathrm{cp}}(t) &= \sum_n c_n \,\mathrm{rect}\left(\frac{t-n\tau_s}{\tau_s}\right) && (4.5) \\ &= \mathrm{rect}\left(\frac{t}{\tau_s}\right) * \sum_n c_n \delta\left(t-n\tau_s\right) && (4.6) \end{aligned}$$

where $\mathrm{Re}\{\cdot\}$ denotes the real part of $\{\cdot\}$, f_c is the carrier frequency, and rect is defined as:

$$\mathrm{rect}(t) = \begin{cases} 1 & \text{for } |t| < \frac{1}{2} \\ \frac{1}{2} & \text{for } |t| = \frac{1}{2} \\ 0 & \text{otherwise} \end{cases} \tag{4.7}$$

The baseband $g_{\mathrm{cp}}(t)$ is called the complex envelope of $s_{\mathrm{cp}}(t)$. From (4.2), the range resolution of a system utilizing a coded pulse can be approximated by the bandwidth of $g_{\mathrm{cp}}(t)$, which in turn can be approximated by the duration of an individual symbol τ_s .

Let $r_{\mathrm{cp}}(t)$ denote the corresponding backscattered received coded pulse,

$$r_{\mathrm{cp}}(t) = s_{\mathrm{cp}}(t) * \sum_m a_m\, \delta\left(t - \frac{2r_m}{c}\right) \tag{4.8}$$

where $\mathbf{a} = \{a_0, \ldots, a_{M-1}\}$ is a set of complex scatterers at relative ranges $\mathbf{r} = \{r_0, \ldots, r_{M-1}\}$, and where c is the sound speed in water and is assumed to be constant. The matched filter operation in continuous time is then represented as a convolution of the impulse response of the matched filter $h_{\mathrm{mf}}(t)$ with the received signal :

$$\begin{aligned} y\left(t\right) &= h_{\mathrm{mf}}\left(t\right) * r_{\mathrm{cp}}\left(t\right) && (4.9)\\ &= \int_{-\infty}^{\infty} h_{\mathrm{mf}}\left(t-\tau\right)\, r_{\mathrm{cp}}\left(\tau\right) d\tau && (4.10)\end{aligned}$$

where

$$h_{\mathrm{mf}}\left(t\right) = s_{\mathrm{cp}}^{*}\left(-t\right) \tag{4.11}$$

From (4.10) and (4.11), the matched filter operation is

$$y\left(t\right) = \int_{-\infty}^{\infty} s_{\mathrm{cp}}^{*}\left(\tau-t\right)\, r_{\mathrm{cp}}\left(\tau\right) d\tau \tag{4.12}$$

Under the assumption of a single scatterer of magnitude $a_0 = 1$ and at range $r_0 = 0$, (4.12) simplifies to

$$\begin{aligned} y\left(t\right) &= \int_{-\infty}^{\infty} s_{\mathrm{cp}}^{*}\left(\tau-t\right)\, \left(s_{\mathrm{cp}}\left(\tau\right) * \delta\left(\tau\right)\right) d\tau && (4.13)\\ &= \int_{-\infty}^{\infty} s_{\mathrm{cp}}^{*}\left(\tau-t\right)\, s_{\mathrm{cp}}\left(\tau\right) d\tau && (4.14)\\ R_{ss}\left(t\right) &= \int_{-\infty}^{\infty} s_{\mathrm{cp}}^{*}\left(\tau-t\right)\, s_{\mathrm{cp}}\left(\tau\right) d\tau && (4.15)\end{aligned}$$

and is further simplified in (4.14) using the delta-Dirac sifting property. The above equation is recognized as the auto-correlation of s_{cp}, labelled $R_{ss}\left(t\right)$, and can also be expressed as

$$R_{ss}\left(t\right) = \mathrm{Re}\left\{\mathrm{e}^{j2\pi f_c t}\, R_{cc}\left(t\right)\right\} \tag{4.16}$$

where $R_{cc}\left(t\right)$ is the auto-correlation of the baseband coded pulse:

$$R_{cc}\left(t\right) = \int_{-\infty}^{\infty} g_{\mathrm{cp}}^{*}\left(\tau-t\right)\, g_{\mathrm{cp}}\left(\tau\right) d\tau \tag{4.17}$$

A sampling of (4.17) at $t = k\tau_s$ gives the discrete auto-correlation of the code sequence.

Much of the research has been focused on finding symbol sequences with favourable auto-correlation properties. The symbols of these sequences are almost always restricted to have a constant magnitude, mainly due to the electronic design of typical transmitters.[1]

Codes can be divided into binary-phase codes and poly-phase codes. In a binary-phase sequence the phase of each symbol is restricted to either 0° or 180°. In a poly-phase sequence the phase of each symbol is unrestricted, 0° - 360°. A common set of binary-phase codes with favorable ACF properties are the Barker sequences [32]. The Barker sequence of length 13 (4.18) will be used as the reference code to demonstrate the different concepts that are innate to phase-coded pulse compression and used to evaluate its performance; other codes and the process of code selection will be discussed at the end of the chapter.

$$\mathbf{c} = \left\{ \begin{array}{ccccccccccccc} +1 & +1 & +1 & +1 & +1 & -1 & -1 & +1 & +1 & -1 & +1 & -1 & +1 \end{array} \right\} \tag{4.18}$$

4.2.1 Aperiodic Auto-correlation Function

The aperiodic auto-correlation function (ACF) of a code $\mathbf{c}$ is defined as

$$R_{\mathbf{cc}}\left[k\right] = \sum_{n} c_n^* c_{n+k} \tag{4.19}$$

where k is the lag. As shown in (4.9-4.14), the structure of the ACF is similar to that of a matched filter, and identical when the return contains only one equal amplitude scatterer. Therefore the ACF provides direct insight into the performance of a specific code. An ideal ACF has an output equal to the total energy in the

---

[1] The transmit circuit typically uses a non-linear class-D amplifier that features an H-bridge arrangement of MOSFETs and therefore is only able to generate one fixed amplitude.

entire pulse compressed to a single output sample and no output elsewhere. Thus an ideal ACF resembles a Dirac delta function. Figure 4.2 illustrates the ACF of the Barker-13 sequence as compared to a single symbol pulse.

4.2.2 Processing Gain

The peak response of the ACF is at $R_{\mathbf{cc}}\left[0\right]$, and is called the *mainlobe*.[2] For the Barker-13, it is 13 times larger than that of the single symbol. From this observed increase in response, a processing gain $\mathrm{PG}_{\mathrm{lin}}$ is defined and represents the gain in SNR achieved through pulse compression:

$$\mathrm{PG}_{\mathrm{lin}} = \left(\frac{R_{\mathbf{cc}}\left[0\right]}{\sqrt{R_{\mathbf{cc}}\left[0\right]}}\right)^2 = R_{\mathbf{cc}}\left[0\right] \tag{4.20}$$

In (4.20), the signal power adds coherently and the noise power adds incoherently, which is expressed by $R_{\mathbf{cc}}\left[0\right]/\sqrt{R_{\mathbf{cc}}\left[0\right]}$. For codes with unity magnitude symbols, such as the Barker-13, the processing gain can be further simplified to

$$\mathrm{PG}_{\mathrm{lin}} = N \tag{4.21}$$

and expressed in terms of decibels as

$$\mathrm{PG}_{\mathrm{dB}} = 10\log_{10} N \tag{4.22}$$

where N is the code length. For the Barker-13, the processing gain is therefore 11.1 dB.

---

[2] References to mainlobe in this chapter refer to the main response of the ACF, where as a second meaning of mainlobe is used in Chapter 5 referring to transducer beampattern response.

(a) Single Symbol

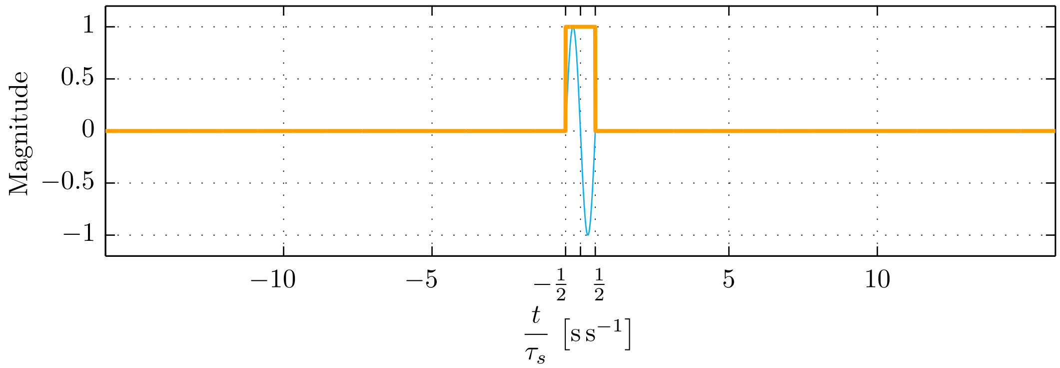

(c) ACF of Single Symbol

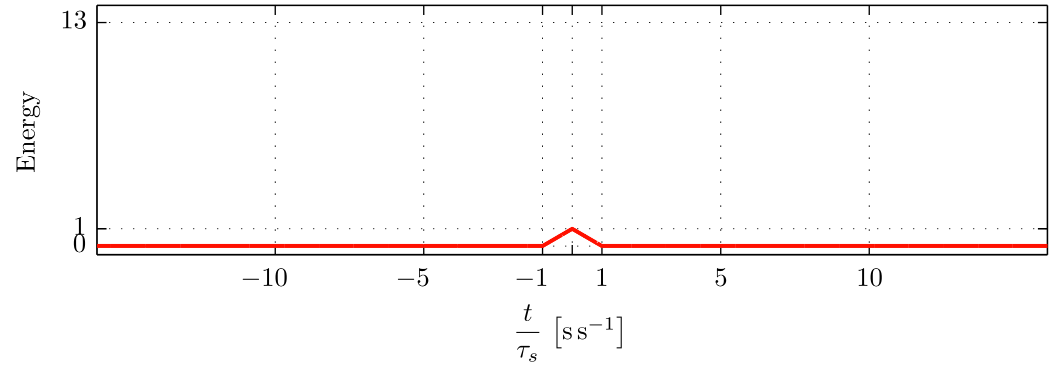

(b) Barker-13

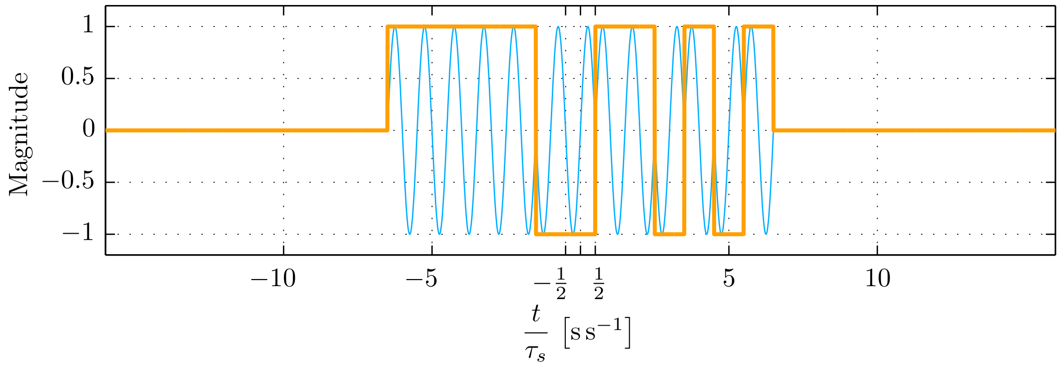

(d) ACF of Barker-13

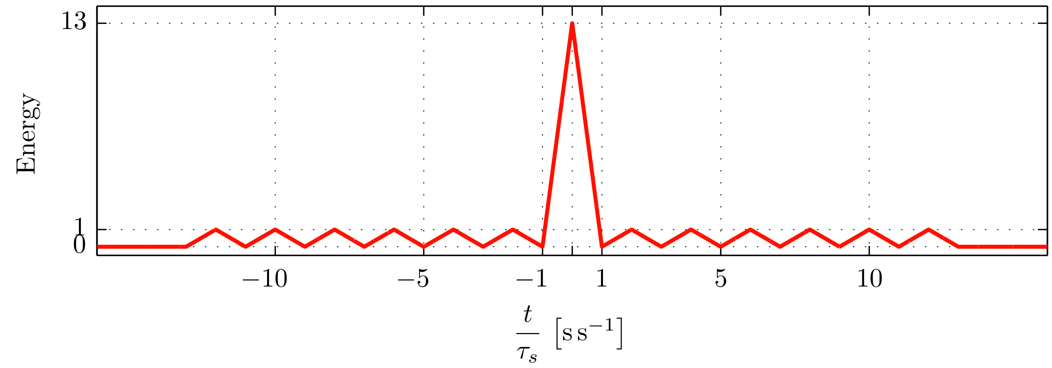

Figure 4.2: Single symbol and Barker-13 codes and relevant ACFs.

4.2.3 Peak and Integrated Sidelobe Levels

A problem inherent to pulse compression, visible in Figure 4.2, is that the ACF does not yield a perfect impulse response, $R_{\mathbf{cc}}[k] \neq 0$ for all $k \neq 0$. These non-zero ACF values are referred to as sidelobes and contribute to a degradation in performance, often referred to a self noise. The reduction of these sidelobes is addressed later in this chapter.

Suppose the received signal consists of two discrete copies of the code equal in intensity and separated in time by k:

$$x_i = c_i + c_{i+k} \tag{4.23}$$

The matched filter output then becomes

$$\begin{aligned} y_i &= \sum_n \bar{c}_{i+n}\, x_{i+n} && (4.24)\\ &= \sum_n \bar{c}_{i+n}\, c_{i+n} + \sum_n \bar{c}_{i+n}\, c_{i+k+n} && (4.25)\\ &= R_{\mathbf{cc}}[i] + R_{\mathbf{cc}}[i+k] && (4.26) \end{aligned}$$

and at the specific sample, for example $i = 0$, the output y becomes:

$$y_0 = R_{\mathbf{cc}}[0] + R_{\mathbf{cc}}[k] \tag{4.27}$$

Thus the leakage of the k^{th} sidelobe return into the mainlobe return is dependent on the ACF of the code at the k^{th} lag. The ratio of the two ACF values is a measure of the leakage and gives rise to the two most frequently used sidelobe measures: the peak sidelobe level (PSL) ratio and the integrated energy sidelobe level (ISL) ratio. The PSL represents the ratio of the energy in the largest sidelobe to the energy in the mainlobe, and from the auto-correlation function is defined as

$$\mathrm{PSL}_{\mathrm{lin}} = \max_{k \neq 0} \left(\frac{R_{\mathbf{cc}}[k]\, R^*_{\mathbf{cc}}[k]}{R_{\mathbf{cc}}[0]\, R^*_{\mathbf{cc}}[0]} \right) \tag{4.28}$$

where $R^*_{\mathbf{cc}}$ denotes a complex conjugate of the ACF. The ISL represents the ratio of the total energy contained in all the sidelobes, the total leakage energy, relative to the energy in the mainlobe and is defined as:

$$\mathrm{ISL}_{\mathrm{lin}} = \sum_{k \neq 0} \left(\frac{R_{\mathbf{cc}}[k]\, R^*_{\mathbf{cc}}[k]}{R_{\mathbf{cc}}[0]\, R^*_{\mathbf{cc}}[0]} \right) \tag{4.29}$$

Both measures are often calculated in decibels:

$$\mathrm{PSL}_{\mathrm{dB}} = 10 \log_{10} \mathrm{PSL}_{\mathrm{lin}} \tag{4.30}$$

$$\mathrm{ISL}_{\mathrm{dB}} = 10 \log_{10} \mathrm{ISL}_{\mathrm{lin}} \tag{4.31}$$

The Barker-13's PSL and ISL are $-22.3\,\mathrm{dB}$ and $-11.5\,\mathrm{dB}$ respectively. Two simulations were conducted to illustrate the effect of pulse compression sidelobes on sonar systems.

In the first simulation, three discrete scatterers give rise to a number of false returns that are shown in Figure 4.3. In the figure, the sidelobes resulting from the use of the Barker-13 sequence are seen early in the return, and at the same time a larger response is seen later due to the coherent combination of the sidelobes from two of the scatterers. The last scatter has a weaker intensity and is obscured by the sidelobes of the other two strong scatterers. This result shows the need for low PSL when attempting to reject false returns from a sparse set of scatters.

The second simulation consists of a set of tightly grouped scatterers. This more closely approximates the situation in sidescan where the pulse footprint travels along the seafloor and produces a continuous return. The result of this simulation, seen in

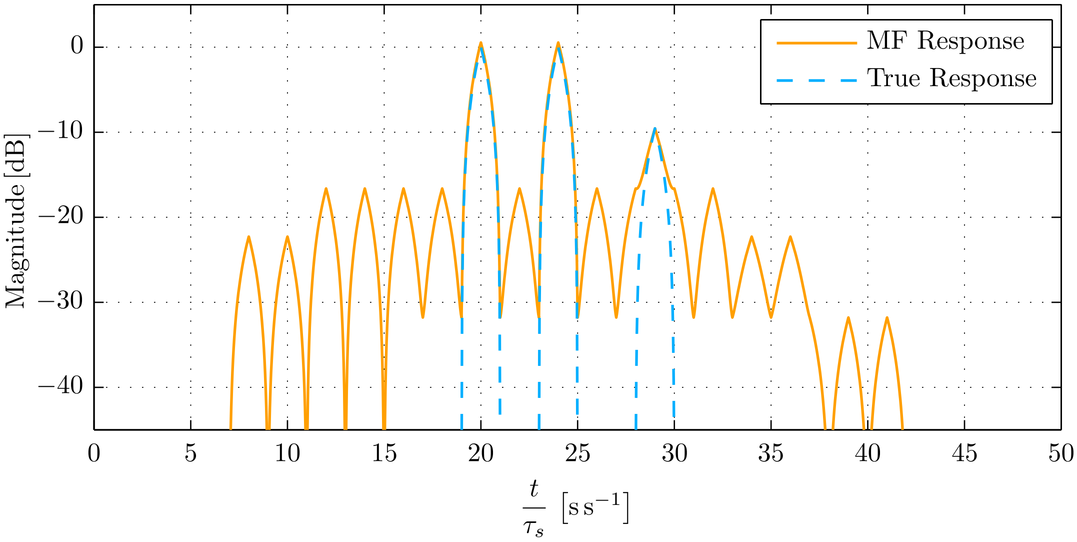

Figure 4.3: Simulation results for a Barker-13 coded pulse illuminating three discrete scatters.

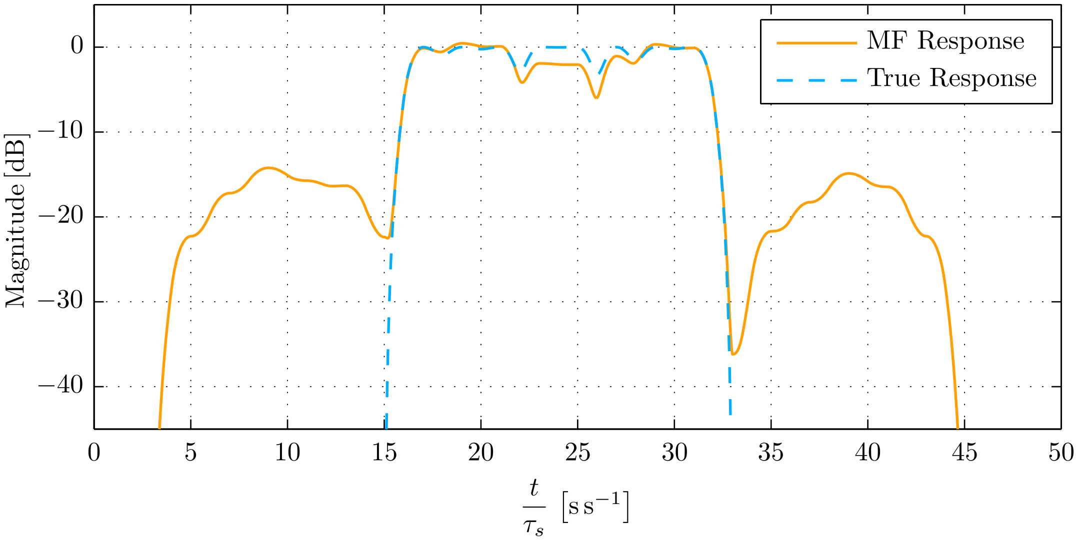

Figure 4.4: Simulation results for a Barker-13 coded pulse illuminating a continuum of scatters.

Figure 4.4, exhibits large phantom $-15\,\mathrm{dB}$ returns on both sides of the continuous footprint caused by sidelobes. Within the continuous return, the leakage caused by adjacent sidelobes distorts the matched filter response from the true response. The degree of this distortion is quantified by the ISL measure and should be minimized.

A popular method used to reduce sidelobes is to mismatch the pulse compression filter.

4.3 Mismatched Pulse Compression Filter

Unlike a matched filter, a mismatched filter is designed to meet a condition other than maximizing the SNR and in doing so sacrifices SNR. The two most popular optimizations are to minimize the ISL or PSL response of the filter. Another advantage of the mismatched filter is that the length of the filter can be greater than the code length. This enables the system to push the sidelobes down further at the expense of creating more sidelobes of lower magnitude over a longer time window. Both optimizations generate a filter that is less then optimal in terms of maximizing the SNR and this sacrifice is referred to as a *loss in processing gain* (LPG) and can be calculated from

$$\mathrm{LPG}_{\mathrm{lin}} = \frac{R_{\mathbf{ch}}[0]\, R^{*}_{\mathbf{ch}}[0]}{R_{\mathbf{cc}}[0]\, R^{*}_{\mathbf{cc}}[0]} \tag{4.32}$$

where $R_{\mathbf{ch}}[0]$ is the response or cross-correlation of the code with the generated filter at the mainlobe. The LPG is often computed in decibels as:

$$\mathrm{LPG}_{\mathrm{dB}} = 10\log_{10}\mathrm{LPG}_{\mathrm{lin}} \tag{4.33}$$

4.3.1 Minimizing Integrated Sidelobe Level

The generation of a filter that minimizes the ISL is a linear least mean squares problem. The condition to be minimized can be expressed as:

$$f(\mathbf{h}) = \sum_{k \neq 0} \frac{R_{\mathbf{ch}}[k]\, R^{*}_{\mathbf{ch}}[k]}{R_{\mathbf{ch}}[0]\, R^{*}_{\mathbf{ch}}[0]} \tag{4.34}$$

More conveniently, in [33] the problem is stated in matrix form and a closed form solution for the minimum ISL mismatched filter is found as

$$\mathbf{h} = \mathbf{B}^{-1}\mathbf{c} \tag{4.35}$$

where $\mathbf{c}$ is a vector of length N containing the transmitted binary or poly-phase code symbols, $\mathbf{h}$ is the computed filter of length $P \geq N$, and

$$\mathbf{B} = \mathbf{C}\,\mathbf{F}\,\mathbf{C}^{\mathbf{H}} \tag{4.36}$$

where $\mathbf{C}$ is the full convolution matrix

$$\mathbf{C} = \begin{bmatrix} 0 & \cdots & \cdots & 0 & c_0 & c_1 & \cdots & c_{N-1} \\ 0 & \cdots & 0 & c_0 & c_1 & \cdots & c_{N-1} & 0 \\ \vdots & & & & & & & \vdots \\ 0 & c_0 & c_1 & \cdots & c_{N-1} & 0 & \cdots & 0 \\ c_0 & c_1 & \cdots & c_{N-1} & 0 & \cdots & \cdots & 0 \end{bmatrix}_{P \times P} \tag{4.37}$$

and $\mathbf{F}$ is the $P \times P$ identity matrix with the centre element set to 0. A MATLAB implementation of this closed form solution is displayed in Figure 4.5.

```
function [ h ] = generate_MISL_filter( c , P )
    % Parameters:
    % c : complex code symbol sequence
    % P : length of the mismatched filter in symbols

    % Number of symbols in code:
    N = length(c);
    if (P < N)
        error('P cannot be smaller than code length');
    end

    % Zeropad the code to the mismatched filter length:
    c = [zeros(1,(P-N)/2) c zeros(1,(P-N)/2)];

    % Form the C convolution matrix:
    C = hankel([zeros(1,P) c]);
    C = C(1:P,2:end);

    % Create the I matrix with center element zero:
    F = eye(2*P-1);
    F(P,P) = 0;

    % Compute the B:
    B = C*F*C';

    % Compute the filter:
    h = inv(B)*c.';
end
```

Figure 4.5: MATLAB implementation of a linear least mean squares solution for a minimum ISL filter.

4.3.2 Minimizing Peak Sidelobe Level

The generation of a minimum PSL filter is often accomplished through linear programming techniques [34, 35]. The condition to be minimized can be expressed as

$$f(\mathbf{h}) = \max_{k \neq 0} \left(\frac{R_{\mathbf{ch}}[k]\, R^{*}_{\mathbf{ch}}[k]}{R_{\mathbf{ch}}[0]\, R^{*}_{\mathbf{ch}}[0]} \right) \tag{4.38}$$

where $\mathbf{h}$ are the filter coefficients to be manipulated in-order to minimize $f(\mathbf{h})$. In this thesis, the MATLAB function `fmincon`() is used to minimize the PSL with the filter coefficients initialized to the minimum ISL filter. This initialization is done to speed up the convergence of `fmincon`() and it does so because the minimum PSL coefficients are typically close in value to the minimum ISL ones. The MATLAB code to do this is available in Figure 4.6.

4.3.3 Normalizing Filter Power

In order to allow for direct performance comparisons, the generated filter is normalized such that it is equivalent in noise power to the matched filter. This is done by applying the following constraint:

$$\frac{\sum_i h_{\text{mf}}[i]\, h^*_{\text{mf}}[i]}{\sum_i h_{\text{mmf}}[i]\, h^*_{\text{mmf}}[i]} = 1 \tag{4.39}$$

$$\mathbf{h}_{\text{mf}}\mathbf{h}^*_{\text{mf}} = \mathbf{h}_{\text{mmf}}\mathbf{h}^*_{\text{mmf}} \tag{4.40}$$

Scaling the vector $\mathbf{h}_{\text{mmf}}$ by the scalar value $\sqrt{\frac{\mathbf{h}_{\text{mf}}\mathbf{h}^*_{\text{mf}}}{\mathbf{h}_{\text{mmf}}\mathbf{h}^*_{\text{mmf}}}}$ applies the constraint

$$\mathbf{h}^{normalized}_{\text{mmf}} = \mathbf{h}_{\text{mmf}}\sqrt{\frac{\mathbf{h}_{\text{mf}}\mathbf{h}^*_{\text{mf}}}{\mathbf{h}_{\text{mmf}}\mathbf{h}^*_{\text{mmf}}}} \tag{4.41}$$

where $\mathbf{h}_{\text{mf}}$ are the matched filter coefficients and $\mathbf{h}_{\text{mmf}}$ are the mismatched filter coefficients.

4.3.4 Example of Min PSL and Min ISL filters for Barker-13

A classical example of mismatched filters compared to the match filter is shown in Figure 4.7. In this figure, the matched filter response is shown side by side with the response generated by the minimum ISL filter of length 13, and the response generated by the minimum PSL filter of length 13. Closer inspection of this figure shows that the minimum PSL filter has the lowest peak sidelobe $-25.6\,\text{dB}$, and the minimum ISL filter has the lowest integrated sidelobe level $-15.7\,\text{dB}$, also the LPG is very small for both filters $-0.2\,\text{dB}$. These results show the benefits of using mismatched

```matlab
function [ h ] = generate_MPSL_filter( c , P )
    % Parameters:
    % c : complex code symbol sequence
    % P : length of the mismatched filter in symbols

    % Number of symbols in code:
    N = length(c);
    if (P < N)
        error('P cannot be smaller than code length');
    end

    % Zeropad the code to the mismatched filter length:
    c = [zeros(1,(P-N)/2) c zeros(1,(P-N)/2)];

    % Generate the initial starting filter using MISL:
    hi = generate_MISL_filter(c, P).';

    % Setup the options for the fmincon LP method:
    opt = optimset('Algorithm', 'interior-point', ...
                   'TolX', 1e-9, ...
                   'TolFun', 1e-9, ...
                   'MaxFunEvals', 500000, ...
                   'MaxIter', 3000);

    % Execute LP minimization on the objective
    % function psl() defined below:
    [h, ~, ~] = fmincon(@(h) psl(c,h), hi, [], [], ...
                         c, [1], [], [] , [], opt);
end

function [ peak ] = psl( c, h )
    N = length(c);
    XC = xcorr(c,h);
    pwr = XC .* conj(XC);
    pwr(N) = 0;  % Remove mainlobe
    peak = max(pwr);
end
```

Figure 4.6: MATLAB implementation of a linear programming solution for a minimum PSL filter.

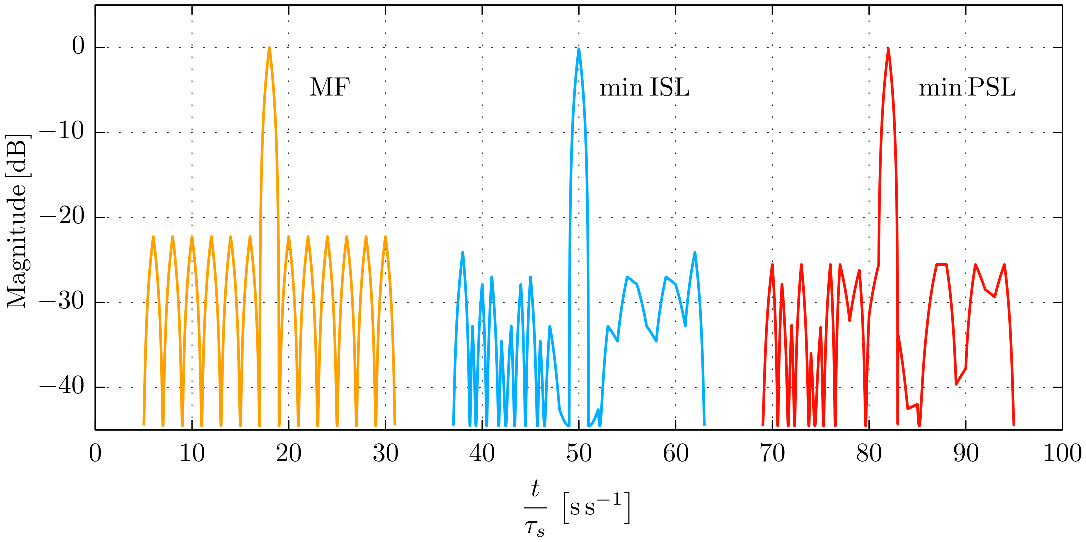

Figure 4.7: Response of matched, minimum ISL and minimum PSL filters of length 13 for the Barker-13 code.

filters.

The ISL and PSL of minimum ISL and minimum PSL filters of different length for the Barker-13 code are shown in Figure 4.8. As the filter length increases both the ISL and PSL are reduced. Long filters have the ability to reduce sidelobes at the expense of computational complexity.

The simulations in Section 4.2.3 exhibited large sidelobe levels; if a mismatched filter is used in these simulations, the sidelobes are suppressed substantially. Figure 4.9 compares the matched filter and mismatched minimum PSL length 39 filter performance when illuminating discrete scatterers. Mismatched filtering has reduced the range sidelobes by nearly 20 dB and all three scatterers are now clearly evident.

Figure 4.10 compares the matched filter and mismatched minimum ISL length 39 filter performance when illuminating a group of scatterers. The sidelobe leakage has been reduced to −40 dB and −30 dB before and after the group of scatterers. A close-up of the return from the group of scatterers on their own is shown in Figure 4.11; the response of the mismatched filter closely follows the true response, while the

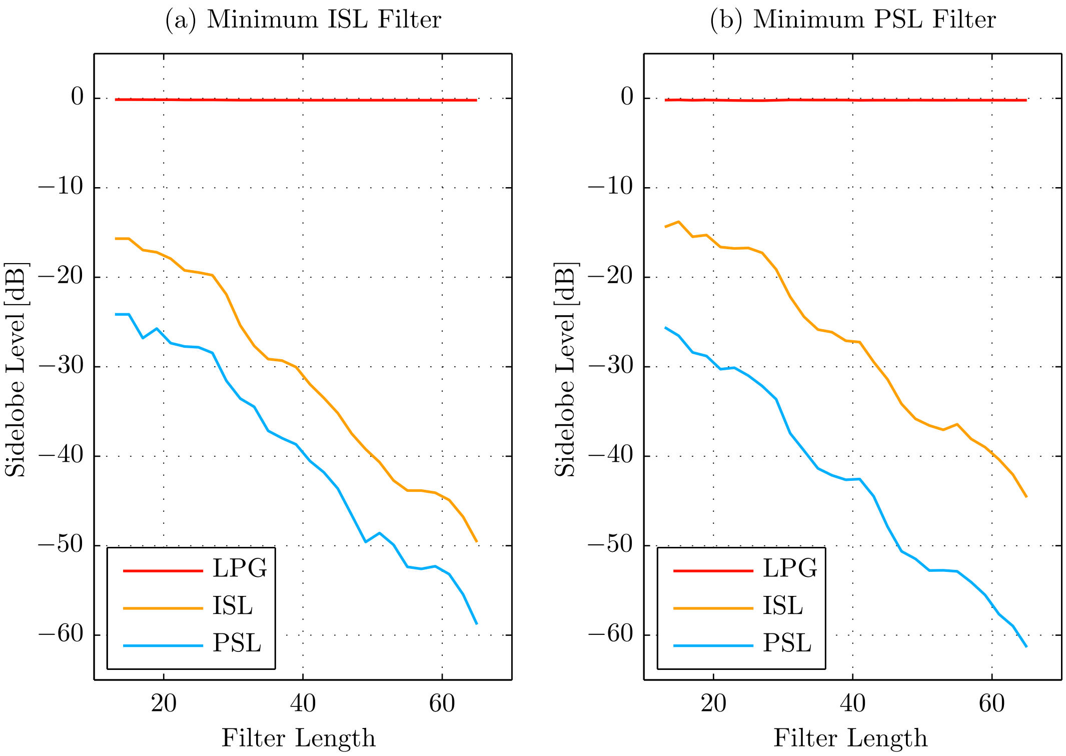

Figure 4.8: Barker-13 ISL and PSL performance as a function of mismatched filter length.

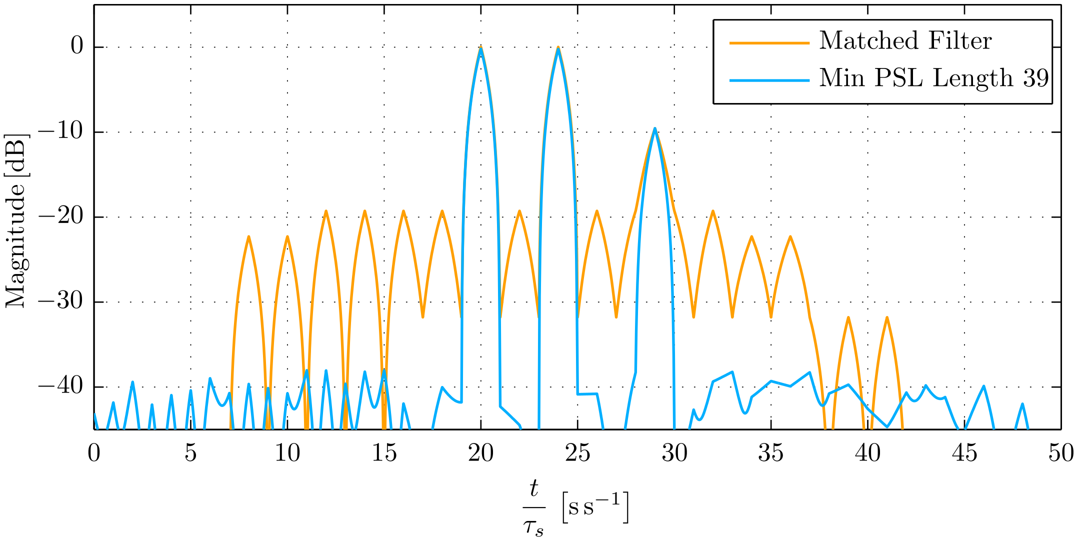

Figure 4.9: Simulation results for a Barker-13 coded pulse illuminating three discrete scatterers and processed with a mismatched minimum PSL length 39 filter.

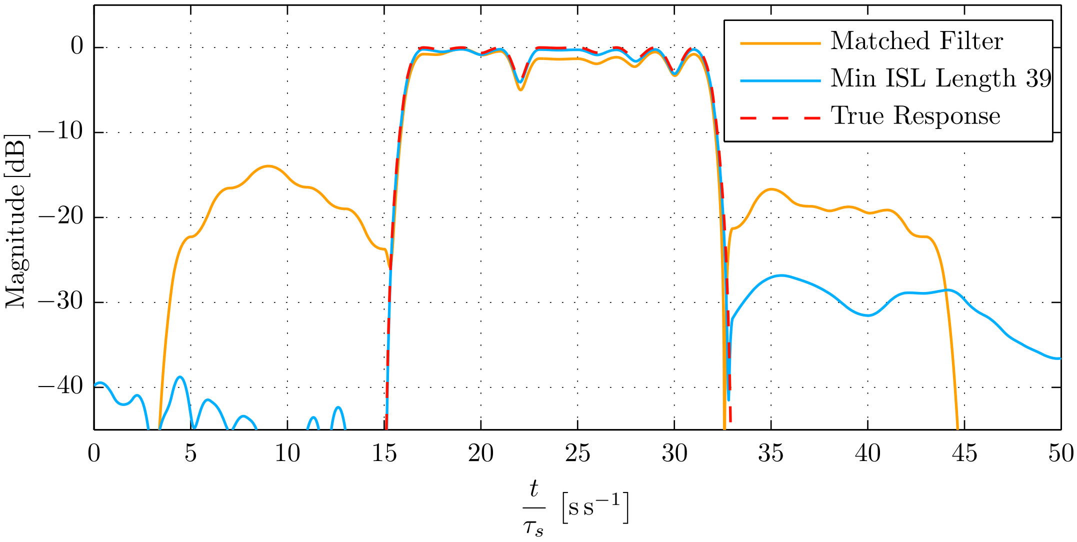

Figure 4.10: Simulation results for a Barker-13 coded pulse illuminating a continuum of scatterers and processed with a mismatched minimum ISL length 39 filter.

matched filter response exhibits a significantly larger deviation due to range sidelobe leakage. The small constant deviation from the true response can be attributed to the $-0.2\,\mathrm{dB}$ processing gain loss of this mismatched filter.

4.4 Code Selection Considerations

The process of code selection is best performed simultaneously with filter selection. The first consideration is to determine the length of the code. The two factors affecting this choice are

1. the maximum allowable pulse duration τ_m; determined by the capability of the transmitter and minimum imaging range, and

2. the desired range resolution δ_r; which is in turn limited by the transducer bandwidth and which sets the number of carrier cycles per code symbol.

The combination of these two parameters is used to compute the optimal code length:

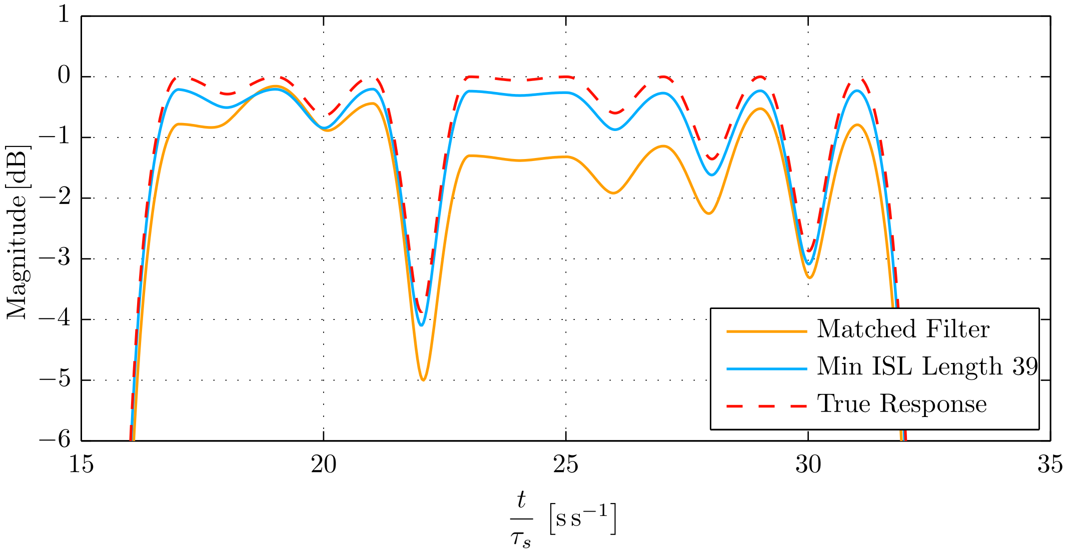

Figure 4.11: Simulation results for a Barker-13 coded pulse illuminating a continuum of scatters and processed with a mismatched minimum ISL length 39 filter. Expanded View.

$$N = \text{floor}\left(\frac{c\,\tau_m}{2\delta_r}\right) \tag{4.42}$$

Once the code length is determined, the next selection is the choice of code. Thus far only the binary Barker code has been introduced, however there are many other codes. Earlier in this chapter, for practical reasons, the set of symbols in a code sequence have been limited to have a constant magnitude. Codes such as these vary in phase, symbol to symbol, and can be grouped into one of two types:

1. Binary-phase codes, which restrict the phase of all symbols in the sequence to one of 0° or 180°, and

2. poly-phase codes, which allow the symbol phase to be arbitrary.

Binary-phase codes offer the simplicity of having to generate only two phases and if combined with a matched filter allow for simple processing that requires only additions. Poly-phase codes have traditionally been used in systems requiring high Doppler resilience; discretized versions of LFM or non-linear FM chirps are popular in such systems. In the case of a SBS system, Doppler is negligible therefore this thesis focuses on binary-phase codes.

Two classes of binary-phase codes that are most tailored to pulse compression are

1. optimal PSL codes, and
2. optimal ISL codes, traditionally referred to as optimal *merit factor* (MF) in literature.

Optimal-PSL codes are constructed such that the peak auto-correlation sidelobe is minimal for a given length of code. These codes have been found through exhaustive search for all code lengths up to length 61 [36]. The Barker codes are a special subset of optimal-PSL codes where the peak sidelobe is 1; a limitation of Barker codes is that they only exist for lengths up to 13, and it is conjectured that none exist beyond this length [37]. It has also been shown in literature that there are no even length Barker codes and that there are no other Barker codes shorter than 10^{20} in length. Even if a very long Barker code is found it would be impractical to use. The group of optimal-PSL codes is most useful in situations where there is a small set of discrete scatterers as discussed in Section 4.2.3.

Optimal-MF codes are a set of sequences for which the *merit factor* (MF) has been maximized. The MF was first defined by Golay in 1977 [38] and can be thought of as the inverse of ISL:

$$\mathrm{MF} = \frac{N^2}{\sum_{k \neq 0} R_{\mathbf{cc}}\left[k\right] R^*_{\mathbf{cc}}\left[k\right]} \tag{4.43}$$

The optimal-MF codes are typically applied when the return consists of a continuous signals generated by a large number of scatterers as discussed in Section 4.2.3. The optimal-MF codes for lengths up to 60 have been discovered through exhaustive searches, and very good codes with MF > 8.0 are known for most lengths between 100 and 200 [39].

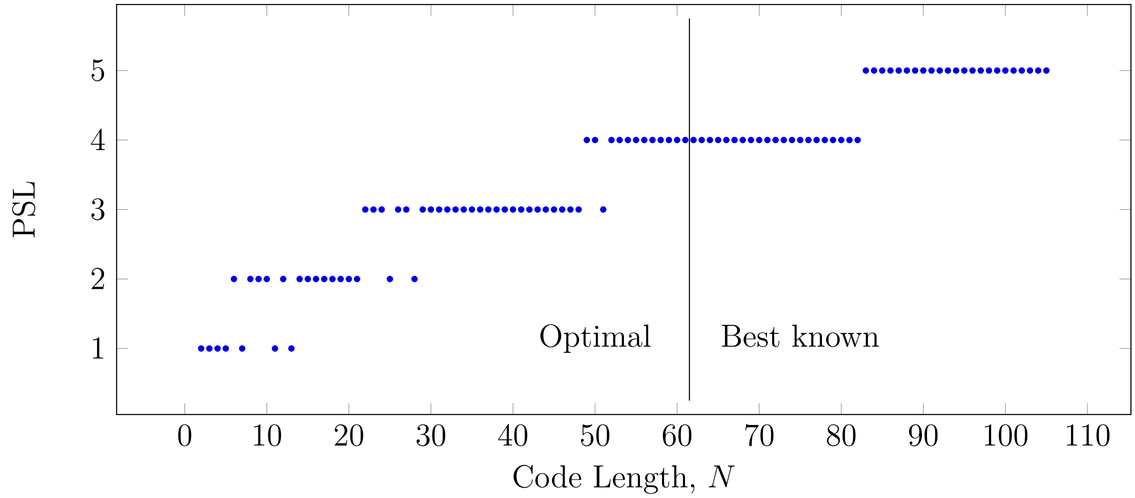

Figure 4.12: Peak sidelobe level of known optimal PSL codes of different lengths. [37]

Code	PSL	MF	ISL (dB) for Filter Length			PSL (dB) for Filter Length		
			$1N$	$3N$	$5N$	$1N$	$3N$	$5N$
OPS42 & OMF42	3	8.73	-13.0	-24.4	-35.9	-22.3	-33.3	-44.0
OPS43	3	6.75	-12.4	-29.4	-44.5	-23.5	-40.4	-55.7
OMF43	5	8.48	-10.6	-16.0	-18.5	-19.8	-29.6	-35.1

Table 4.1: Results of optimal PSL and MF codes of length 42 and 43 mismatched filtered with minimum ISL filters of length $1N$, $3N$ and $5N$.

It has been this authors experience that for some lengths such as $N = 42$, the same code meets both the optimal-MF and optimal-PSL conditions. Starting with one of these codes gives a high probability of good results, however it does not guarantee that the code and mismatched filter pair will be optimal. Therefore, the code and filter choice must be made simultaneously.

An example of this process is shown in Table 4.1, where the code length N is chosen to be 42 or 43. Three codes and their minimum ISL mismatched filters are evaluated. The best code is found to be the optimal-PSL length 43 code (OPS43) as long as the mismatched filter has a length equal to or greater than 129 or $3N$. This code significantly outperforms the other two despite the fact that it has the least favourable MF.

4.5 Code-Filter Performance Analysis

This section analyzes particular codes of interest to this thesis. Each code's symbol sequence is given in one of two notations. For binary phase codes, a hexadecimal notation is used where each bit represents one symbol of unity magnitude, and the bit value is the symbol's phase; 0 is 0° and 1 is 180°. For poly-phase codes, a comma separated list of the phase of each symbol in degrees is used.

4.5.1 Barker 13

The Barker 13 sequence (B13) is the longest known binary phase code with a peak sidelobe of 1 [37]. The auto-correlation of the Barker 13 is either 0 or ±1 at all lags except 0 where it is 13. The sequence for the code is given below (4.44) in hexadecimal notation:

$$\text{Barker13} \rightarrow \texttt{13'h\,1F35} \tag{4.44}$$

The performance of the Barker 13 code has been extensively studied in this thesis. Table 4.2 shows the results. The performance of the minimum ISL filter at a length of $5N = 65$ should be highlighted because it is exceptionally good. The integrated sidelobes are suppressed to $-50\,\text{dB}$ and the peak sidelobe is suppressed to $-59\,\text{dB}$ with a small $-0.2\,\text{dB}$ loss in processing gain. This code is used extensively throughout the thesis to demonstrate and experimentally verify pulse compression.

```
=== Matched Filter Results =======================================
Code Length,                 N   :    13
Peak Sidelobe,               PS  :     1
Merit Factor,                MF  :  14.1
Processing Gain,             PG  :  11.1 dB
Peak Sidelobe Level,         PSL : -22.3 dB
Integrated Sidelobe Level,   ISL : -11.5 dB

=== Mismatched Minimum ISL Filter Results =======================
Filter Length,               N   :    13         39         65
Loss in Processing Gain,     LPG :  -0.1 dB    -0.2 dB    -0.2 dB
Peak Sidelobe Level,         PSL : -24.1 dB   -38.7 dB   -58.8 dB
Integrated Sidelobe Level,   ISL : -15.7 dB   -30.0 dB   -49.6 dB

=== Mismatched Minimum PSL Filter Results =======================
Filter Length,               N   :    13         39         65
Loss in Processing Gain,     LPG :  -0.2 dB    -0.2 dB    -0.2 dB
Peak Sidelobe Level,         PSL : -25.6 dB   -42.6 dB   -61.3 dB
Integrated Sidelobe Level,   ISL : -14.4 dB   -27.1 dB   -44.6 dB
```

Table 4.2: Performance analysis of Barker 13 code.

4.5.2 Optimal PSL 28

The optimal PSL length 28 (OPS28) sequence [40] is the longest binary phase code with a peak auto-correlation sidelobe of 2. At more than twice the length of the Barker-13, its peak sidelobe level is lower $\frac{2}{28} \approx -23\,\text{dB}$. The sequence for the code is given below (4.45) in hexadecimal notation:

$$\text{OPS28} \rightarrow \texttt{28'h\,8F1112D} \tag{4.45}$$

The performance of OPS28 is shown in Table 4.3. Although the auto-correlation properties of the code are favourable; it has a low peak sidelobe and a high merit factor; the code under performs the Barker 13 in terms of sidelobe suppression and processing gain loss. The code does have a 3 dB advantage in overall processing gain due to its longer length. However, better codes near to this length exist, such as the optimal MF length 27 code.

```
=== Matched Filter Results ======================================
Code Length,                N   :    28
Peak Sidelobe,              PS  :     2
Merit Factor,               MF  :   7.8
Processing Gain,            PG  :  14.5 dB
Peak Sidelobe Level,        PSL : -22.9 dB
Integrated Sidelobe Level,  ISL :  -8.9 dB

=== Mismatched Minimum ISL Filter Results =======================
Filter Length,              N   :    28         84        140
Loss in Processing Gain,    LPG :  -0.3 dB    -0.9 dB    -1.2 dB
Peak Sidelobe Level,        PSL : -21.3 dB   -31.6 dB   -40.8 dB
Integrated Sidelobe Level,  ISL : -11.3 dB   -19.2 dB   -27.2 dB

=== Mismatched Minimum PSL Filter Results =======================
Filter Length,              N   :    28         84        140
Loss in Processing Gain,    LPG :  -0.3 dB    -0.8 dB      -
Peak Sidelobe Level,        PSL : -24.9 dB   -37.1 dB      -
Integrated Sidelobe Level,  ISL :  -9.1 dB   -17.3 dB      -
```

Table 4.3: Performance analysis of optimal PSL length 28 code.

4.5.3 Optimal MF 27

The optimal merit factor length 27 code (OMF27) has the highest known MF amongst binary codes other than the Barker codes [37]. The code has an auto-correlation peak sidelobe of 3 and a merit factor of 9.9. The sequence for the code is given below (4.46) in hexadecimal notation:

$$\text{OMF27} \rightarrow \texttt{27}'\texttt{h}\,\texttt{70EEED2} \tag{4.46}$$

The performance of OMF27 is shown in Table 4.4.

```
=== Matched Filter Results =======================================
Code Length,                N   :    27
Peak Sidelobe,              PS  :     3
Merit Factor,               MF  :   9.9
Processing Gain,            PG  :  14.3 dB
Peak Sidelobe Level,        PSL : -19.1 dB
Integrated Sidelobe Level,  ISL :  -9.9 dB

=== Mismatched Minimum ISL Filter Results =======================
Filter Length,              N   :    27          81        135
Loss in Processing Gain,    LPG :  -0.2 dB    -0.5 dB    -0.6 dB
Peak Sidelobe Level,        PSL : -21.5 dB   -35.2 dB   -45.7 dB
Integrated Sidelobe Level,  ISL : -12.1 dB   -22.9 dB   -33.3 dB

=== Mismatched Minimum PSL Filter Results =======================
Filter Length,              N   :    27          81        135
Loss in Processing Gain,    LPG :  -0.5 dB    -0.5 dB    -0.6 dB
Peak Sidelobe Level,        PSL : -25.1 dB   -39.9 dB   -51.1 dB
Integrated Sidelobe Level,  ISL :  -9.7 dB   -20.4 dB   -29.9 dB
```

Table 4.4: Performance analysis of optimal MF length 27 code.

4.5.4 Optimal PSL and Optimal MF 42

The code presented in this section labelled OPS42 / OMF42 is both optimal in PSL and MF for length 42 [40]. The code has an optimal auto-correlation peak sidelobe of 3 and a maximum merit factor of 8.7. The sequence for the code is given below (4.47) in hexadecimal notation:

$$\mathrm{OPS42} \,/\, \mathrm{OMF42} \rightarrow \texttt{42'h}\,\texttt{04447B874B4} \tag{4.47}$$

The performance of OPS42 / OMF42 is shown in Table 4.5.

```
=== Matched Filter Results =======================================
Code Length,                N   :    42
Peak Sidelobe,              PS  :     3
Merit Factor,               MF  :   8.7
Processing Gain,            PG  :  16.2 dB
Peak Sidelobe Level,        PSL : -22.9 dB
Integrated Sidelobe Level,  ISL :  -9.4 dB

=== Mismatched Minimum ISL Filter Results =======================
Filter Length,              N   :    42        126        210
Loss in Processing Gain,    LPG :  -0.4 dB    -0.6 dB    -0.7 dB
Peak Sidelobe Level,        PSL : -22.3 dB   -33.3 dB   -44.0 dB
Integrated Sidelobe Level,  ISL : -13.0 dB   -24.4 dB   -35.9 dB

=== Mismatched Minimum PSL Filter Results =======================
Filter Length,              N   :    42        126        210
Loss in Processing Gain,    LPG :  -0.5 dB    -0.7 dB    -0.7 dB
Peak Sidelobe Level,        PSL : -27.2 dB   -37.7 dB   -49.8 dB
Integrated Sidelobe Level,  ISL :  -9.7 dB   -18.3 dB   -27.9 dB
```

Table 4.5: Performance analysis of optimal PSL / MF length 42 code.

4.5.5 Optimal MF 43

The optimal merit factor length 43 code is presented here to show its less than optimal performance when compared to OPS42/OMF42 and OPS43. The sequence for the code is given below (4.48) in hexadecimal notation:

$$\text{OMF43} \rightarrow \texttt{43'h\,5CF1ABF92C8} \tag{4.48}$$

The performance of OMF43 is shown in Table 4.6.

```
=== Matched Filter Results ======================================
Code Length,                 N   :    43
Peak Sidelobe,               PS  :     5
Merit Factor,                MF  :   8.5
Processing Gain,             PG  :  16.3 dB
Peak Sidelobe Level,         PSL : -18.7 dB
Integrated Sidelobe Level,   ISL :  -9.3 dB

=== Mismatched Minimum ISL Filter Results =======================
Filter Length,               N   :    43        129        215
Loss in Processing Gain,     LPG :  -0.1 dB    -0.4 dB    -0.7 dB
Peak Sidelobe Level,         PSL : -19.8 dB   -29.6 dB   -35.1 dB
Integrated Sidelobe Level,   ISL : -10.6 dB   -16.0 dB   -18.5 dB

=== Mismatched Minimum PSL Filter Results =======================
Filter Length,               N   :    43        129        215
Loss in Processing Gain,     LPG :  -0.7 dB    -0.7 dB      -
Peak Sidelobe Level,         PSL : -24.9 dB   -35.1 dB      -
Integrated Sidelobe Level,   ISL :  -7.1 dB   -13.3 dB      -
```

Table 4.6: Performance analysis of optimal MF length 43 code.

When mismatch filtered, this code and filter pair exhibits sub-par performance compared to codes of similar length despite its large and favourable merit factor. This code highlights the importance of choosing the code and filter pair simultaneously.

4.5.6 Optimal PSL 43

The optimal peak sidelobe code of length 43 designated OPS43 has both favourable auto-correlation properties and generates a good code filter pair. The sequence for the code is given below (4.49) in hexadecimal notation:

$$\text{OPS43} \rightarrow \texttt{43'h 005B2ACCE1C} \tag{4.49}$$

The performance of OMF43 is shown in Table 4.7.

```
=== Matched Filter Results ======================================
Code Length,                 N   :    43
Peak Sidelobe,               PS  :     3
Merit Factor,                MF  :   6.7
Processing Gain,             PG  :  16.3 dB
Peak Sidelobe Level,         PSL : -23.1 dB
Integrated Sidelobe Level,   ISL :  -8.3 dB

=== Mismatched Minimum ISL Filter Results =======================
Filter Length,               N   :    43        129        215
Loss in Processing Gain,     LPG :  -0.4 dB    -0.8 dB    -0.8 dB
Peak Sidelobe Level,         PSL : -23.5 dB   -40.4 dB   -55.7 dB
Integrated Sidelobe Level,   ISL : -12.4 dB   -29.4 dB   -44.5 dB

=== Mismatched Minimum PSL Filter Results =======================
Filter Length,               N   :    43        129        215
Loss in Processing Gain,     LPG :  -0.5 dB    -0.7 dB    -0.8 dB
Peak Sidelobe Level,         PSL : -28.0 dB   -46.4 dB   -60.6 dB
Integrated Sidelobe Level,   ISL : -10.2 dB   -25.1 dB   -38.4 dB
```

Table 4.7: Performance analysis of optimal PSL length 43 code.

The code filter pair exhibits good sidelobe suppression and an acceptable processing gain loss. This is the second code of interested used throughout the thesis along with the Barker 13.

4.5.7 M-Sequence 31

M-sequence is a maximum length pseudo-random binary sequence generated through the use of *linear feedback shift registers* (LFSR). This particular sequence is of interest historically because it was used in a Soviet over-the-horizon radar system. The sequence was observed by ham radio operators for over a decade from 1976 until 1989 and dubbed as the Russian Woodpecker. The system used 4 transmitter with different m-sequence codes of length 31, one of which is listed in below

$$\text{MSEQ31} \rightarrow \texttt{31'h}\,\texttt{7C6EA12C} \tag{4.50}$$

and is generated from the LFSR polynomial $p(x) = x^5 + x^3 + 1$. An interesting side note about m-sequences is that their merit factor approaches 3 asymptotically as the m-sequence length increases [41]. The performance of MSEQ31 is shown in Table 4.8.

```
=== Matched Filter Results ======================================
Code Length,                 N   :    31
Peak Sidelobe,               PS  :     5
Merit Factor,                MF  :   2.8
Processing Gain,             PG  :  14.9 dB
Peak Sidelobe Level,         PSL : -15.8 dB
Integrated Sidelobe Level,   ISL :  -4.5 dB

=== Mismatched Minimum ISL Filter Results =======================
Filter Length,               N   :    31         93        155
Loss in Processing Gain,     LPG :  -0.5 dB    -1.8 dB    -2.6 dB
Peak Sidelobe Level,         PSL : -17.4 dB   -26.1 dB   -33.6 dB
Integrated Sidelobe Level,   ISL :  -6.5 dB   -14.0 dB   -19.9 dB

=== Mismatched Minimum PSL Filter Results =======================
Filter Length,               N   :    31         93        155
Loss in Processing Gain,     LPG :  -1.0 dB    -1.6 dB      -
Peak Sidelobe Level,         PSL : -21.5 dB   -33.2 dB      -
Integrated Sidelobe Level,   ISL :  -4.7 dB   -11.8 dB      -
```

Table 4.8: Performance analysis of m-sequence length 31 code.

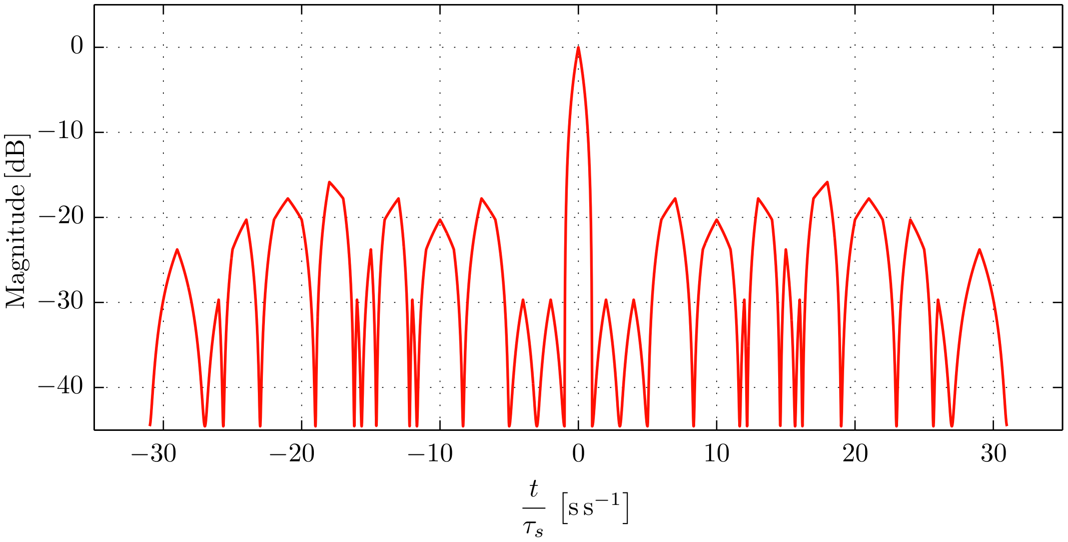

Figure 4.13: Auto-correlation of m-sequence length 31 code.

Although this code does not perform particularly well, the auto-correlation is interesting in that it exhibits low −30 dB sidelobes near the mainlobe as seen in Figure 4.13. The reduction of close-in sidelobes is useful in scenarios where few or possibly only 1 target is expected. The advantage of this code is the simplicity of the match filter, which would have been well within the capabilities of the hardware available in the 1970s and 80s.

4.5.8 Poly-phase Barker 9

The poly-phase[3] Barker 9 (PB9) is a 9 symbol code which meets the Barker condition $R_{\mathbf{cc}}(k)\, R^{*}_{\mathbf{cc}}(k) \leq 1 \,\text{for all}\, k \neq 0$ and is found in [42]. The sequence for the code is given below (4.51) in symbol phase notation:

$$\text{PolyBarker9} \rightarrow \{0, 0, 53.57, 42.22, 270.79, 215.59, 41.51, 161.92, 335.47\} \tag{4.51}$$

The performance of PB9 is shown in Table 4.9. This sequence performs extremely well with a very high merit factor and a small peak sidelobe 1.0.

```
=== Matched Filter Results =======================================
Code Length,                 N   :     9
Peak Sidelobe,               PS  :   1.0
Merit Factor,                MF  :  37.8
Processing Gain,             PG  :   9.5 dB
Peak Sidelobe Level,         PSL : -19.1 dB
Integrated Sidelobe Level,   ISL : -15.8 dB

=== Mismatched Minimum ISL Filter Results ======================
Filter Length,               N   :     9         27         45
Loss in Processing Gain,     LPG :  -0.0 dB    -0.1 dB    -0.1 dB
Peak Sidelobe Level,         PSL : -19.6 dB   -40.6 dB   -61.5 dB
Integrated Sidelobe Level,   ISL : -16.1 dB   -36.0 dB   -56.0 dB
```

Table 4.9: Performance analysis of poly-phase Barker length 9 code.

The next highest sidelobe after the 1.0 sidelobe found at $k = \pm(N-1)$ has a magnitude of 0.11. This is illustrated in Figure 4.14.

The MATLAB based method used to generate minimum PSL filters does not work on complex numbers such as those found in poly-phase sequences, hence the results for minimum PSL filters are not shown.

---

[3] In the practical system the poly-phase symbols are quantized. For example the prototype sonar used in this thesis has the capability to generate any of 256 equally spaced phases around the unit circle.

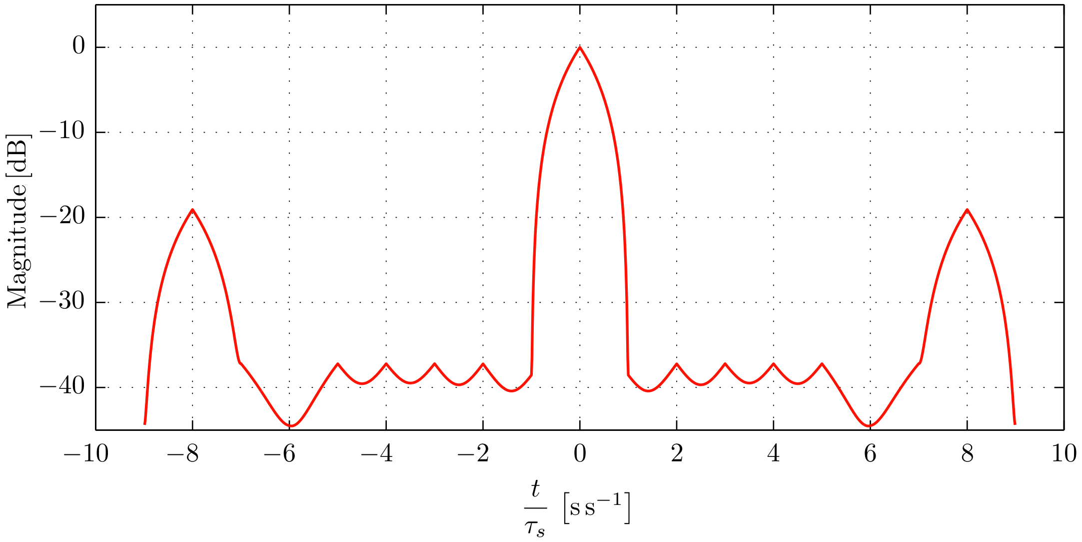

Figure 4.14: Auto-correlation of poly-phase Barker 9 code.

4.5.9 Poly-phase Barker 32

The poly-phase Barker 32 (PB32) is a 32 symbol code found in [43]. The sequence for the code is given below (4.52) in symbol phase notation:

$$\begin{aligned}\text{PolyBarker32} \;\rightarrow\; & \{\, 0.00, 0.09, 6.59, 119.23, 117.36, 109.06, 19.25, 57.08, \\ & 40.15, 155.19, -136.10, 166.69, 15.38, 30.28, -68.93, 96.17, \\ & 8.13, 28.24, -103.63, -170.91, -45.01, -117.97, 110.03, -78.43, \\ & 162.02, 45.40, 102.78 - 145.14, -8.17, 104.32, -120.09, 0.00 \,\}\end{aligned} \tag{4.52}$$

The performance of PB32 is shown in Table 4.10. This sequence performs extremely well with a very high merit factor and a small peak sidelobe 1.0. The PB32 code is the poly-phase code chosen for further experimental verification.

```
=== Matched Filter Results ======================================
Code Length,                 N   :    32
Peak Sidelobe,               PS  :   1.0
Merit Factor,                MF  :  34.9
Processing Gain,             PG  :  15.1 dB
Peak Sidelobe Level,         PSL : -30.1 dB
Integrated Sidelobe Level,   ISL : -15.4 dB

=== Mismatched Minimum ISL Filter Results =======================
Filter Length,               N   :    32          96         160
Loss in Processing Gain,     LPG :  -0.1 dB    -0.2 dB    -0.2 dB
Peak Sidelobe Level,         PSL : -28.8 dB   -44.3 dB   -59.2 dB
Integrated Sidelobe Level,   ISL : -17.5 dB   -32.8 dB   -48.1 dB
```

Table 4.10: Performance analysis of poly-phase Barker length 32 code.

4.6 Conclusion

The maximization of energy in the water is a key to improved performance of a sonar system. Many sonar systems already do this by driving the piezoceramic elements with the highest possible magnitude waveform. This combined with a longer duration coded pulse results in superior SNR performance without loss of resolution.

The choice of suitable code is a process of choosing both the transmit code and the filter used to compress it. The sets of optimal PSL and MF codes presented earlier in this section, found through exhaustive searches, are excellent candidates and typically exhibit good mismatched performance. The experiments in Chapter 7 use the codes presented here to examine the performance gains that pulse compression provides for SBS.

Chapter 5

Transmit Beamforming for Increased Backscatter Energy and Reduced Multipath Interference

A principal advantage of multi-element *swath bathymetry sidescan* (SBS) sonars over their interferometric counterparts is their ability to solve for more than one arrival. This capability is important in scenarios where the sea bottom features a complex geometry, the sea surface causes backscatter, or a combination of these which can result in multipath arrivals. The additional elements and processing of multi-element SBS systems affords the ability to solve for interfering angles of arrivals which can subsequently be separated or discarded. However, even with this ability, the presence of interfering arrivals degrades performance and increases the susceptibility of *angle-of-arrival* (AOA) processing to angle errors.

The current generation of SBS systems typically utilize a six to eight element linear array and solve for multiple simultaneous plane wave arrivals. Typically however, only two of the array elements are used on transmit. The two element transmit response of a typical SBS system generates a wide 55° fan-shaped acoustic illumination, and is generally tilted downward by 20° to 30° producing a strongly illuminated regions at nadir and near sea the surface. A natural extension to SBS systems is to make use of all available array elements on transmit in order to increase overall power in the water and to shape the angular distribution of the acoustic energy in the water, subject to specific imaging and mapping application goals under differing geometric conditions.

The objective of this chapter is to develop the concept of transmit beamforming, specifically steering and shading, as a means of increasing the backscatter energy and reducing multipath interference.

5.1 Typical Swath Bathymetry Sidescan Scenarios.

The three scenarios representing typical SBS sea floor imaging and bathymetry applications and geometries are:

A. A deep water scenario,

B. a shallow water near surface scenario, and

C. a shallow water mid water column scenario.

In **A**, the deep water scenario, the SBS is attached to a platform, such as an *autonomous underwater vehicle* (AUV) or a tow fish, and is far below the sea surface and free of its potential for generating interference. The absence of interference makes this scenario the simplest and most desirable.

In **B**, the shallow water near surface scenario, the SBS is mounted just below the water surface as is common for over-the-side mounted sonars, or towed sonars in shallow water. This scenario poses a challenge because of the close proximity of

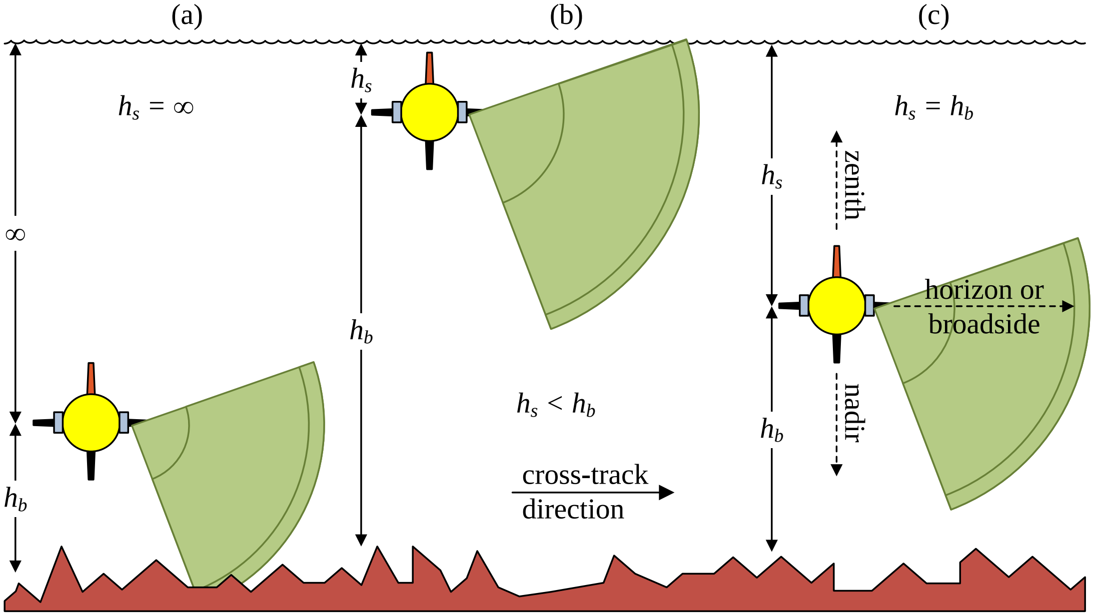

Figure 5.1: Three typical swath bathymetry sidescan operating scenarios.

the SBS to the sea surface. Any acoustic energy sent towards the sea surface will scatter, and either return to the sonar or cause a multipath illumination of the sea bottom. Additionally, a sea-floor to sea-surface multipath is also typically present and interferes with the direct path.

In **C**, the shallow water mid-column scenario, the SBS is considered to be near the centre of the water column, approximately equidistant from both the bottom and the surface. This scenario is less problematic than the near surface scenario, and is representative of an actively stabilized towed sonar or a shallow water AUV application.

Figure 5.1 illustrates the three scenarios and defines three orientation terms used throughout this chapter:

1. *Nadir* is directly under the sonar system at 90° below horizontal,
2. *zenith* is directly above the sonar system at $-90°$ above horizontal, and
3. *horizon* or *broadside* refers to the horizontal direction and are used interchange-

ably.

Any acoustic energy radiated between broadside and zenith is assumed to acoustically illuminate the sea surface, except in scenario **A**. Any acoustic energy radiated between broadside and nadir is assumed to acoustically illuminate the sea bottom. Finally, any acoustic energy radiated at angles beyond nadir produces illumination of the sea bottom on the opposite side of the sonar and interferes with operation of the complementary side transducer.

With these scenarios in mind and a general understanding of where energy is most beneficial and most detrimental, a cursory evaluation of common transmit beampatterns can be performed. Using simulations, the transmit intensity and energy distribution produced by different transmit array beampatterns is evaluated. The first step in this analysis is to derive the acoustic transmit beampattern of an SBS array.

5.2 Acoustic Beampattern Design.

An SBS array features a fan-shaped beam pattern, narrow in the alongtrack direction, and, in general, wide in the crosstrack direction. For the purpose of this analysis, only the beampattern response of the array in the crosstrack direction is considered. The following crucial parameters influence the beampattern in the crosstrack direction:

1. The number of elements N in the SBS discrete element linear array,
2. the single element response $b_1(\theta)$, often approximately omnidirectional,
3. the spacing of the elements d, typically regular and $\lambda/2$, and
4. the complex weights $\mathbf{a}$ applied to each element during transmit.

The typical aperture of SBS arrays is relatively small (e.g. less than 5 wavelengths) in the crosstrack plane, and as a result the response is assumed to always be in the far-field.

5.2.1 Discrete Linear Array Transmit Beam-Pattern

Given an N element discrete linear array, its beampattern is the result of a combination of the single element response $b_1(\theta)$, the array element spacing d, and the applied complex element weights $\mathbf{a} = [a_0, a_1, \ldots, a_n]$ for $n = 0 \ldots N-1$. For the purpose of this analysis, the magnitude of the single element pattern is assumed to be approximated by an empirical equation

$$b_1(\theta) = \cos^{\theta^2}(\eta\theta) \tag{5.1}$$

where θ is the angle away from broadside, and η is a spreading factor that increases the width of the single element response. At broadside, $\theta = 0$, the element exhibits its maximum response of $b_1(0) = 1$. For the simulations presented here, the spreading factor is set to $\eta = 0.7$ in order to approximate the single element beampattern of the experimental transducer used in Chapters 7 and 8. The resulting single element pattern has a wide $-3\,\mathrm{dB}$ response of 122°.

Next, the array pattern produced by a set of specific element weights and element spacing must be determined. The far field response of a discrete element linear array with omnidirectional equidistant elements spaced by $\lambda/2$, and weighted by a set of complex coefficients, $\mathbf{a}$, can be expressed as a summation of the response of each element in the far field in the θ direction:

$$b_2(\theta) = \sum_{n=0}^{N-1} a_n \exp\left(-\jmath\pi n \sin\theta\right) \tag{5.2}$$

This summation is equivalent to beamforming or spacial filtering in the θ direction. The overall array pattern $b(\theta)$ can then be expressed as a multiplication of the two patterns, the single element pattern and the discrete element linear array pattern above:

$$b(\theta) = b_1(\theta)b_2(\theta) \tag{5.3}$$

The combination of (5.1), (5.2), and (5.3) allows for the estimation of a SBS array crosstrack beampattern in the far field.

5.2.2 The Typical Two Element Transmit Pattern

Sidescans and SBS systems typically use a one or two element wide pattern to illuminate the sea floor. Shown in Figure 5.2 is a two $\lambda/2$ element wide pattern, 1λ overall, commonly used in sidescan systems. The two elements in this pattern are driven in-phase at maximum amplitude, $\mathbf{a} = [1, 1]$. This will be the baseline pattern used for the remainder of the chapter. It exhibits a wide 58° mainlobe with 6 dB more power at its peak response than a single element.

The pattern also shows a substantial response outside of $0^\circ \leq \theta \leq 90^\circ$, which in the case of $\theta > 90^\circ$ causes cross illumination of the complementary sidescan side, while $\theta < 0^\circ$ causes upward illumination towards the sea surface. Both of these effects are detrimental to the operation of the system.

5.2.3 Fully Utilizing Available Elements

Since SBS systems typically employ six or more array elements for receive, additional transmit energy and directivity is available by also utilizing these elements on transmit. Unfortunately however, including additional elements also has the potential to form *nulls* in the acoustic radiation response. Nulls are regions where the

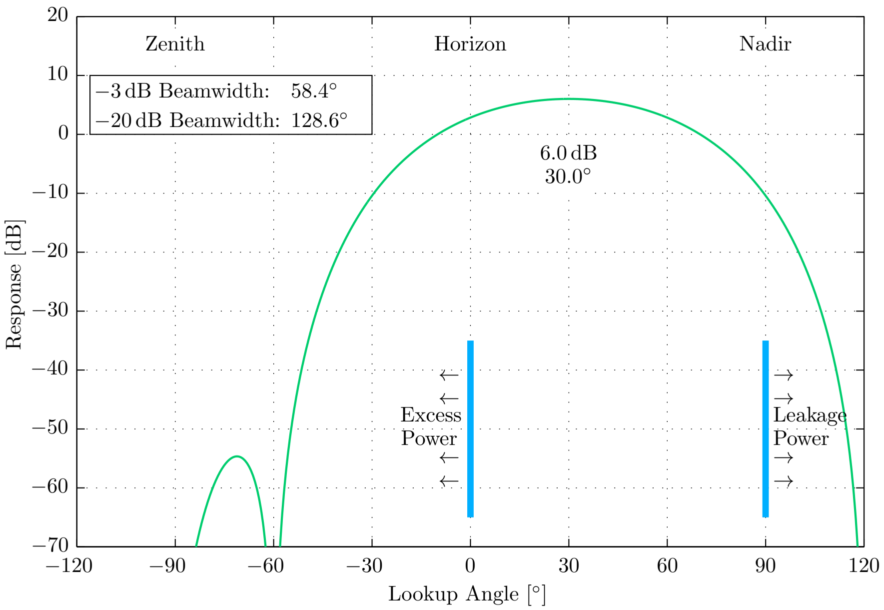

Figure 5.2: Acoustic radiation beampattern $b(\theta)$ of a two element $\lambda/2$ transducer array tilted 30° towards nadir.

acoustic energy generated by the elements interferes destructively and produces no acoustic backscatter. These nulls are undesirable for sea floor backscatter, but can be beneficial for suppression of interfering sea surface backscatter.

One often used method for removing nulls is *array shading*. This method progressively reduces the amplitude of the transmit signal applied to elements further away from the centre of the array. The implementation is generally accomplished using a set of real weights or coefficients, $\mathbf{w} = [w_0, w_1, \ldots, w_{N-1}]$, applied to the array transmit signals and computed from a windowing function such as hamming, hanning or kaiser.

In addition to modifying the beampattern, the utilization of additional elements on transmit also affords the ability to *steer* the beampattern. To implement beam steering the transmit signal driving each element is phase delayed in-order to shift the response of the mainlobe in a direction of interest. The steering coefficients combined with the shading coefficients, make the set of transmit signal weights $\mathbf{a}$ complex and can be represented as

$$\mathbf{a} = [a_0, a_1, \ldots, a_n] \tag{5.4}$$

$$a_n = w_n \exp\left(-\jmath\phi_n\right) \tag{5.5}$$

$$\phi_n = n\pi \sin\theta_e \tag{5.6}$$

where θ_e is the electronic steering angle, the angle by which the mainlobe is shifted from broadside, and w_n are a set weights as defined by a specific window function applied for the purpose of suppressing nulls.

5.2.4 An Example Eight Element Transmit Pattern

This thesis proposes a new narrow 8-element transmit beam-pattern tailored for new generation SBS sonars. The new beampattern uses a normalized `hamming(8)` window (5.7), and phase shifts the elements to steer the mainlobe downward by 20°, $\theta_e = -20°$.

$$\mathbf{w} = [0.08, 0.27, 0.67, 1.00, 1.00, 0.67, 0.27, 0.08] \tag{5.7}$$

The response of this beam-pattern, shown in Figure 5.3, features a strong 12 dB mainlobe, a significant reduction in the power transmitted above the horizontal, and very little power transmitted at and beyond nadir. This beampattern is provides increased illumination further in crosstrack distance, as well as reduced sea surface illumination. In addition to increasing the transmit energy directed at the sea floor, the reduced sea surface illumination provides the added benefit of less sea surface backscatter interference for operating scenarios **B** and **C**. The objective of the next sections is to develop a means of determining bottom illumination strength using simulations, and to quantify the expected increase in illumination strength relative

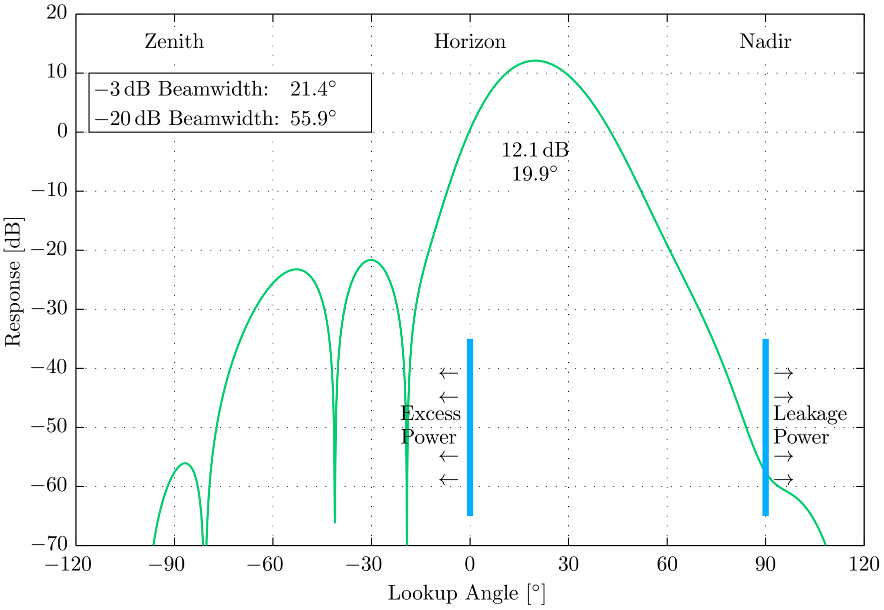

Figure 5.3: Acoustic radiation beampattern $b(\theta)$ of an eight element $\lambda/2$ transducer array shaded with the hamming window and electronically steered 20° towards nadir.

to the baseline results of the two element pattern.

5.3 Method For Analyzing Sea Bottom Illumination.

To analyze the illumination strength of different transmit beampatterns the sonar equation for received signal level RL, the parameter of interest, provides

$$RL = SL - TL + TS \tag{5.8}$$

where SL is the source level of the transducer including beam pattern and directivity effects, TL is the transmission loss, and TS is the target strength of the seafloor.

5.3.1 Source Level

The source level for a transducer in the θ direction is defined as

$$SL(\theta) = 10 \log P_1 + DI_A + DI_C(\theta) \tag{5.9}$$

where P_1 is the mean acoustic power out of a single element of the transducer, DI_A is the alongtrack transmit directivity, and $DI_C(\theta)$ is the crosstrack transmit directivity and is equivalent to $20 \log b(\theta)$.

5.3.2 Transmission Loss

The transmission loss is dependant on the range r to target and can be approximated by a two-way spherical spreading term plus a linear term to account for absorption loss,

$$TL(r) = 40 \log r + 2\alpha r \tag{5.10}$$

where α is the absorption coefficient at the frequency of interest. For an operating frequency of 450 kHz, $\alpha \approx 0.1\,\mathrm{dB/m}$ [44].

5.3.3 Target Strength

The target strength TS is combination of the sea-floor backscatter intensity SB and the illuminated area A:

$$TS(\theta, r) = SB(\theta) + 10 \log A(r) \tag{5.11}$$

For a swath sidescan SB is a function of θ and A is a function of r. The backscatter from the sea-floor is assumed to follow Lambert's law [44] which states that the backscatter is a function of the grazing angle θ of the pulse within the illuminated footprint

$$SB(\theta) = 10 \log \mu + 10 \log \sin^2 \theta \tag{5.12}$$

where μ is a proportionality constant and depends on sea-floor composition and the operating frequency of the sonar. Under the conditions of a medium sand sea-floor, $10 \log \mu$ is approximately $-25\,\mathrm{dB}$ [44]. The illuminated footprint area is calculated from the range, alongtrack beamwidth Θ_{A}, and the leading and trailing edges, l_+ and l_- respectively, of the pulse footprint:

$$A = r\Theta_{\mathrm{A}}\left(l_+ - l_-\right) \tag{5.13}$$

where

$$l_+ = \sqrt{\left(r + \frac{c\tau_p}{2}\right)^2 - h_f^2} \tag{5.14}$$

$$l_- = \sqrt{\left(r - \frac{c\tau_p}{2}\right)^2 - h_f^2} \tag{5.15}$$

and where τ_p is the duration of the transmitted pulse and h_f is the altitude above the sea-floor.

5.3.4 Crosstrack Directivity

The crosstrack directivity is derived from the transmit response pattern described in Section 5.2.1:

$$DI_C(\theta) = 20 \log b(\theta) \tag{5.16}$$

5.3.5 Overall Evaluation Equation

Equations (5.8) thru (5.16) can be combined into a single equations in order to analyze SBS transmit beampatterns by defining a receive signal figure, RSF:

$$RSF = RL - 10 \log P_1 - DI_A \tag{5.17}$$

$$= DI_C(\theta) - TL(r) + TS(\theta, r) \tag{5.18}$$

RSF is just the RL with terms that do not vary across beampattern or with crosstrack distance removed. Specifically, the acoustic power of a single element P_1, and the alongtrack directivity DI_A are constant and have been removed.

5.4 Analysis of Flat Sea Bottom Illumination

In this section, the equations derived previously are used to simulate the return from a flat bottom in scenario **A**, and the return from both a flat sea surface and sea bottom in scenarios **B** and **C**. The assumptions common to all three scenarios are listed:

1. The sea floor is a horizontal flat medium sand bottom with $10 \log \mu_f = -25\,\mathrm{dB}$,
2. the pulse length and speed of sound are $\tau_p = 20\,\mu\mathrm{s}$ and $c = 1480\,\mathrm{m\,s^{-1}}$,
3. the along-track beamwidth is $\Theta_A = 1°$,
4. the transducer is tilted 20° towards nadir for the 2-element transmit beam-pattern, and
5. the transducer is electronically steered 20° towards nadir for the 8-element transmit beam-pattern.

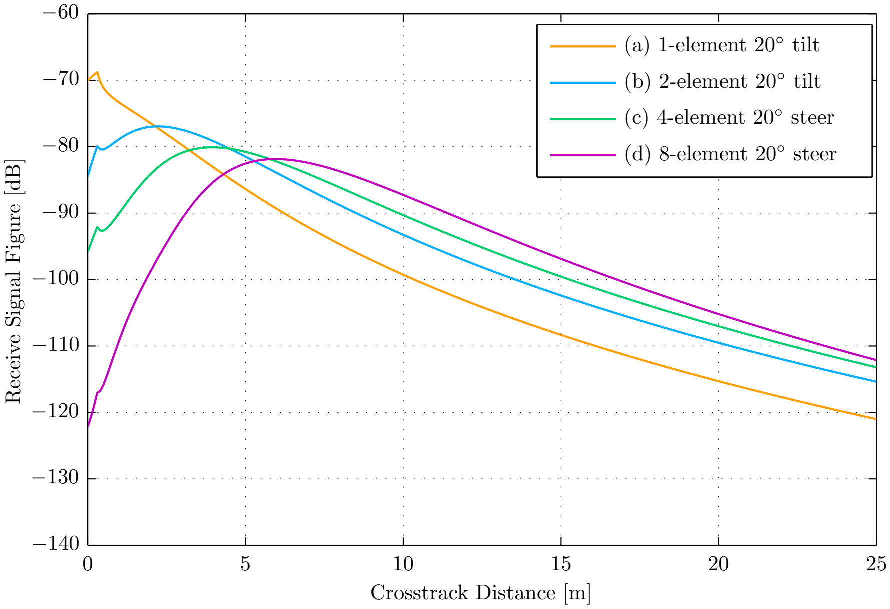

Figure 5.4: RSF for scenario A where the SBS is 4 m above the sea floor.

While other sonar parameters examples can also be applied, the purpose of this specific example is only to demonstrate a representative transmit illumination comparison for different realizable transmit beampatterns.

5.4.1 Scenario A

Scenario **A** simulates operation of an SBS system in deep water where the sea surface is not acoustically visible. Particular to scenario **A** is the following set of assumptions:

1. The sea surface is infinitely far away and hence not illuminated, and
2. the altitude of the SBS above the sea floor is $h_f = 4\,\mathrm{m}$.

Typical transmit patterns for SBS sonars mounted with a tilt of 20° direct significant transmit energy in the nadir direction as shown in Figure 5.4, where a much higher receive level is exhibited by traces a and b near nadir in comparison with the receive level at the maximum crosstrack distance.

The addition of transmit steering and shading allows the system to direct more energy towards the sea floor at the maximum crosstrack distance and less energy towards nadir, and flattens the RSF curve. Trace d show the RSF response for the designed 8-element transmit pattern. In the nadir direction, trace d dips to $-120\,\mathrm{dB}$, and this lower nadir response is the tradeoff for an increased response at the maximum crosstrack distance. For crosstrack distances greater than 10 m there is a 6.0 dB gain in receive level for the 8-element trace over trace b, the 2-element trace. This gain narrows to 3.3 dB at the maximum crosstrack distance, however it is still significant.

5.4.2 Scenario B

Scenario **B** simulates the operation of an SBS system in an over-the-side mount or shallow tow configuration. In particular the relative intensities of the backscatter from the sea surface and sea bottom are of interest. Scenario **B** makes the following set of assumptions:

1. The depth of the SBS below the sea surface is $h_s = 4\,\mathrm{m}$,
2. the reflectivity of the sea surface is $10 \log \mu_s = -25\,\mathrm{dB}$, and
3. the altitude of the SBS above the seafloor is $h_f = 16\,\mathrm{m}$.

The simulated results of scenario **B** are seen in Figure 5.5. For the 2-element array with 20° of tilt, the separation of the sea surface and sea floor backscatter intensity is $\approx 15\,\mathrm{dB}$ for the majority of the return. The intensity of the sea surface backscatter is significant enough that the SBS system must solve for the sea surface arrivals and discard them.

In the case of the 8-element array electronically steered to 20° with 0° of physical tilt, the near nadir separation is poor, however it quickly increases away from nadir, as shown in (b) of Figure 5.5. For crosstrack distances over 15 m the separation exceeds 25 dB. The added directivity of the 8-element transmit has reduced sea surface illumination by over 10 dB.

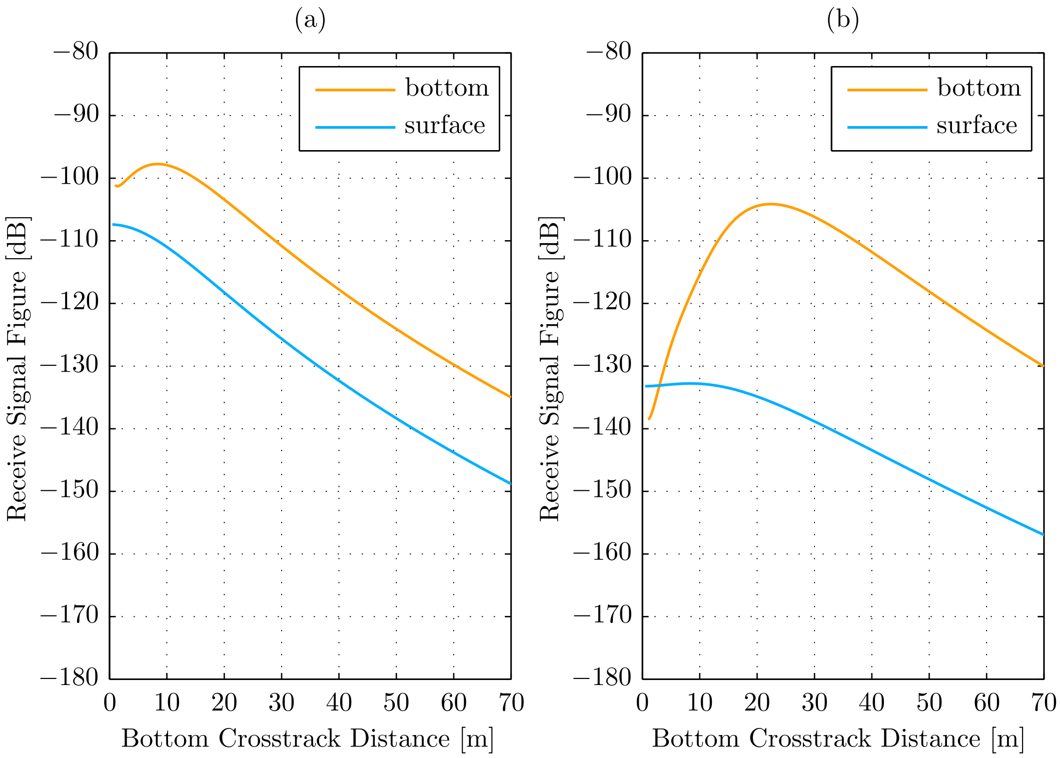

Figure 5.5: *RSF* for scenario B where the SBS is 4 m below the sea surface and 16 m above the sea floor. (a) 2-element transmit (b) 8-element transmit

5.4.3 Scenario C

Finally scenario **C** simulates the operation of an SBS system in a mid water column configuration in shallow water. Particular to scenario **C** is the following set of assumptions:

1. The depth of the SBS below the sea surface is $h_s = 10\,\mathrm{m}$,
2. the reflectivity of the sea surface is $10 \log \mu_s = -25\,\mathrm{dB}$, and
3. the altitude of the SBS above the seafloor is $h_f = 10\,\mathrm{m}$.

The results for scenario **C** are very similar to **B** as seen in Figure 5.6. The major difference being that the 2-element transmit beampattern shows even less intensity separation between the sea floor and sea surface backscatter. More specifically, the separation is less than 6 dB for the majority of the return. In this case, the SBS will

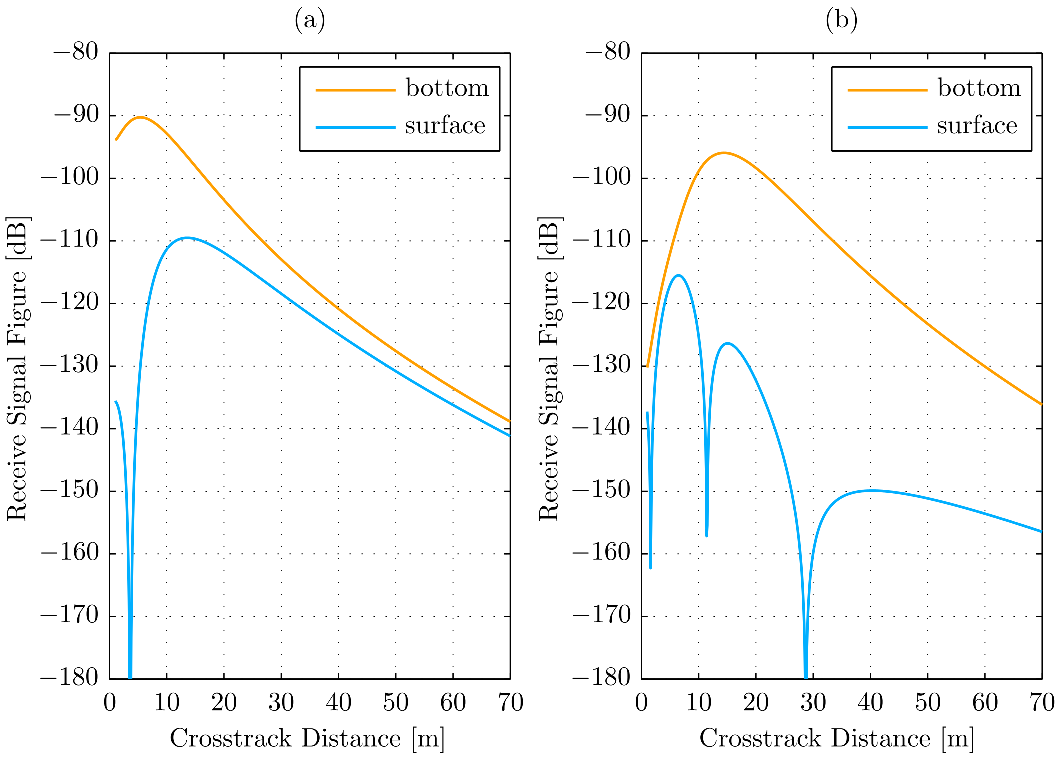

Figure 5.6: *RSF* for scenario C where the SBS is 10 m below the sea surface and 10 m above the sea floor. (a) 2-element transmit (b) 8-element transmit

need to solve for and discard the surface return in order to accurately profile the sea bottom. This requirement reduces the number of solutions available to accommodate interfering multipaths and/or complex sea bottom geometries.

The 8-element transmit beampattern in scenario **C** shows improved separation in the backscatter intensity of the sea bottom and sea surface. Near nadir performance is degraded, as expected, however at crosstrack distances greater than 10 m the separation again increases to more than 20 dB. Interestingly, the nulls of the transmit pattern can be seen in the illumination of the sea surface. These nulls are considered to be beneficial since they help to further suppress the sea surface return.

5.4.4 Conclusion

Utilization of all available transducer array elements has been shown to allow beneficial redistribution of the transmit energy. The redistribution provides for an increased in the backscatter intensity of the sea floor at far cross-track distances, and a reduction in the sea surface illumination and resulting backscatter. The higher intensity sea bottom illumination is expected to reduce the variance of bathymetric angle estimates, and at the same time extend the useable range of the SBS system. The reduction in interfering sea surface backscatter is also expected to improve the reliability of SBS angle estimates especially in scenarios featuring complex geometries and competing multipath arrivals.

In the next chapter, the prototype SBS sonar used in the experiments of Chapters 7 and 8 is presented. Chapter 8 provides an experimental investigation of the simulation finding of this chapter.

Chapter 6

The 3DSS-EX450 Experimental Swath Bathymetry Sidescan Sonar

The objective of this section is to describe the prototype sonar system used in the experiments described in the following chapters and that directly relate to the concepts and simulations introduced in the previous two chapters. The features of the prototype SBS which allow for more advanced operation are also highlighted. The experimental and highly configurable swath bathymetry sonar was provided by Ping DSP Inc. of Victoria, BC. This sonar system is uniquely suited in that it features flexible hardware and is highly programmable in .NET or using MATLAB.[1] The system consists of 5 major modules:

1. An 8 channel receiver with configurable frequency and electronically selectable bandwidth,
2. an 8 channel transmitter with programmable voltages and arbitrary 2 level waveform capability,
3. an 8 element SBS wideband transducer designed to operate at a centre fre-

---

[1] MATLAB is a widely used interpretive language for signal processing development and analysis of large data sets. MATLAB is a product of Mathworks Inc.

quency of 450 kHz,

4. an integration module providing Gigabit Ethernet communication and system power, and
5. a top-side computer executing MATLAB to control the system, process data, and generate displays.

The system also has several minor modules which include:

1. An 8 channel electronic *transmit receive* (T/R) switch which allows the system to transmit and receive on the same transducer elements,
2. an internal *motion reference unit* (MRU) which provides orientation and motion information referenced to the transducer position,
3. an internal water temperature measurement unit which allows for the estimation of sound velocity, and
4. up to 4 RS-485 ports for connecting an external MRU, GPS with pulse-per-second (PPS) signalling, sound velocity probe (SVP), and an external trigger.

The modular components are part of Ping DSP Inc's SoftSonar™ architecture, and are developed using *field programmable gate arrays* (FPGA) in-order to provide a highly flexible and software programmable platform for sonar development. The 3DSS™-EX450 sonar itself is identical to the 3DSS™-SX450 product sold by Ping DSP Inc but is extended to also include additional advanced configuration options.

6.1 Hardware

The following describes the sonar hardware used in the experiments in subsequent chapters.

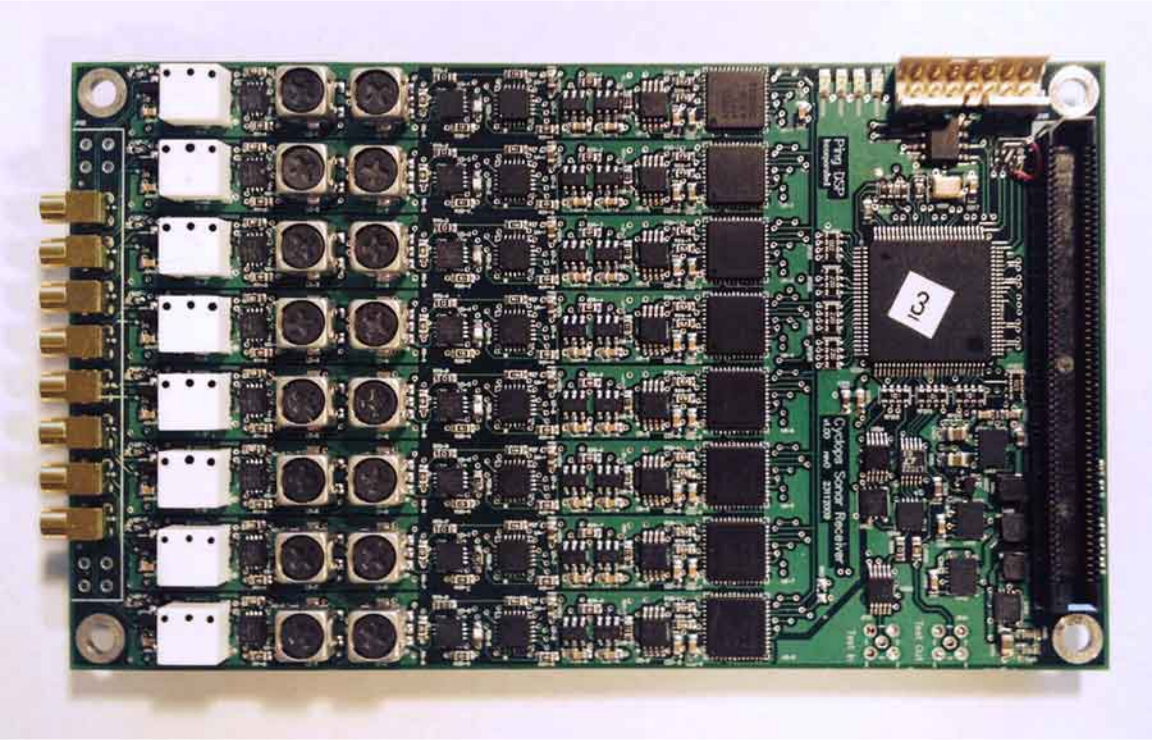

Figure 6.1: Photograph of SoftSonar™ 8 Channel Programmable Receiver.

6.1.1 SoftSonar™ Receiver Module

A photograph of the 8 channel SoftSonar receiver is shown in Figure 6.1.

The receiver comprises of 8 identical channels, each of which includes a low noise amplifier, a band-pass filter, a dynamically adjustable gain stage, and an *analog to digital converter* (ADC). The ADCs feed an FPGA which implements a digital down-converter, digital filters, and decimation. The use of the FPGA allows the receiver to adjust its digital filters, sample bandwidth, and centre frequency in a fashion similar to modern software defined radios.

6.1.2 SoftSonar™ Transmitter Module

A photograph of the 8 channel SoftSonar transmitter is shown in Figure 6.2.

Each transmit channel features a MOSFET output stage which is designed to directly drive a piezoceramic transducer. The output stage is powered by a pro-

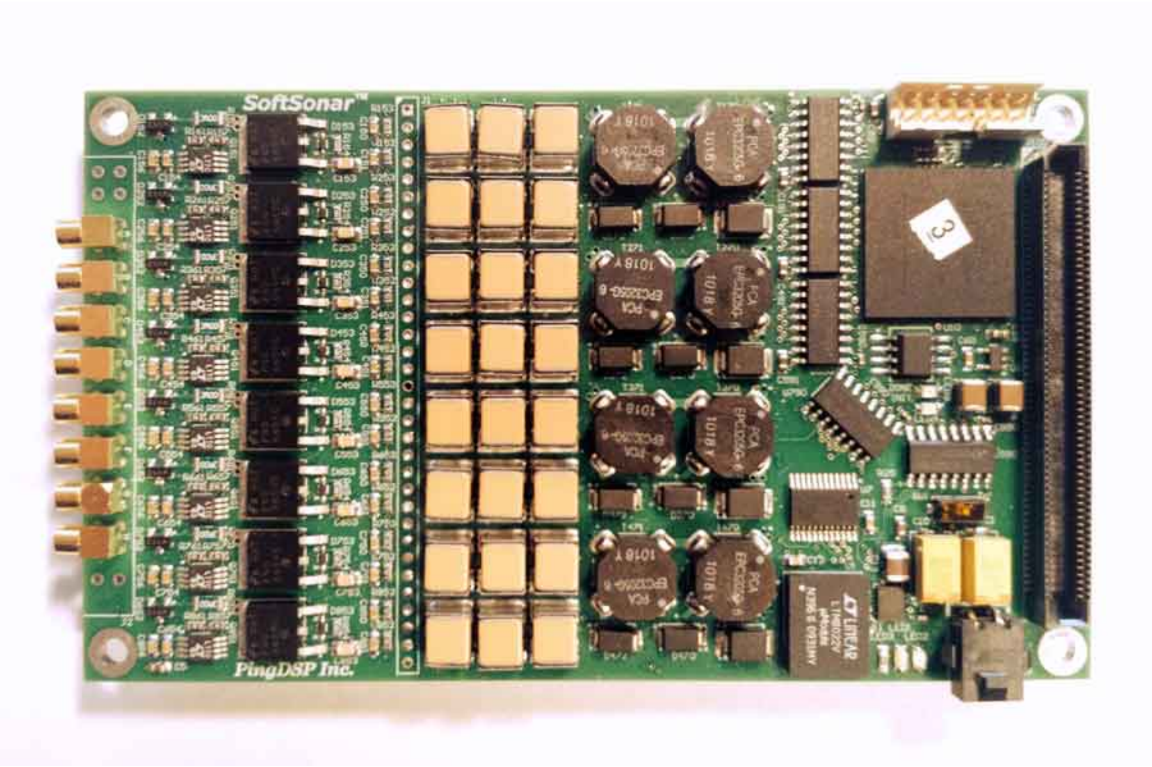

Figure 6.2: Photograph of SoftSonar™ 8 Channel Flexible Transmitter.

grammable voltage DC to DC converter that charges the bank of transmit capacitors to a voltage of up to ±250 V DC. Both the output stage and the programmable DC to DC converter are controlled by an FPGA which also stores an arbitrary binary pulse transmit waveform and phase delay coefficients for the 8 output channels. The arbitrary waveform capability allows transmission of coded pulses as needed for the pulse compression experiments described in Chapter 7. The ability to phase delay individual channels is integral to transmit steering, and the programmable transmit voltage is required for transmit beam shading and shaping. This capability is used in the experiments in Chapter 8.

6.1.3 3DSS™-450 Transducer

The third of the major components is the 8 channel SBS transducer. Two transducers were used during the experimental phase of this thesis.

The first is a transducer created by Simon Fraser University for the Department of Mechanical Engineering at the University of Victoria. Designed to function at 450 kHz, it features 8 linear elements of length $\approx 50\lambda$ and spaced a half wavelength apart for a total baseline of 3.5λ. Each element is made of *lead zirconate titanate* (PZT) a piezoceramic with a substantial piezoelectric effect. The single element response of the transducer exhibits a fan shaped acoustic one way beampattern of approximately 1° by 150°.

The second transducer was provided by Ping DSP Inc and is the same one used on their SX450 and DX450 SBS commercial systems. It also features 8 elements at $\lambda/2$ spacing, but has a significantly longer length of $\approx 95\lambda$. The single element response of the transducer features a fan shaped acoustic one way beampattern of approximately 0.57° by 150°.

6.1.4 SoftSonar™ Host Integration Module

This module interconnects and orchestrates the operation of all other modules as well as providing combined RS-485 and Ethernet communication to and from the sonar. The host module also provides power regulation and monitoring for the sonar system, and includes dedicated hardware *digital signal processors* (DSP) for embedded signal processing. And finally the host module also keeps accurate time, and timestamps sonar data as well as all serial data generated inside the sonar (e.g. MRU data) and received by the serial ports.

6.1.5 Top-side Computer and MATLAB

The final module is a top side computer which controls the sonar system, processes data, and generates data displays. MATLAB by Mathworks Inc is used for all of these functions and provides a convenient method for rapid development of custom sonar GUI's, processing, and display. A laptop with a dual or quad core Intel processor, 8 gigabytes of memory, and a large solid state drive for storage was used to provide real-time operation of all controls, processing, and display requirements of the experiments in Chapters 7 and 8.

6.2 Software

The high level MATLAB control, processing, and display capabilities of the EX450 sonar was provided using a combination of 3DSS and SoftSonar .NET libraries. These libraries provide for flexible control of sonars implemented using the SoftSonar modules and can be used directly from within MATLAB.

6.2.1 3DSS™ Application Programming Interface

The 3DSS™ *Application Programming Interface* (API) is a set of .NET classes compiled into DLL libraries that allow for the control of the 3DSS series of sonars. Through the API and an Ethernet connection to the sonar, it is possible to fully control the 3DSS-EX450. Through the API the programmer has control of parameters such as range, transmit shading, steering, pulse waveform, and pulse repetition rate. An example of how the 3DSS .NET API can be used inside or outside of MATLAB is provided in Figure 6.3.

6.2.2 MATLAB Processing

Further processing is done in MATLAB using a combination of functions. Of specific interest is the TLS AOA processing function. In Figure 6.4, the simplicity of implementing TLS AOA processing in MATLAB is shown.

The complete code is only 10 lines long excluding comments and blank spaces. It makes use of the `hankel` function to generate the sub-array sample matrix, performs

```
/******* Find and Connect to EX450 Sonar *******/
var mySonar = ThreeDssExSonar.FindFirst();
mySonar.Connect();

/******* Modify EX450 Sonar Settings ***********/
// Set data acquisition range to 75m:
mySonar.Range = 75.0;

// Set transmit pulse to Barker-13 16cps:
mySonar.Transmit.Pulse =
   Pulses.CreateBinaryCodedPulse(0x1F35, 13, 16);

// Set transmit steering angle to 20 degrees:
mySonar.Transmit.Angle = 20.0;

// Set transmit shading:
mySonar.Transmit.ElementShading =
   new double[]{0, 0, 0.42, 1, 1, 0.42, 0, 0};

// Set Average sound velocity (m/s):
mySonar.SoundVelocity = 1485.0;

// Set trigger to continuous 5 Hz
mySonar.Trigger.ContinuousRate = 5.0;
mySonar.Trigger.Source = TriggerSource.Continuous;

// Commit the settings to the sonar:
mySonar.Commit();

/******* Use Sonar for 100 Pings ***********/
for(int i=0; i<100; i++)
{
   // Read data
   var myData = mySonar.Read();

   // ... use data ...
}

// Disconnect from system:
mySonar.Disconnect();
```

Figure 6.3: C# Example of using the .NET 3DSS API to control the EX450 sonar.

```matlab
function [theta, mag, z] = aoa_tls(s , M)
    % Parameters:
    % s : complex sample vector
    % M : number of planewaves

    N = length(s);    % Number of elements
    if (N < 2*M)
        error('N must be greater than or equal to 2M');
    end

    % Generate sample subarray:
    S = hankel(s);
    S = S(1:(end-M),1:(M+1));

    % Solve min||Sw|| using SVD:
    [U,A,V] = svd(S);
    w = V(:,end);

    % Solve for roots of W(z):
    z = roots(w);

    % Compute the AOA of planewaves:
    theta = asin(angle(z) / pi);

    % Compute magnitude of planewaves:
    % ... skipped ...
end
```

Figure 6.4: A MATLAB Implementation of TLS Angle Of Arrival Processing.

SVD on the matrix using the `svd` function, and solves for the roots of the resulting polynomial using the `roots` function.

6.3 Conclusion

A brief overview of the experimental hardware and software has been provided in this chapter. The overview has highlighted the unique hardware features of the EX450 and the software flexibility afforded by its integration with MATLAB. The combination of these hardware and software features provide the required sonar functionality necessary for the transmit steering, shading, and pulse compression experiments. These experiments are performed for comparison with the simulation results from previous chapters. The next chapter makes use of the EX450 sonar for experiments into the benefits of transmit coding and pulse compression. Then in Chapter 8, a set of experiments are conducted to investigate the benefits of transmit steering and shading.

Chapter 7

Experimental Investigation of the Benefits of Pulse Coding

Chapter 4 introduced pulse compression and simulated the expected performance for two underwater acoustic application examples. The first example featured a discrete distribution of point targets which in turn produced discrete, time separated, acoustic returns. The second example featured a single distributed scatterer target, as a representation of the sea floor, producing continuous acoustic backscatter. In both scenarios, pulse compression increased the SNR of the backscatter. At the same time, the concept of pulse compression sidelobes was introduced and a method for suppressing these sidelobes through mismatched filtering was investigated.

To compare and contrast with the simulated results of Chapter 4, two experiments were devised to represent the two simulated scenarios and refute or confirm the benefits of pulse compression as applied to SBS. The expected improvement in SNR is also expected to yield a lower variance in the angle estimates and in doing so provide improved bathymetric results.

The first experiment was conducted at the University of Victoria Underwater Research Facility. The test facility created by Dr. Brad Buckham for the purpose of testing control systems for remotely operated vehicles. It was built around a boathouse at the Van Isle Marina in Sidney, BC and features an enclosed area of tidal water approximately 10 feet deep at low tide and accessible from three sides. The facility also includes an insulated office with a work area for computer and other equipment. The facility was used for experiments with the prototype sonar in which three precisely positioned targets [1] of differing diameters were acoustically illuminated and the returned echoes recorded. In the experiments, the sonar employed both simple gated or rectangular pulses as well as varying length coded pulses to measure the range and angle to the three pipes which appeared as discrete targets. The strength of the backscatter returned by the three targets was measured and the SNR for each was estimated. The variance in the angle estimate for each target over a set of pings was also determined. The measurements afford quantitative analysis of the performance improvement resulting from the use of pulse coding and subsequent compression.

The second experiment was conduced at the Saanich Commonwealth Place swimming pool. One side wall of the 50 m competition swimming pool was used as a long continuous target representative of a flat sea bottom. The sonar was placed in a mounted vertically in a precise position at one end of the pool and used to image the 50 m long side wall with both coded and uncoded pulses. The strength of the continuous backscatter signal and the ping-to-ping variance of the measured angles along the wall were determined in each case. The results of the experiments are described in Section 7.2.

---

[1] Two targets were vertical pipes made of PVC, while the other was a rope.

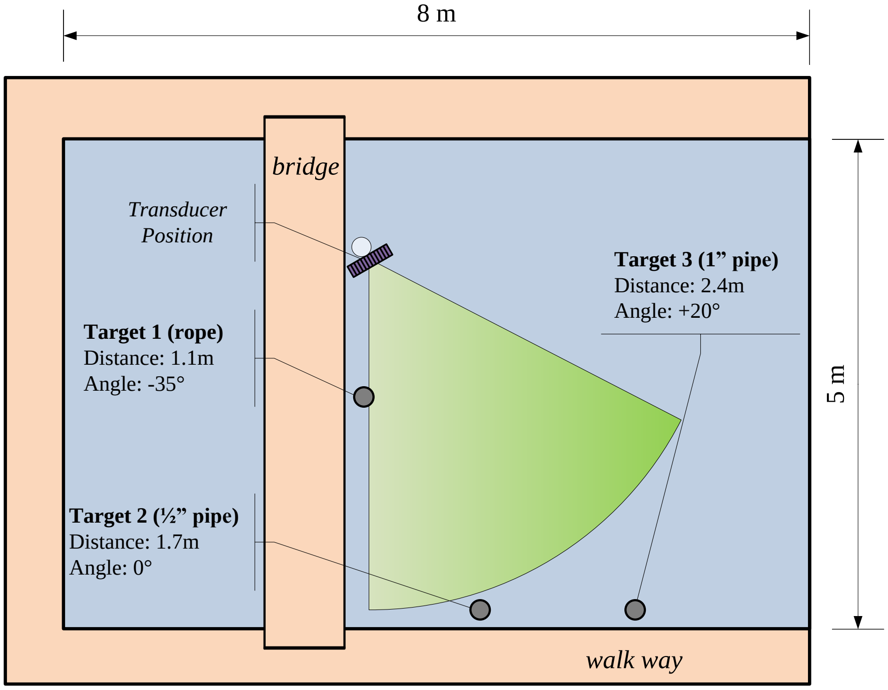

Figure 7.1: Setup for Discrete Target Experiments at the Underwater Research Facility.

7.1 Discrete Target Experiments

The University of Victoria Underwater Research Facility boat house includes a 8 m by 5 m opening through which instruments and targets can be lowered into the water. In this experiment a small 1/2” pipe, a larger 1” pipe and a rope were suspended vertically in the water column at different distances and angles from the transducer. The experimental sonar’s transducer was also mounted vertically in the water column at a depth of 1.4 m below the water line. A detailed view of the experimental setup is shown in Figure 7.1.

The prototype SBS transducer acoustic radiation pattern is a thin fan shaped beam pattern and the vertical orientation of the SBS transducer aligns the major axis of this fan beam parallel with the water surface. The vertically placed pipes intersect this beam and entirely span its vertical extent. The result is a set of small discrete cylindrical targets of the same length but at different distances and angles relative to the SBS transducer. The ranges to the targets are determined by the time of flight, while the angles to the targets are determined interferometric processing alone since it has already been established in Chapter 3 that an improvement in SNR is beneficial regardless of the type of angle estimation procedure used.

The sonar transmitted the following pulses 100 times each and used the resulting backscatter to quantify the improvement in SNR and reduction in angle-of-arrival variance for the coded pulse:

1. Rectangular uncoded pulse 12 and 24 cycles long, and
2. Barker-13 coded pulse with symbol lengths of 12 and 24 cycles.

The received backscatter generated by the transmitted pulses was processed in MATLAB to quantitatively investigate the performance change resulting from the use of pulse compression. The analysis procedure was as follows.

First the backscatter is filtered with a matched filter, then the SNR of the signal is determined, and finally the angle of arrival is solved for by means of interferometry using the centre two elements of the 8-element array.

7.1.1 Illumination of Three Targets with Uncoded Rectangular Pulse

A typical simple sonar system transmits a rectangular or gated pulse at the carrier frequency of the sonar. The received backscatter is also typically filtered to match the bandwidth of the transmitted pulse in order to maximize the received signal SNR. The first experiment conducted in the boat house used an uncoded 24 cycle rectangular transmit pulse. The experiment is a representation of the typical rectangular pulse sonar system.

Figure 7.2 (a) shows the received backscatter for this uncoded 24 cycle long rectangular pulse. In (b) the backscatter has been match filtered; using a simple sinc

(a) Backscatter Return

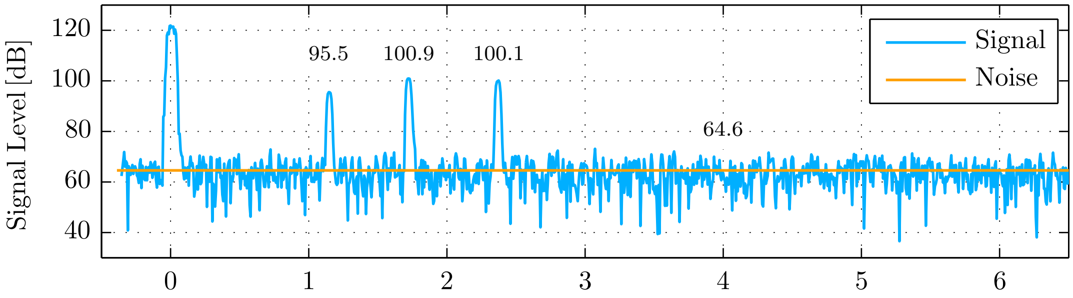

(b) Filtered Backscatter Return

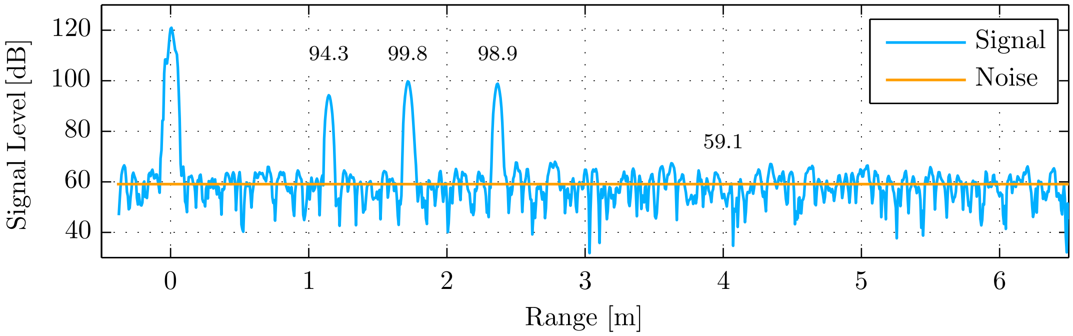

Figure 7.2: Backscatter and processed return from three targets using uncoded 24 cycle rectangular pulse.

frequency response that matches the bandwidth of the gated transmitted pulse. The filter reduces the noise floor by 5.5 dB and slightly attenuates, by 1.2 dB, the target backscatter. The peak signal level for the three targets and the noise floor are highlighted in the figure. From these measurements, the SNR for the peak response of each target is calculated as 35 dB, 41 dB and 40 dB.

7.1.2 Illumination of Three Targets with Barker-13 Coded Pulse

In this experiment the three targets were illuminated using a Barker-13 coded pulse with 24 cycles per symbol. This pulse has the same bandwidth and therefore the same range resolution as the 24 cycle rectangular pulse but is 13 times longer in duration. Figure 7.3 (a) shows the received backscatter generated by this pulse. The

(a) Barker-13 Backscatter Return

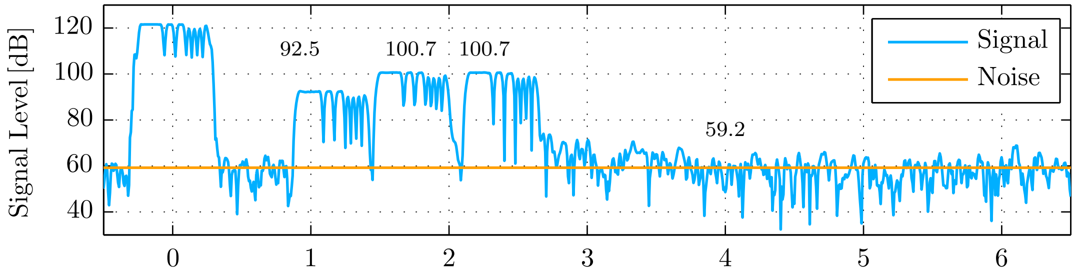

(b) Barker-13 Match Filtered

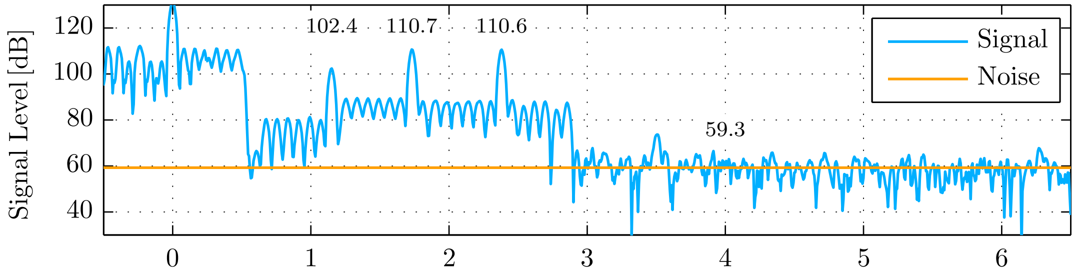

(c) Barker-13 Minimum PSL Mismatch Filtered

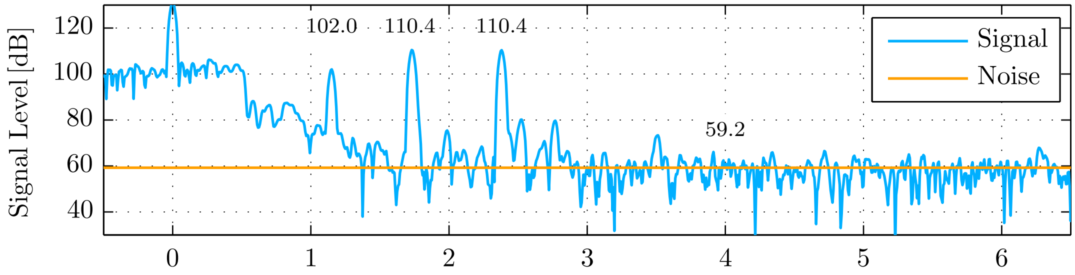

(d) Barker-13 Minimum PSL Mismatch Filtered with Transmit Erased

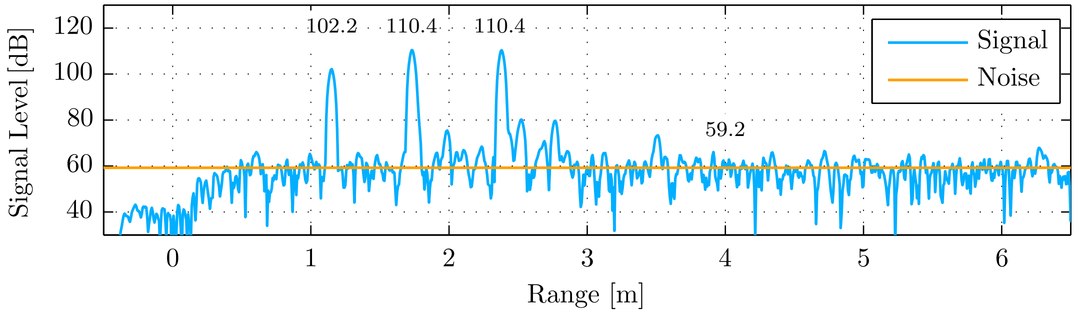

Figure 7.3: Backscatter and processed return from three targets using coded Barker-13 pulse with 24 cycles per symbol.

Barker-13 code sequence can be clearly seen in the return.

After the backscatter is match filtered in (b), the intensity of each target is increased by 9.9 dB, which is called the processing gain, and is very close to the theoretical 11.1 dB gain for a Barker-13 code. Unfortunately the sidelobes inherent to match filter processing of coded pulses are also clearly visible surrounding each target. In order to suppress these sidelobes and at the same time maintain the same amount of processing gain the backscatter can be mismatch filtered using a minimum PSL filter of length 65 as discussed in Chapter 4.

In (c), the sidelobes have been suppressed using the mismatched filter at a small cost in SNR, a loss in processing gain of 0.2 dB. This small loss is corresponds exactly to the expected LPG for a length 65 minimum PSL filter applied to a Barker-13 code, as calculated in Section 4.5.1.

From Figure 7.3 (c) it can also be seen that although the mismatched filter has suppressed the sidelobes for targets 2 and 3 it seems to have actually further obscured target 1, the target closest to the transducer. The reason for this discrepancy is that the transmit signal has erroneously leaked into the receive backscatter and acts to distort the lengthy mismatched filter in the vicinity of the backscatter from target 1.

To address this issue the transmit pulse leakage at the beginning of the ping is removed before the backscatter is filtered.[2] As can then be observed in Figure 7.3 (d), the result is similar to the improved sidelobe suppression results for targets 2 and 3, and at the same time target 1 is now well defined. In summary, the introduction of the Barker-13 coded pulse and pulse compression of the received backscatter using a mismatched filter has resulted in a 10 dB net increase in SNR.

---

[2] The recorded samples out to a range of 0.5 m are set to zero.

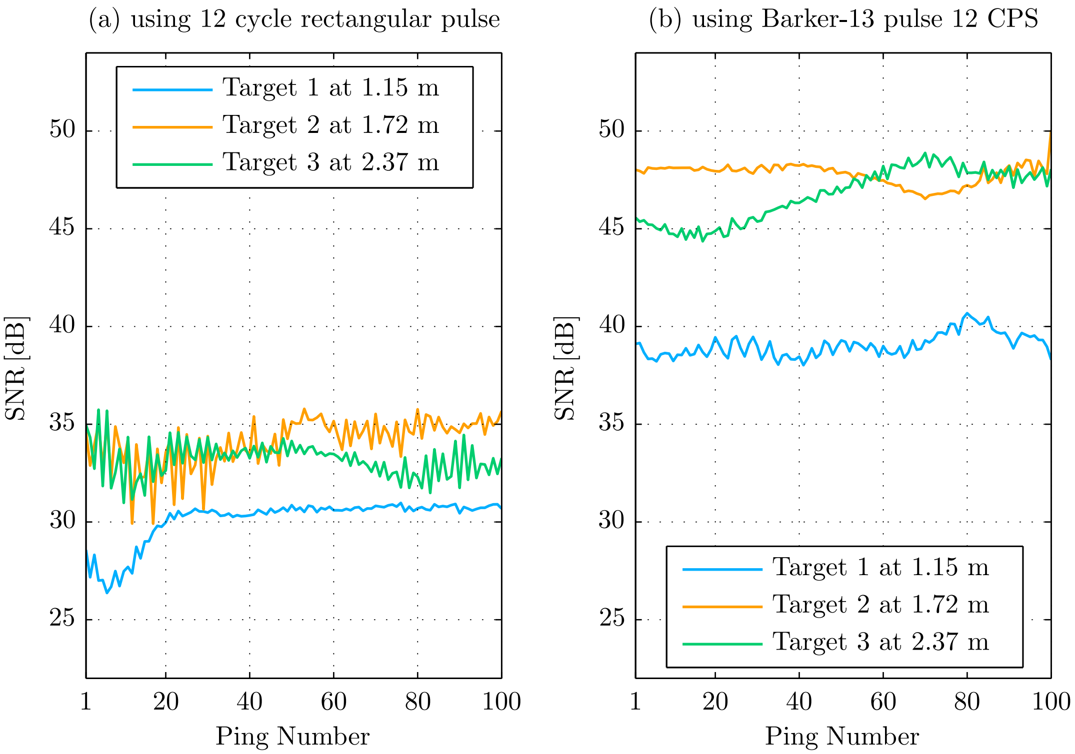

Figure 7.4: SNR for three targets for both uncoded and coded pulses.

7.1.3 Improved Angle of Arrival Estimates.

The improvement in SNR demonstarted in the previous section is expected to yield an improved angle estimate for each target. The objective of this section is to confirm that improvement by measuring the SNR and angle to each target over 200 pings; 100 with pulse compression and 100 without. Although a similar procedure was used in the previous section, the gated pulse length for the uncoded transmit pulses, and the symbol length for the coded pulses is reduced to 12 cycles in these experiments in order to widen the bandwidth.[3] Figure 7.4 (a) shows the SNR of the three targets over 100 pings using the 12 cycle rectangular pulse. The SNR shown in Figure 7.4 (b) is for the other 100 coded pings which use a Barker-13 12 cycle per symbol pulse.

---

[3] The previous section used 24 cycles in-order to better show the Barker-13 sequence in the backscatter return prior to filtering.

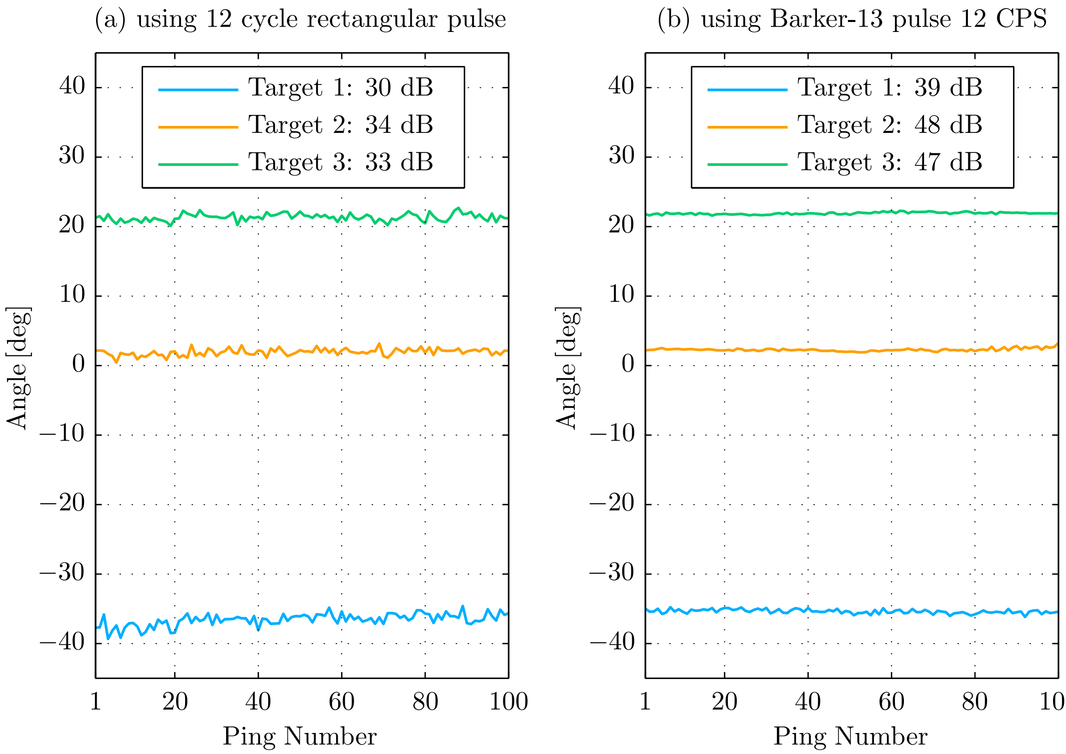

Figure 7.5: Angle to each of the three targets over 100 pulses.

A 9 dB increase in SNR due to pulse compression can be observed for target 1, and an 11 dB to 15 dB increase is observed for targets 2 and 3. The larger than expected increase can in part be attributed to slight motion of the targets and hence the slow variation in SNR seen in Figure 7.4.[4]

For each ping the angle to each target is computed using the 2-element interferometric differential phase method. The results of the interferometric method over the 100 pings are shown in Figure 7.5. In this figure the decrease in variance is clearly evident even before computing it; ping-to-ping the computed angle shows significantly less variance with additional SNR.

Over one hundred pings, the average angle to each target and its standard deviation are computed and listed in Table 7.1 for both the uncoded rectangular pulse and the coded mismatch filtered Barker-13 pulse.

---

[4] Target motion varies the angle of incidence on the targets and this in turn can significantly vary the target strength for returns that are close to specular (e.g. from a smooth cylinder wall).

	SNR	Angle	Angle Std [deg]	
	[dB]	[deg]	expected	actual
Target 1 @ −35° - Interferometric Solver				
Rectangular Uncoded 12 Cycle Pulse	30	-36.6	0.70	0.71[a]
Barker-13 Coded 12 CPS Pulse	39	-35.4	0.25	0.27[a]
Target 2 @ 0° - Interferometric Solver				
Rectangular Uncoded 12 Cycle Pulse	34	1.9	0.36	0.40[b]
Barker-13 Coded 12 CPS Pulse	48	2.3	0.07	0.10[a,c]
Target 3 @ 20° - Interferometric Solver				
Rectangular Uncoded 12 Cycle Pulse	33	21.3	0.44	0.52
Barker-13 Coded 12 CPS Pulse	47	21.9	0.09	0.11[d]

[a] Removed motion using 2nd order polynomial fit.
[b] Evaluated over 50:100 pings.
[c] Evaluated over 1:50 pings.
[d] Removed motion using 3rd order polynomial fit.

Table 7.1: Mean SNR, Angle and Angle Std computed over 100 pings using Interferometric Solver.

The uncoded 12 cycle pulse has a large standard deviation in the angle estimate to each of the three targets of 0.71°, 0.40° and 0.52° respectively. The Barker-13 processing gain of 11 dB has reduced this standard deviation of the angle estimate to 0.27°, 0.11° and 0.10° respectively.

7.2 Continuous Target Experiments

In this set of experiments the 50 m long side wall of the Saanich Commonwealth Place swimming pool was used to simulate the sea bottom. The sonar was mounted vertically in the pool at a position 5.4 m along the short 21 m end wall of the pool. The following coded and uncoded transmit pulses were used to illuminate the simulated bottom:

1. 15 cycle uncoded rectangular pulse.

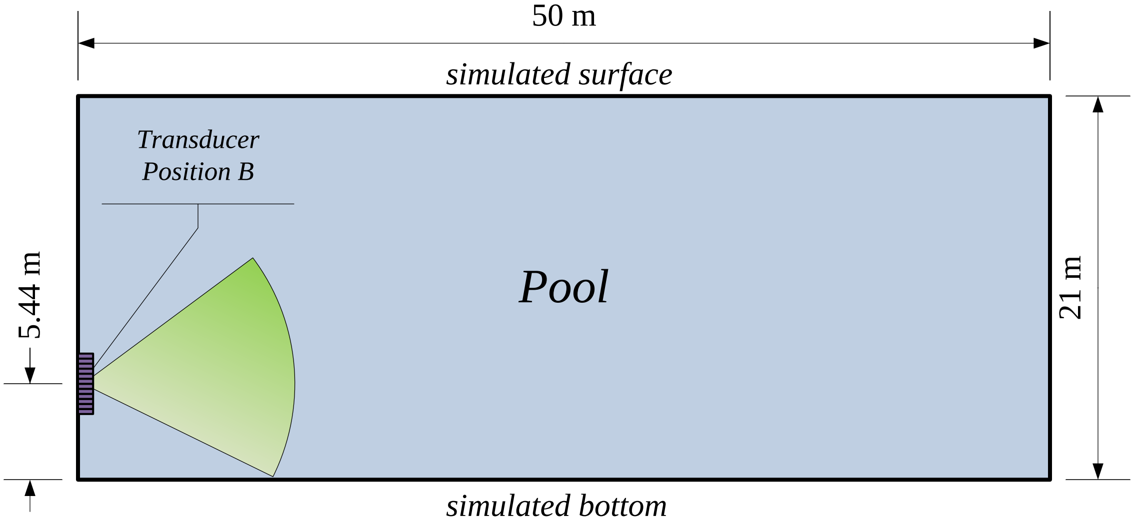

Figure 7.6: Setup for pulse coding experiments at the Commonwealth pool.

2. Coded Barker-13 pulse with 16 cycles of the carrier per symbol (Section 4.5.1).
3. Coded Optimal PSL 43 pulse with 16 cycles per symbol (section 4.5.6).

The received backscatter was pulse compressed to improve the SNR and the profile of the side wall was derived from angles computed using the TLS AOA algorithm. This procedure was repeated 200 times for each of the three pulse types in order to derive the standard deviation of the angle measurements.

7.2.1 Inspection of the Backscatter Intensity.

The thinking behind the experiment was that the pool wall, being a flat plane, would represent a continuous source of backscatter in a fashion similar to that of the sea bottom (e.g. a sandy bottom). However, on inspection of the received backscatter echoes, the returns are in fact better described as a series of intense discrete scatterer returns every 25 cm rather than a single continuous return. The discrete return pattern can be attributed to the flatness of the pool tiles which produce nearly specular acoustic reflections, in combination with the regularly spaced strong scatter returns produced by the grout in between the 25 cm long tiles. Figure 7.8 (a)

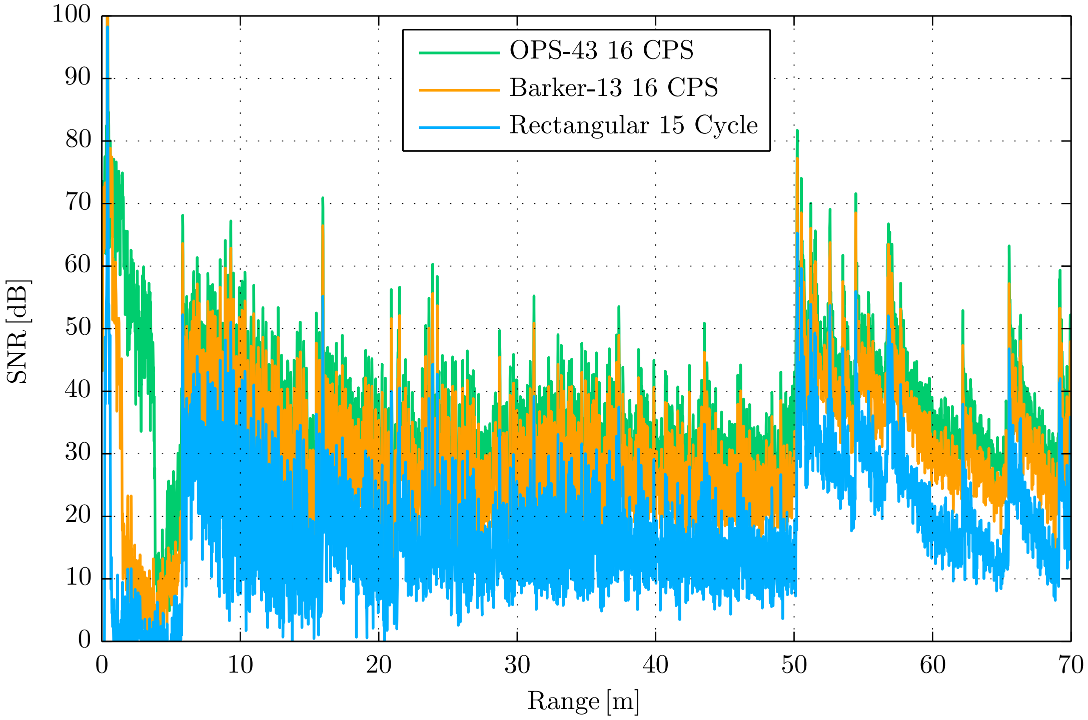

Figure 7.7: Acoustic backscatter return for three different pulses at the Commonwealth pool.

demonstrates these strong “grout” returns which can be seen every 25 cm. The angle to each of the discrete grout scatterers is then estimated as the pulse travels along the wall using the 8-element TLS AOA algorithm.

The entire received backscatter return is pulse compressed and shown in Figure 7.7. The pool side wall return starts at about 5.4 m and remains well above the noise floor until the 50 meter mark. At approximately the 15.4 m mark, the second wall return (i.e. the simulated surface) arrives at the transducer. At the 50 meter mark, the strong reflection of the pulse from the back wall of the pool can also be seen. The compressed Barker-13 and OPS-43 pulses result in a stronger return signal level than the rectangular pulse, and as expected the OPS-43 outperforms the Barker-13 in terms of improved SNR. The increased SNR is expected to reduce angle variance and provide a benefit in bathymetric accuracy. To verify this prediction, a small segment of the pool wall is selected and processed with TLS AOA over 200 pings in order to determine angle variance.[5]

7.2.2 Verification of Angle Variance Reduction with Increased SNR.

Figure 7.8 (a) shows the SNR of the returned backscatter from 9 m to 11 m slant range, or 7.8 m to 10 m cross-track distance. The processing gain achieved over the uncoded pulse, as seen in the figure, is 11.3 dB for the Barker-13 coded pulse, and 16.2 dB for the optimal PSL length 43 code. These values match up well with the expected processing gains predicted by sections 4.5.1 and 4.5.6 respectively.

Figure 7.8 (b) then shows the mean of the computed angle for each of the 3 pulses. This mean angle is different where the variance is high for the three pulse types, and overlaps where the variance is low for the three pulse types. All three pulse types exhibit a null in their response at the 10 m mark, possibly due to an obstruction, and this null produces widely varying angle estimates in this region.

Finally, Figure 7.8 (c) shows the standard deviation of the computed angle for the 3 pulses over the 200 pings. A decrease in standard deviation is observed for the coded pulses, with the optimal PSL-43 code outperforming the Barker-13 as expected.

Unfortunately the high variability in the intensity of the backscatter, caused by specular reflections from the pool tiles, prevent the experiment from generating a smooth angle progression as the pulse travels along the pool wall. In spite of this problem, the experiments validate the prediction that pulse compression will produce an increase in SNR, which in turn will reduce the variance of individual angles computed by TLS AOA processing.

---

[5] The use of the TLS AOA algorithm was chosen over the interferometric method because of its flexibility in the number of angle solution sought. It happened that this flexibility was not used until Chapter 8.

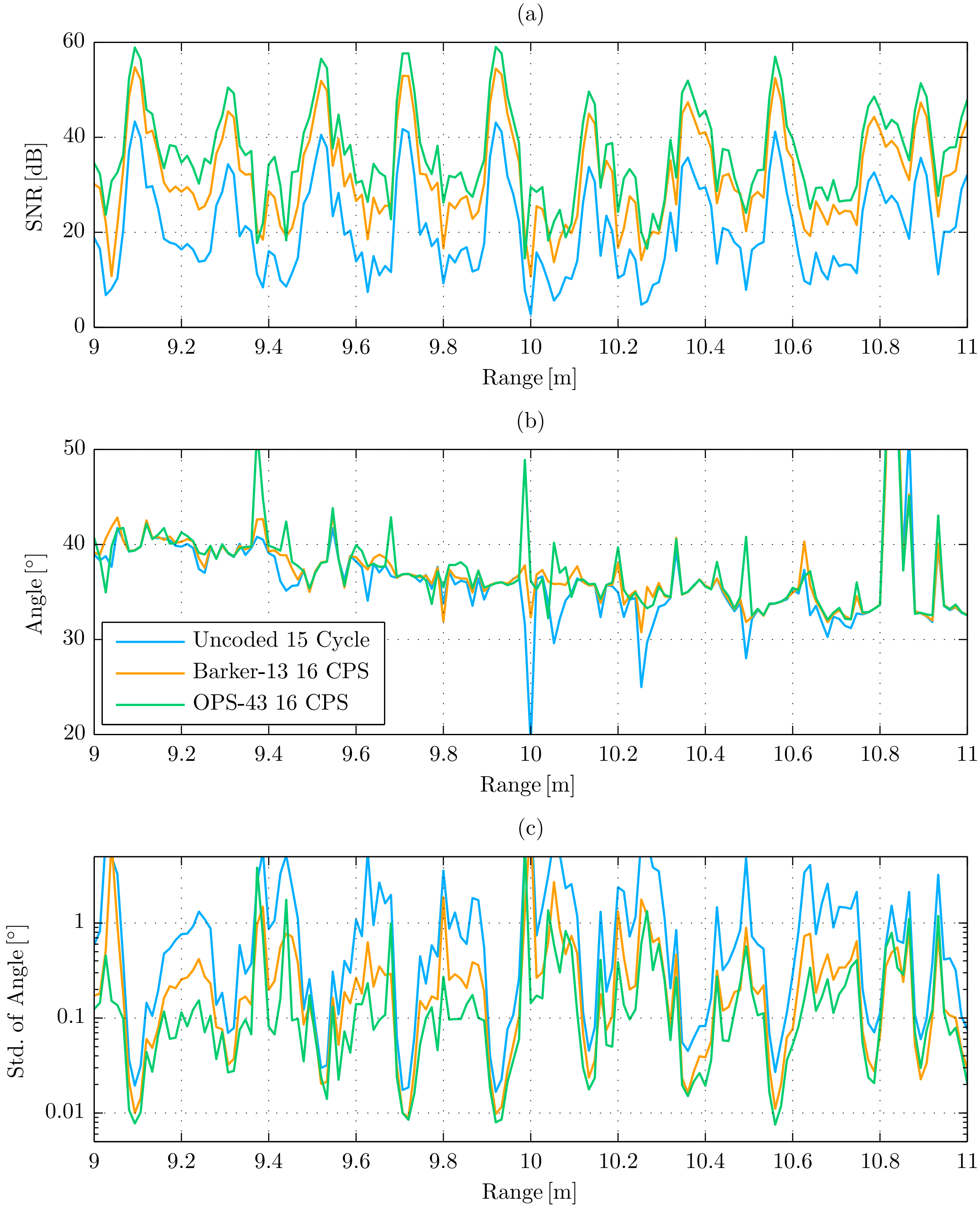

Figure 7.8: Angle variance of pool wall backscatter between 9 m and 11 m range.

7.2.3 Polar and Cartesian Plots of Commonwealth Pool Return

The backscatter captured in the previous section was processed for 3 angles of arrival using TLS AOA and plotted in Figure 7.9. The range, angle and intensity of each scatterer is plotted and shows returns from both the near and far pool walls. The intensity of the return for the 3 different pulses has been normalized before plotting. Hence the plots in Figure 7.9 (a-c) have roughly the same intensity. In all three plots (a-c), only one arrival occurs before the 15 m mark, and this arrival originates from the near side wall. At the 15 m mark, the far side wall return arrives, and at the 30 m to 35 m mark multipath arrivals start to occur. A close look at the return in the vicinity of the 35 m mark shows two direct paths, the sea surface and sea bottom, and at least two multipaths. This number of arrivals exceeds the number of solutions in the TLS AOA formulation. Thus the angle solutions break up beyond the range of 40 m due to the ever increasing grazing angle and the excessive multipaths. Although difficult to observe, the coded pulses do in fact have a lower angle variance as was shown in the previous section.

The polar plot in Figure 7.9 was also converted to Cartesian coordinates and plotted in Figure 7.10 to show the actual image of the pool side wall representing the sea bottom. The pool side wall is well defined and can be seen all the way out to 37 m. This result shows the impressive ability of the TLS AOA algorithm to image the sea bottom to nearly 7 times the altitude of the sonar (i.e 5.4 m here) in a strong multipath environment.

The next chapter presents the results of experiments using transmit shaping and steering to increase backscatter intensity in a direction of interest (e.g towards the sea bottom and away from the surface) and in turn also reduce the intensity of interfering multipaths.

(a) 15 cycle rectangular pulse

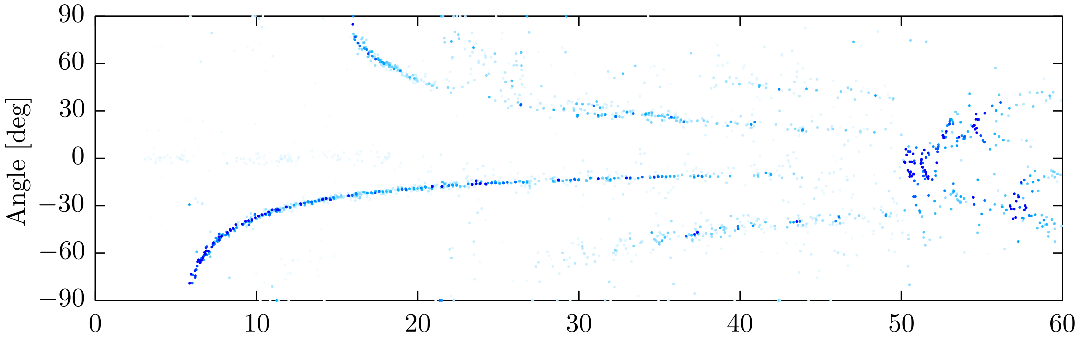

(b) Barker-13 16 CPS pulse

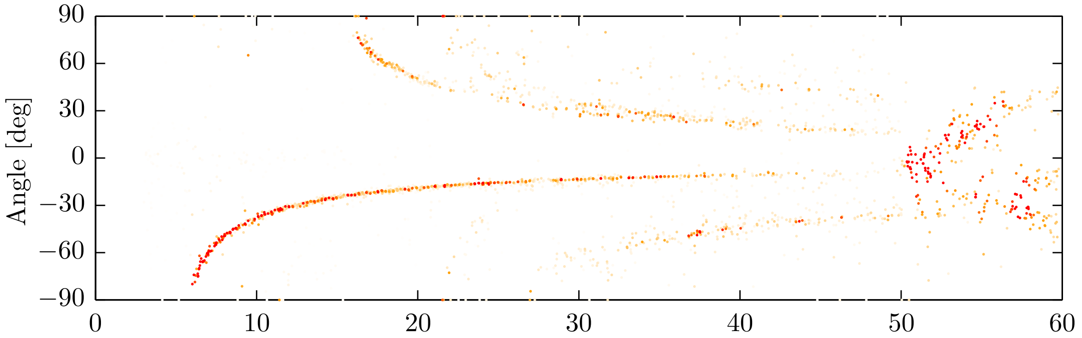

(c) optimal PSL-43 16 CPS pulse

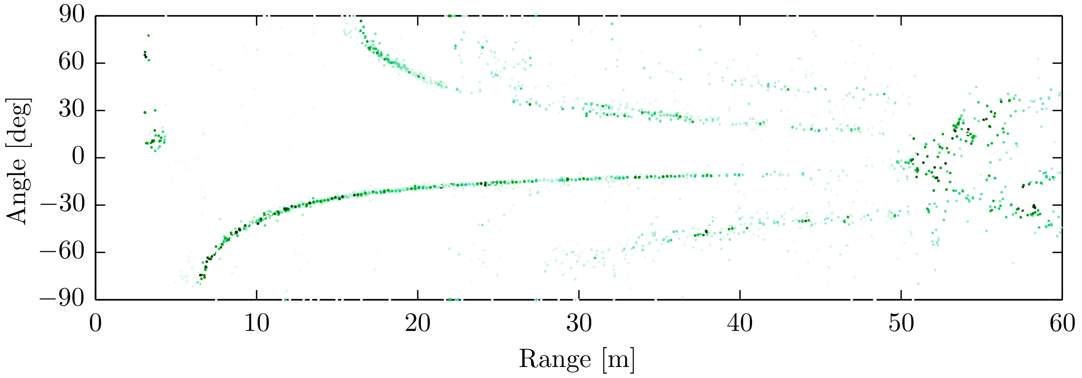

Figure 7.9: Scatter plot of angle solutions versus range for three different coded pulses.

(a) 15 cycle rectangular pulse

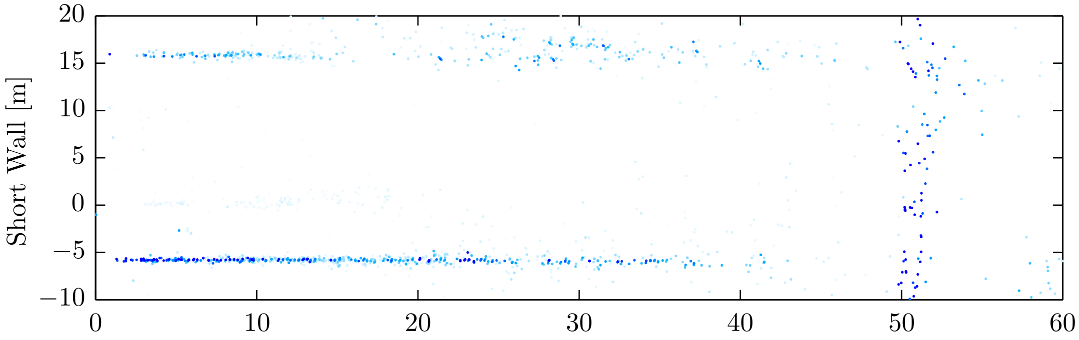

(b) Barker-13 16 CPS pulse

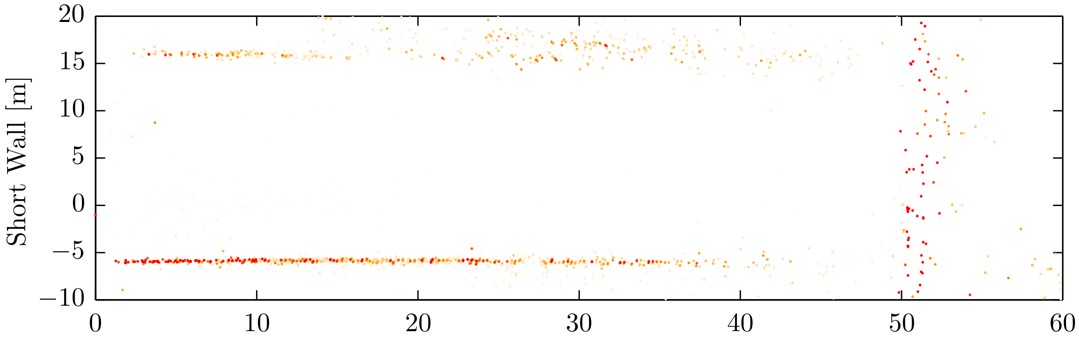

(c) optimal PSL-43 16 CPS pulse

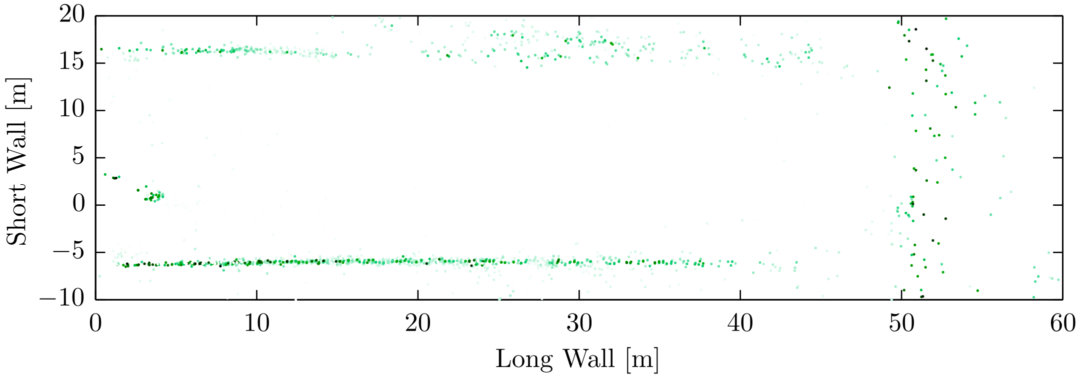

Figure 7.10: Scatter plot of angle solutions for three different coded pulses in Cartesian coordinates.

Chapter 8

Experimental Investigation of the Benefits of Transmit Beamforming

The objective of this chapter is to experimentally validate the benefits of transmit steering in SBS applications as described in Chapter 5. Specifically, the increased illumination afforded by transmit shading and steering of the full 8-element SBS array is demonstrated to increase the SNR of a simulated sea floor return and provide lower angle variance leading to superior bathymetry.

The three scenarios described in Chapter 5 are replicated in a set of experiments conducted at the Saanich Commonwealth Place pool. First, the intensity of the return generated by the 8-element shaded and steered beam-pattern is compared to that of typical 2-element sidescan illumination. Second, the variance in the return angle is computed for the 2-element and 8-element beam-patterns over 100 pings from a stationary sonar.

Finally, conclusions are drawn from these experimental results and possible future modifications to the experiments are suggested which will help clarify the results.

Beam Pattern	Element Weights, a_i							
	1	2	3	4	5	6	7	8
2-element, 55°	-	-	-	1.00	1.00	-	-	-
8-element, 20°	0.04	0.22	0.62	1.00	1.00	0.62	0.22	0.04

Table 8.1: Array shading coefficients used in the experiments.

8.1 Experimental Investigation of Flat Bottom Illumination

The dimensions of the pool found at Commonwealth Place make it ideally suited for the verification of the scenarios described in Chapter 5. The width and length of the pool are approximately 21 m and 50 m respectively, and almost the entire pool is over 2 m deep.

The experimental EX450 sonar is placed vertically in the water and its fan beam response is oriented to be parallel with the pool surface. The narrow beam of the EX450 transducer, $\sim 0.6°$, ensures that neither the main lobe nor the close in sidelobes strike the surface or floor of the pool. Depending on the placement of the transducer along the short wall of the pool, either of the two long walls can be illuminated for imaging, as seen in Figure 8.1. The two long walls of the pool are used to simulate the sea surface and sea bottom in the conducted experiments.

8.1.1 Scenario A

From Chapter 5, scenario A represents an AUV application where the sidescan sonar is near to the sea bottom, and far from the sea surface. To emulate this the transducer is placed 5.4 m away from the near wall, and the main response of the transmit beam-pattern is electronically steered 20° down towards the near wall, as seen in Figure 8.1 (a). The performance of two beam-patterns of interest, 2-element and 8-element

(a) Scenario A: near to bottom

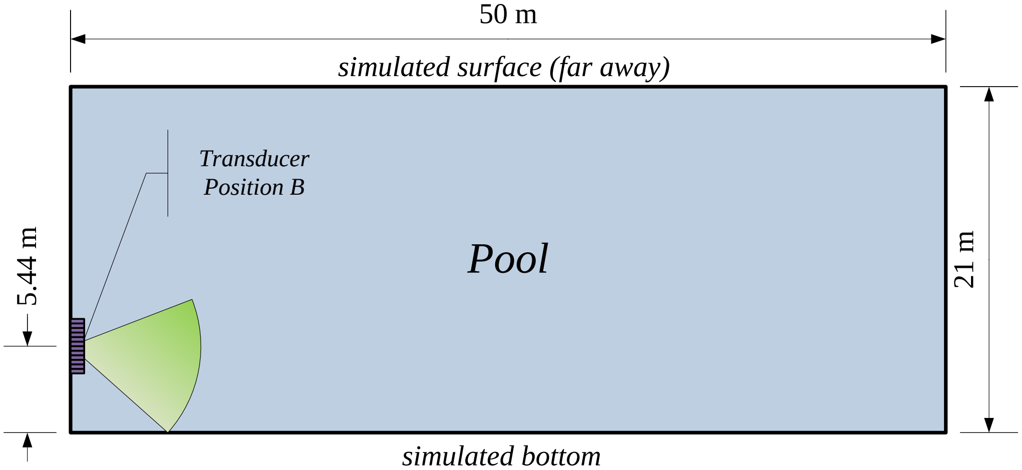

(b) Scenario B: near to surface

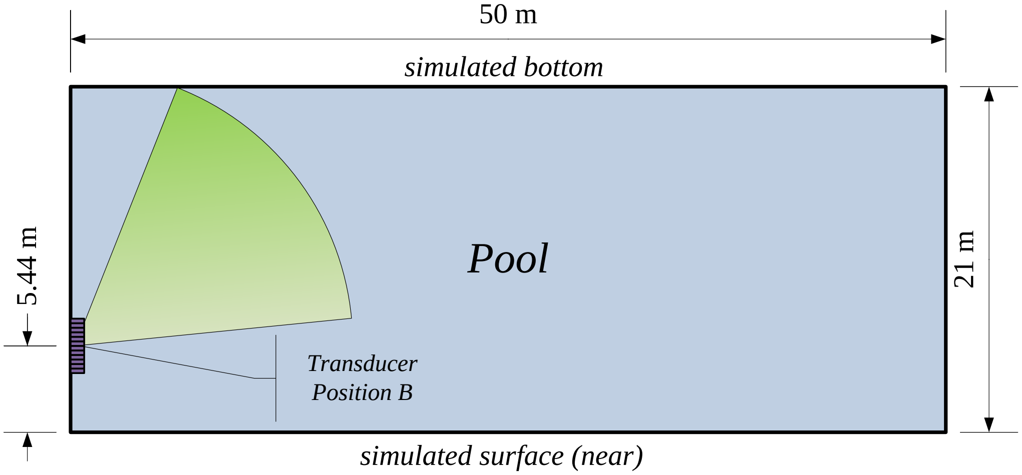

(c) Scenario C: mid water column

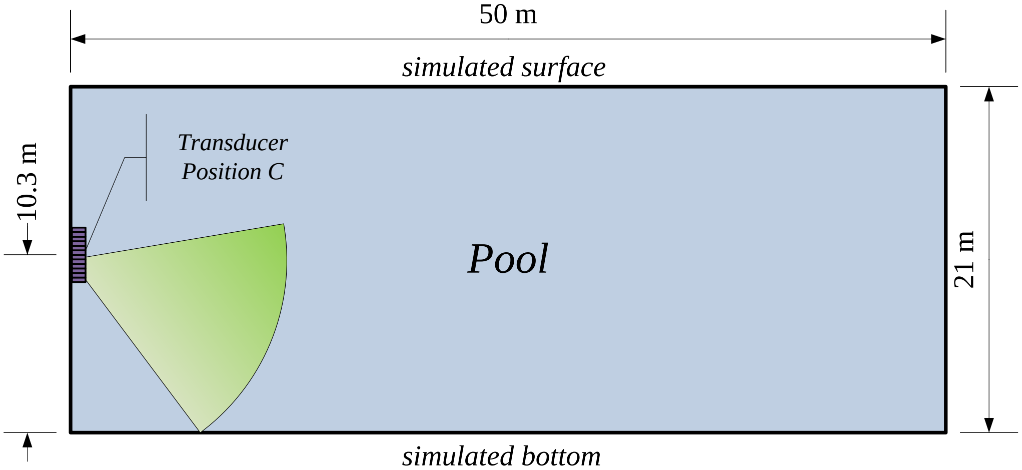

Figure 8.1: Setup for SBS scenario experiments in the Saanich Commonwealth pool.

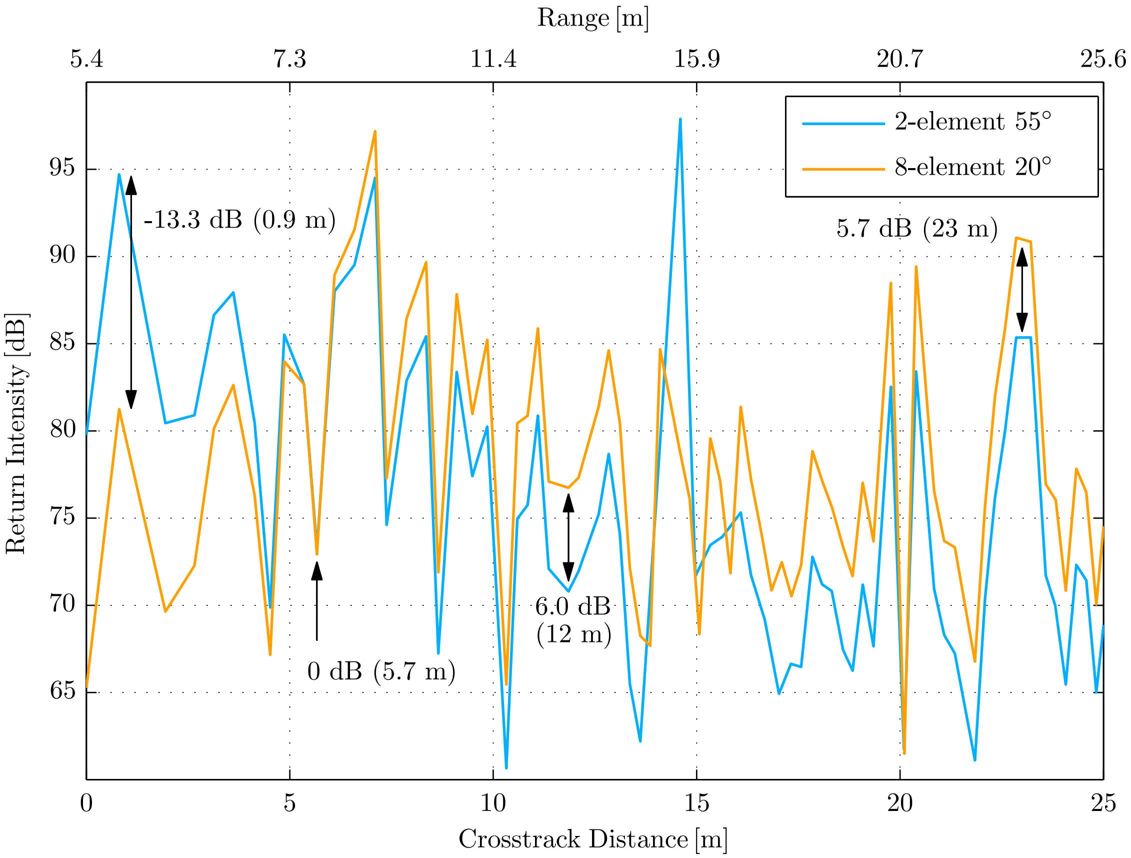

Figure 8.2: Scenario A return intensity for the 2-element and 8-element transmit patterns.

patterns, with coefficients given in Table 8.1 are investigated.

From the simulations performed in Chapter 5 and specifically Figure 5.4 the following results are expected:

1. An increase in the received signal level of 5 dB in the case of the 8-element pattern over the 2-element pattern at crosstrack distances beyond 7.5 m.
2. A crossover in the received signal level of the two patterns at a crosstrack distance of 5.2 m.
3. A significant decrease and drop-off in the received signal level for the 8-element pattern at crosstrack distances prior to 4 m.

In short, the 8-element beam-pattern is expected to trade near nadir illumination for stronger illumination further away in crosstrack distance, and therefore a stronger backscatter response.

From Figure 8.2, the results of the scenario A experiment conducted in the pool, the following observations can be made[1]:

1. An increase in the receive signal level of 4.2 dB to 6.0 dB for crosstrack distances beyond 8 m. Specifically, at 12 m the 8-element pattern produces a 6.0 dB increase in signal level. This increase slightly reduces to 5.7 dB at 23 m.
2. The intensity crossover for the two patterns occurs at 5.7 m.
3. The 2-element pattern is 13.3 dB stronger at the close-in crosstrack distance of 0.9 m. Note that this reduced 8-element signal level is stronger than the 2-element pattern return beyond 17 m, most of the time.

The experimental results are consistent with the simulation conducted in Chapter 5. backscatter intensity has increased for distances beyond 8 m, and this is expected to yield lower angle variance. The angle variance for this scenario is investigated in Section 8.2.1.

8.1.2 Scenario B

Scenario B represents a situation where the sidescan is mounted over-the-side and is operating in shallow water. To emulate this operating configuration, the sonar is placed 5.4 m from the near wall which simulates the sea surface. The transmit beam is steered 20° towards the far wall which simulates the sea bottom and is 15 m away. This setup is shown in Figure 8.1 (b).

The backscatter signal level for both the sea bottom and sea surface is extracted from the SBS array through the use of a Hanning weighted *Fast Fourier Transform*

---

[1] The number of points in Figure 8.2 has been reduced using a peak picking algorithm to make the figure easier to read.

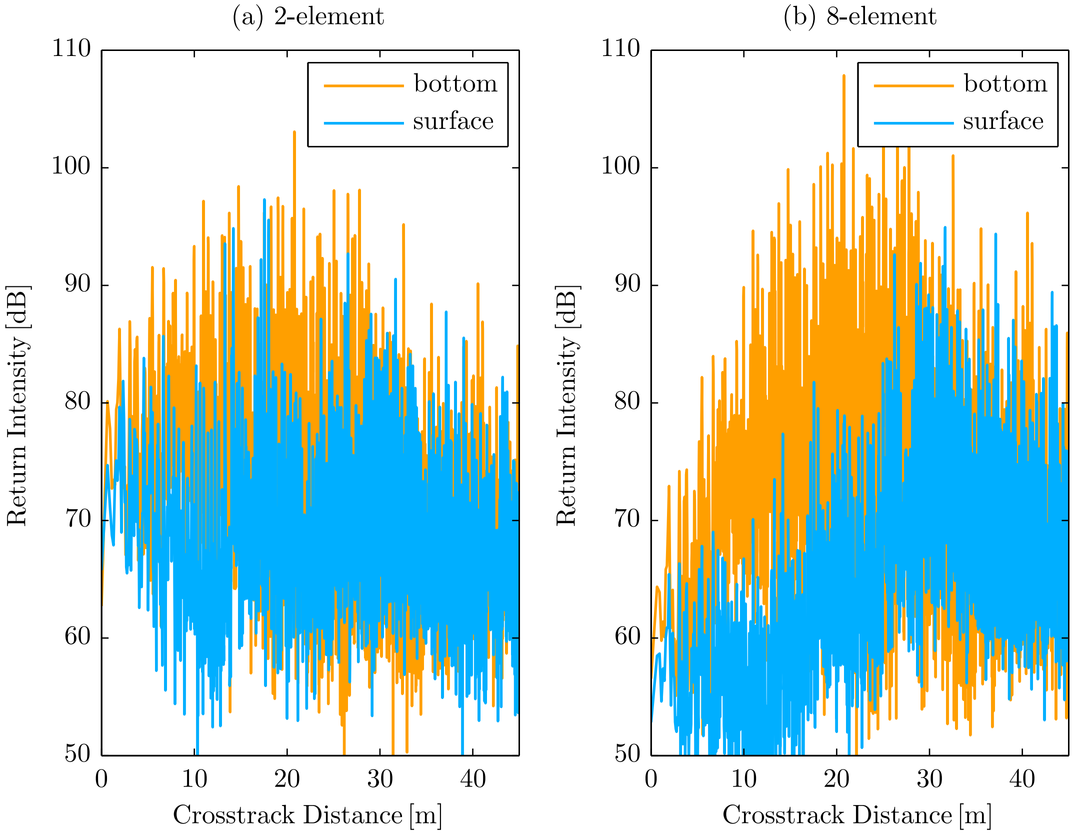

Figure 8.3: Scenario B bottom and surface return intensities for 2-element and 8-element transmit pattern illumination.

(FFT) to form eight beams.[2] The end-fire and broadside beams are discarded, because the energy within them cannot be attributed to arriving from either the bottom or the surface. The remaining six beams are split into two sets, one set of beams points upwards while the other points downwards. These beams are then incoherently summed to produce an overall upward and an overall downward backscatter intensity measurement. These two measurements represent the amount of backscatter energy arriving from the bottom and the surface.

The simulations conducted in Chapter 5 predict that the 8-element pattern will illuminate the sea bottom more intensely than will the 2-element pattern, while at the

---

[2] The FFT of the response seen on an SBS array is equivalent to beam forming or spacial filtering in 8 distinct directions. Specifically, $-49°$, $-30°$, $-14°$, $0°$, $14°$, $30°$, $49°$ and $\pm 90°$ for the 8-element SBS array.

Crosstrack Distance	Simulated Return Separation [dB]		Experimental Return Separation [dB]	
	2-element	8-element	2-element	8-element
5 m	10	6	7.4	10.8
10 m	13	17	11.7	20.9
15 m	14	26	7.6	18.6
20 m	15	30	3.2	7.4
30 m	15	31	-4.0	-2.1

Table 8.2: Scenario B simulated and experimental return separation for the 2-element and 8-element transmit patterns.

same time leaking less energy into the sea surface. Indeed this result can be observed in Figure 8.3, where the bottom return backscatter of the 8-element pattern is more intense than the 2-element one. At the same time, the surface backscatter produced by the 8-element pattern is significantly weaker than the 2-element one for crosstrack distances of less than 25 m. Figure 8.3 shows the general trends well, however due to the high variability of the return it is difficult to quantify the improvement. A quantification is attempted in Figure 8.4, where five slices of the return are selected for closer inspection. Table 8.2 then summarizes the results along with the expected performance from the Chapter 5 simulations.

The experimental return separation is comparable to the simulated results for crosstrack distances less than 15 m to 20 m. The 8-element transmit beam-pattern has successfully increased the separation in the return intensity at crosstrack distances less than 15 m. Specifically, the backscatter intensity of the sea bottom return is now 20 dB stronger than the sea surface. It had been only 10 dB stronger using the 2-element transmit beam-pattern.

Beyond a crosstrack distance of 20 m, or equivalently 25 m range, the experiment falters due to the onset of multipath arrivals that corrupt the calculated bottom and surface return intensities.

Prior to the arrival of these multipaths the increase in intensity separation is

(a) illumination with 2-element transmit pattern

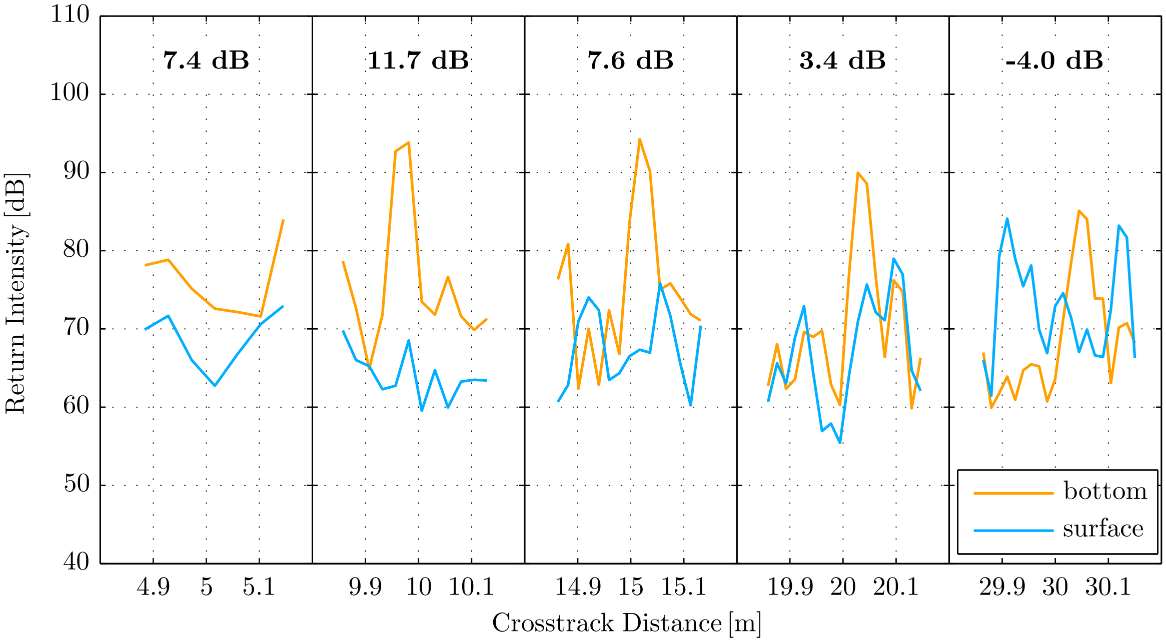

(b) illumination with 8-element transmit pattern

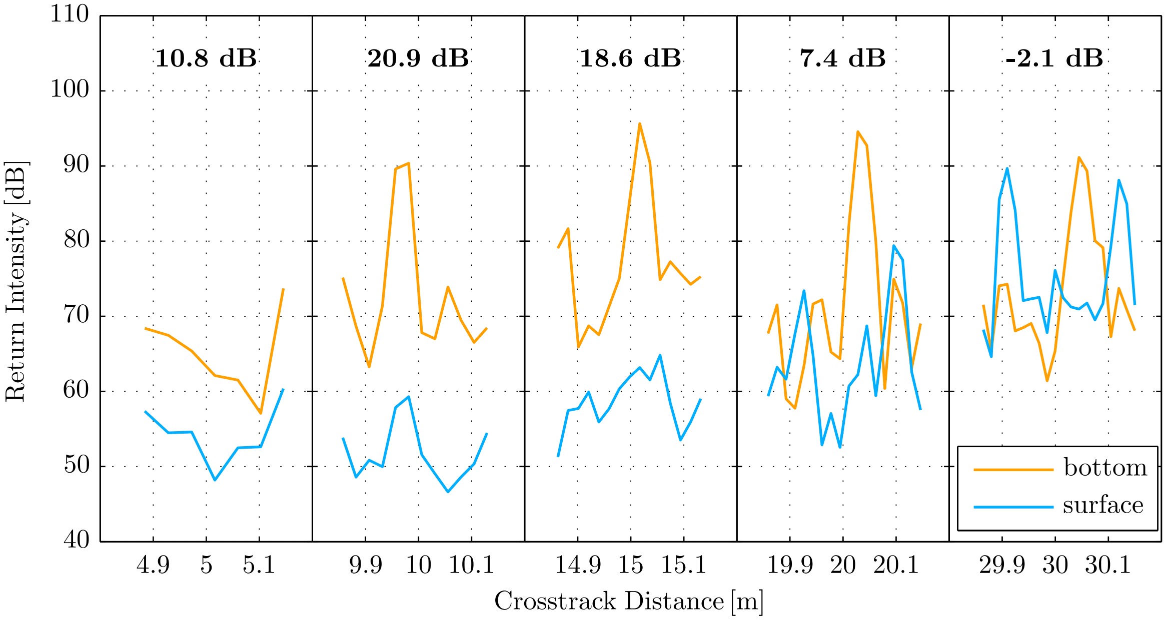

Figure 8.4: Scenario B close up inspection of experimental return intensity for 2-element and 8-element transmit patterns.

expected to yield superior SBS performance, and this prediction is investigated in Section 8.2.2.

8.1.3 Scenario C

Scenario C attempts to simulate a shallow water, mid-water-column scenario where either an AUV or tow-fish sidescan is in the centre of the water column. In the pool experiment the transducer is placed 10.3 m away from near wall, which is almost in the middle of the simulated water column. The setup is illustrated in Figure 8.1 (c). This near wall simulated the sea bottom, while the opposite wall simulates the sea surface and is 10.7 m away. The 2-element and 8-element beam-patterns are steered 20° towards the simulated bottom, in order to more intensely illuminate it than the simulated surface. The surface is considered an undesired interferer, and its suppression is the objective in this scenario.

The intensity of the simulated surface and bottom backscatter is extracted from the experimental data using the same method as in the previous section. A similar plot to those in the previous sections is shown in Figure 8.5, where the backscatter intensities for the two beam-patterns are compared. In this figure, the increased backscatter intensity of the bottom when illuminated by the 8-element beam-pattern is clearly observable, as is the reduced intensity of the surface.

The beamforming result is limited in that surface-bottom and bottom-surface multipaths can occur at ranges greater than 20 m,[3] and cannot be separated from the surface and bottom backscatter with the method used here. In this scenario, these multipaths arrive at the transducer after a crosstrack distance of 20 m, and the intensity separation of the bottom backscatter versus the surface can no longer be observed.

---

[3] These multipaths are visible in Figure 7.9 of the previous chapter. At a range of 21 m arrivals are seen from 80° and −80°.

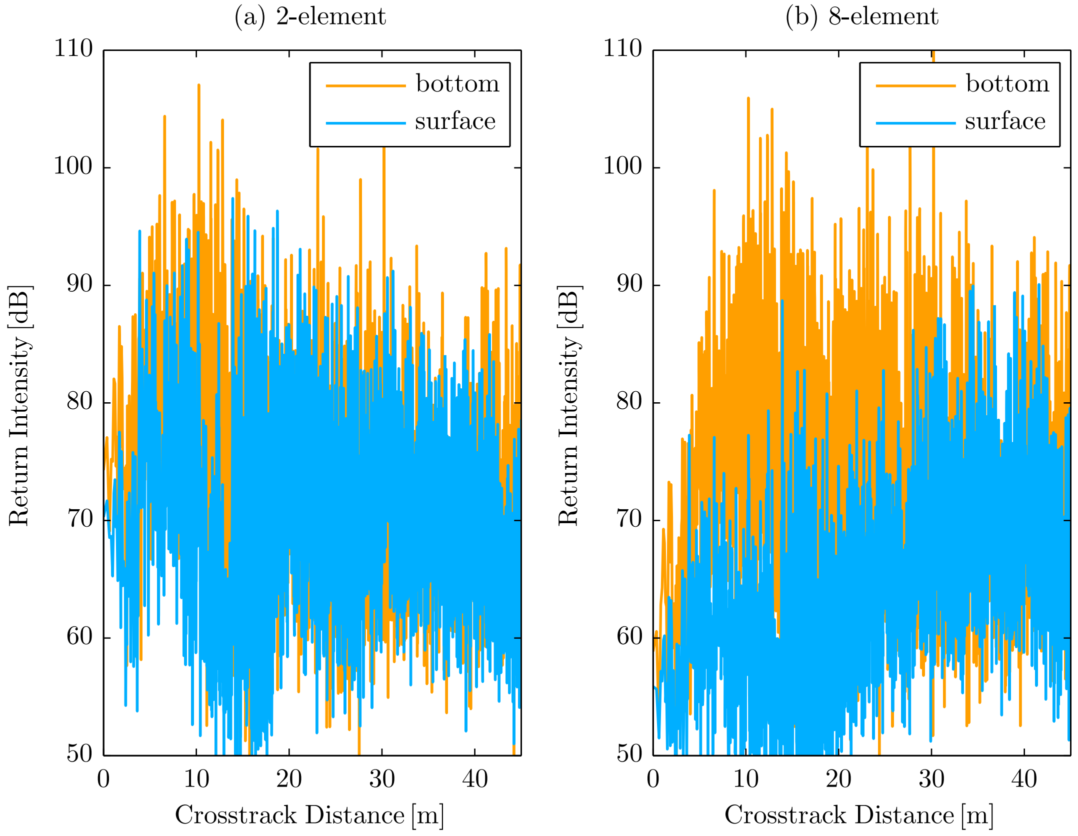

Figure 8.5: Scenario C bottom and surface return intensities for 2-element and 8-element transmit pattern illumination.

The simulations in Chapter 5 predict a very large 30 dB separation throughout the entire return, however in the experiments this large separation is only observed before 15 m crosstrack distance. This does not necessarily mean that the separation is absent beyond 15 m, it simply cannot the observed due to excessive multipaths.[4]

Figure 8.6 shows expanded views of the return intensity plot at five crosstrack distances. From this figure the 8-element illumination beam-pattern can be seen to on average increase the separation of the bottom and surface backscatter by 10 dB. This result is significantly smaller than the Chapter 5 predicted increase in separation of 19 dB to 25 dB at crosstrack distances beyond 15 m.

---

[4] The width of the FFT beams also plays a role in the effectiveness of separating the bottom, surface, and any multipath return intensities. The SBS array has only 8 elements, and their Hanning weighted FFT beamformed width is greater than 18°, and becomes worse away from broadside.

(a) illumination with 2-element transmit pattern

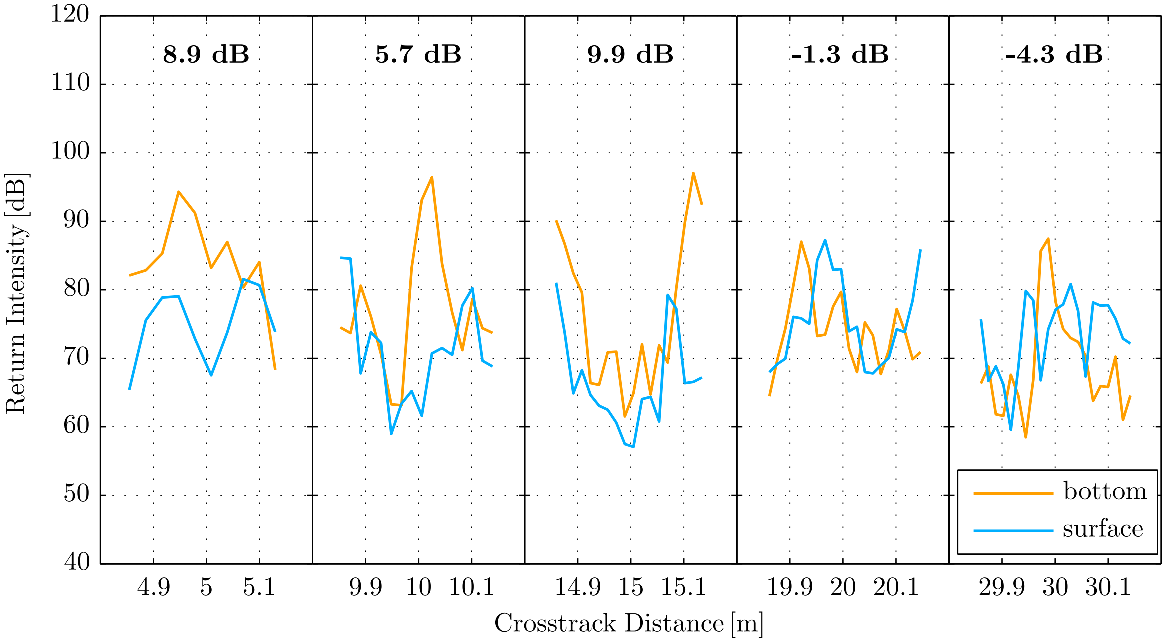

(b) illumination with 8-element transmit pattern

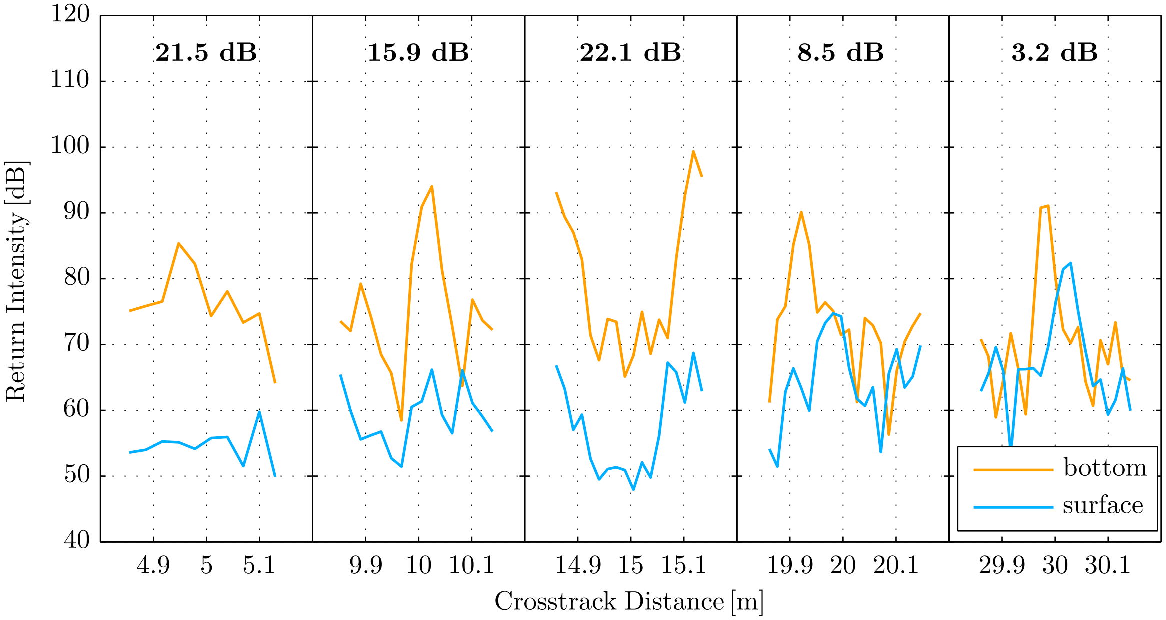

Figure 8.6: Scenario C close up inspection of experimental return intensity for 2-element and 8-element transmit patterns.

Although the measured backscatter intensity separation did not match the simulated values of Chapter 5, the 8-element pattern did generated a superior bottom-surface intensity separation when compared to that achieved with the 2-element pattern. Given this increased separation, it is expected that SBS performance will improve when using the narrower 8-element transmit illumination beam-pattern.

8.2 Experimental Investigation of Angle Variance

The first half of this chapter looked strictly at the backscatter intensity generated by the 2-element and 8-element transmit patterns. The remaining half of this chapter concentrates on whether this increase in backscatter intensity and intensity separation translates into a decrease in angle variance. This decrease is the desired objective and the justification for adding transmit shading and steering capabilities into SBS sonars.

8.2.1 Scenario A

Section 8.1.1 outlined and experimentally quantified the increase in backscatter intensity afforded by the 8-element transmit beam-pattern. The use of all 8 elements of the SBS array on transmit generated more acoustic energy and directed it at the simulated sea bottom. This increase is expected to reduce the variance in angle estimates, and it is important to verify that this indeed does occur. With that goal in mind, the sonar was kept stationary and 100 pings were transmitted with each of the transmit patterns. For each ping the TLS AOA algorithm was applied to solve for one arrival at each point in time. Over the entire span of 100 pings, the mean and standard deviation of the computed angle at each time step were also computed.

The results of this experiment are shown in Figure 8.7, from which it can be generally concluded that higher intensity returns produce angle estimates with a

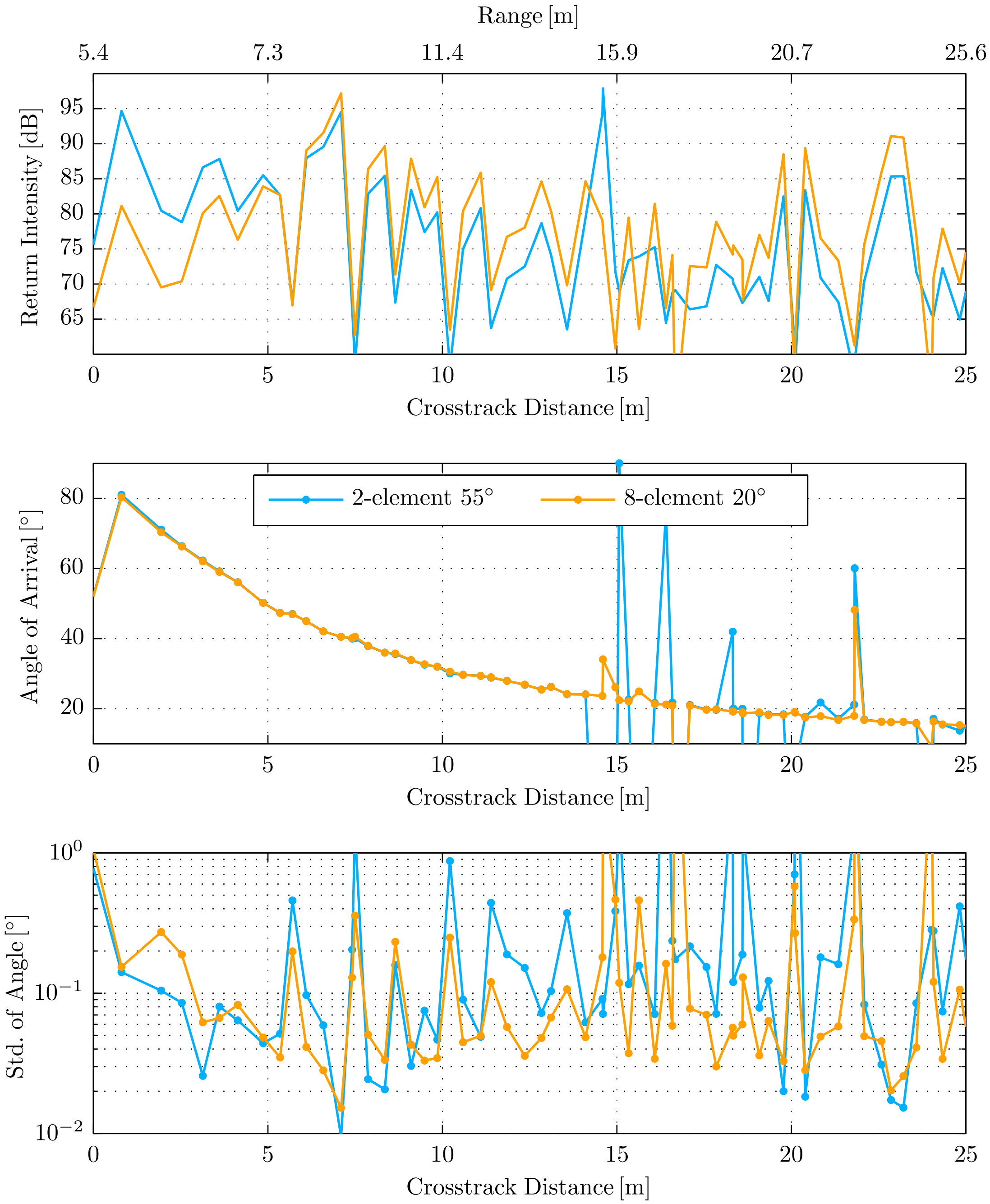

Figure 8.7: Scenario A standard deviation of one solution TLS AOA for 2-element and 8-element transmit illumination.

lower standard deviation. A few key points are summarized below:

1. For cross-track distances between 0 m and 5 m the 2-element pattern generates a higher intensity return which leads to lower standard deviation.
2. For cross-track distances beyond 6 m, the intensity crossover point, the 8-element pattern for the most part generates a higher intensity return which also leads to lower standard deviation.
3. At the cross-track distance of 15 m, the very wide response of the 2-element pattern illuminates the far wall and causes two arrivals. At this point seeking only one solution when multiple arrivals are present significantly degrades performance.
4. The 8-element pattern avoids illuminating the far wall and the single solution $M = 1$ TLS AOA algorithm continues to function well beyond the 15 m mark.

Based on these four points, it can be concluded that the 8-element pattern is better suited to this scenario. The 2-element pattern performs well but only prior to the arrival of a second arrival from the far wall 15 m away. Given two arrivals of similar magnitude, as observed here, the TLS AOA method seeking only one solution and general interferometry are expected to breakdown.

Fortunately for the TLS AOA algorithm the number of angle solutions sought at any one instance in time is a parameter M and can be increased, unlike interferometry. The same data is reprocessed seeking two angle solutions, and the results are shown in Figure 8.8. With $M = 2$, specifying two solutions, the TLS AOA algorithm significantly helps the 2-element pattern overcome the undesired surface arrival at 15 m. Even with this help, the 8-element pattern continues to outperform the 2-element pattern.

As an aside, for crosstrack distances lower than 15 m a comparison of the angle variance seen in Figure 8.7 to that of Figure 8.8 shows that, when only one arrival is

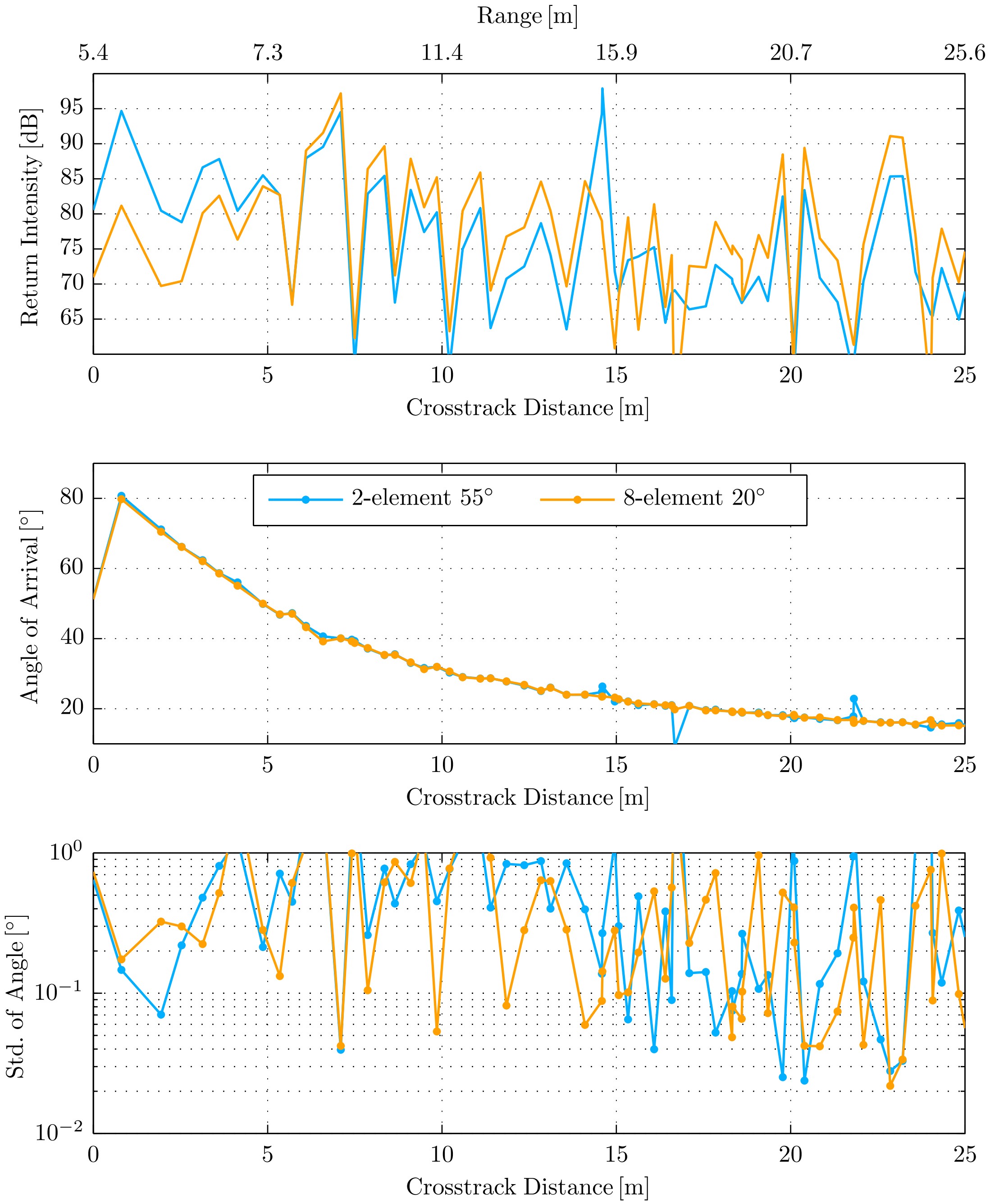

Figure 8.8: Scenario A standard deviation of two solution TLS AOA for 2-element and 8-element transmit illumination.

present, solving for one arrival produces better results than erroneously solving for two arrivals.

This scenario has verified that using all 8 elements on transmit is beneficial for SBS performance. The far wall arrival at 15 m was outside the parameters of this scenario as laid out in Section 5.4.1, however unavoidable due to the geometry of the pool. The far wall is a part of scenario B discussed in the next section, where the near wall return must be suppressed while the far wall is strongly illuminated with the objective of decreasing its angle variance.

8.2.2 Scenario B

Scenario B is different from scenario A in that both the simulated sea bottom and surface are illuminated at all times. Section 8.1.2 showed that the 8-element transmit pattern increases the amount of energy backscattered by the simulated bottom, and at the same time decreases the amount of energy backscattered by the simulated surface. This effectively increases the intensity separation between the two returns and allows the bottom return to dominate.

Once more, 100 stationary pings are performed for each of the two beampatterns, and the variance in the angles is computed and used to compare the performance of the two beampatterns.

In the experiment, the weights of the 8-element beampattern were generated for maximal performance by maximizing the amount of acoustic energy generated and transmitted into the water. The result of this optimization is that the overall backscatter intensity of the sea bottom is increased, typically a desired effect, however it makes attributing increased performance due to return intensity separation difficult. A suggestion is made later in this chapter to improve this experiment by changing the 8-element weights to have equivalent power to the 2-element weights. For now the examination of the available experimental data continues below.

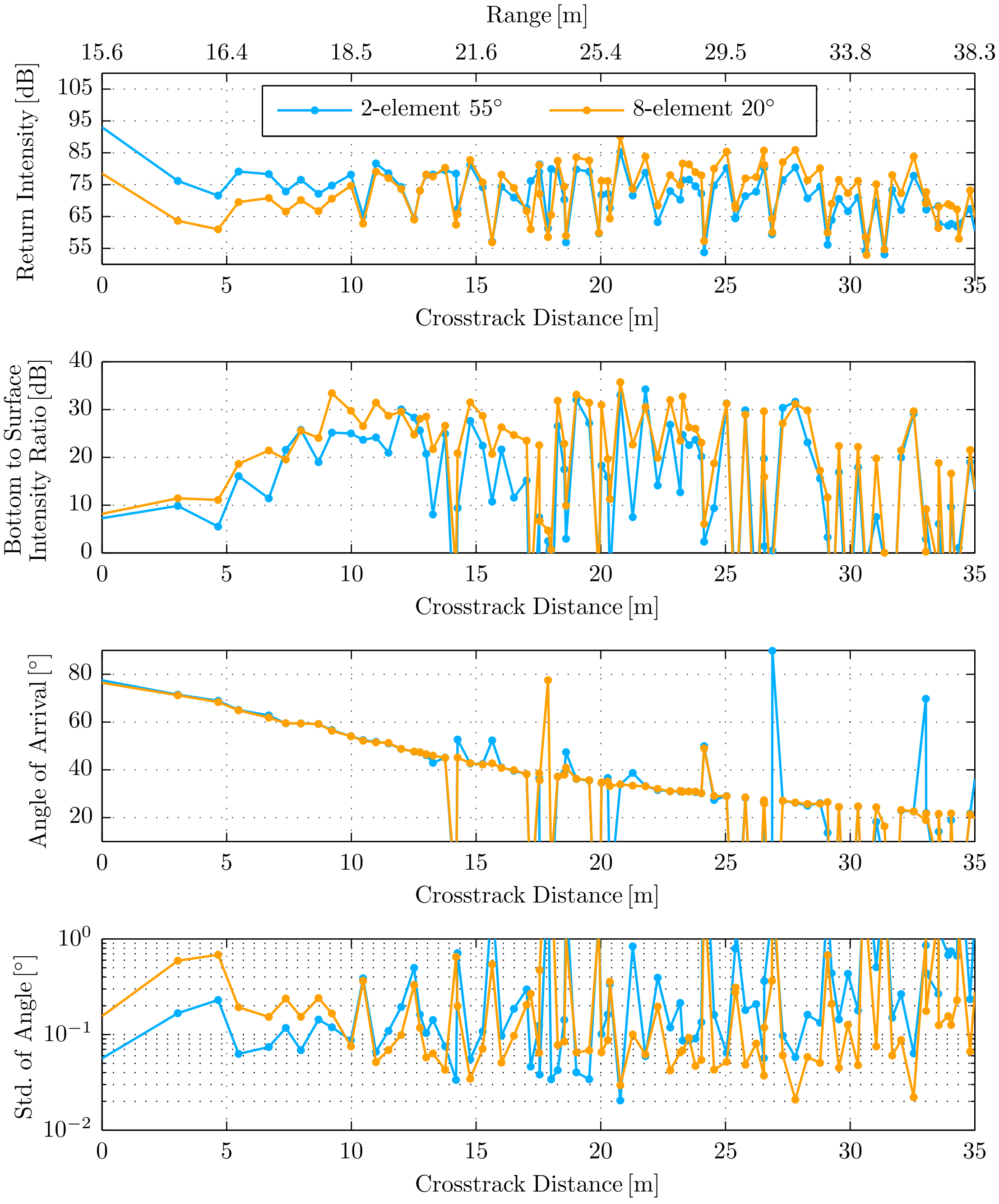

Figure 8.9: One solution TLS AOA results for scenario B using 2-element and 8-element transmit illumination.

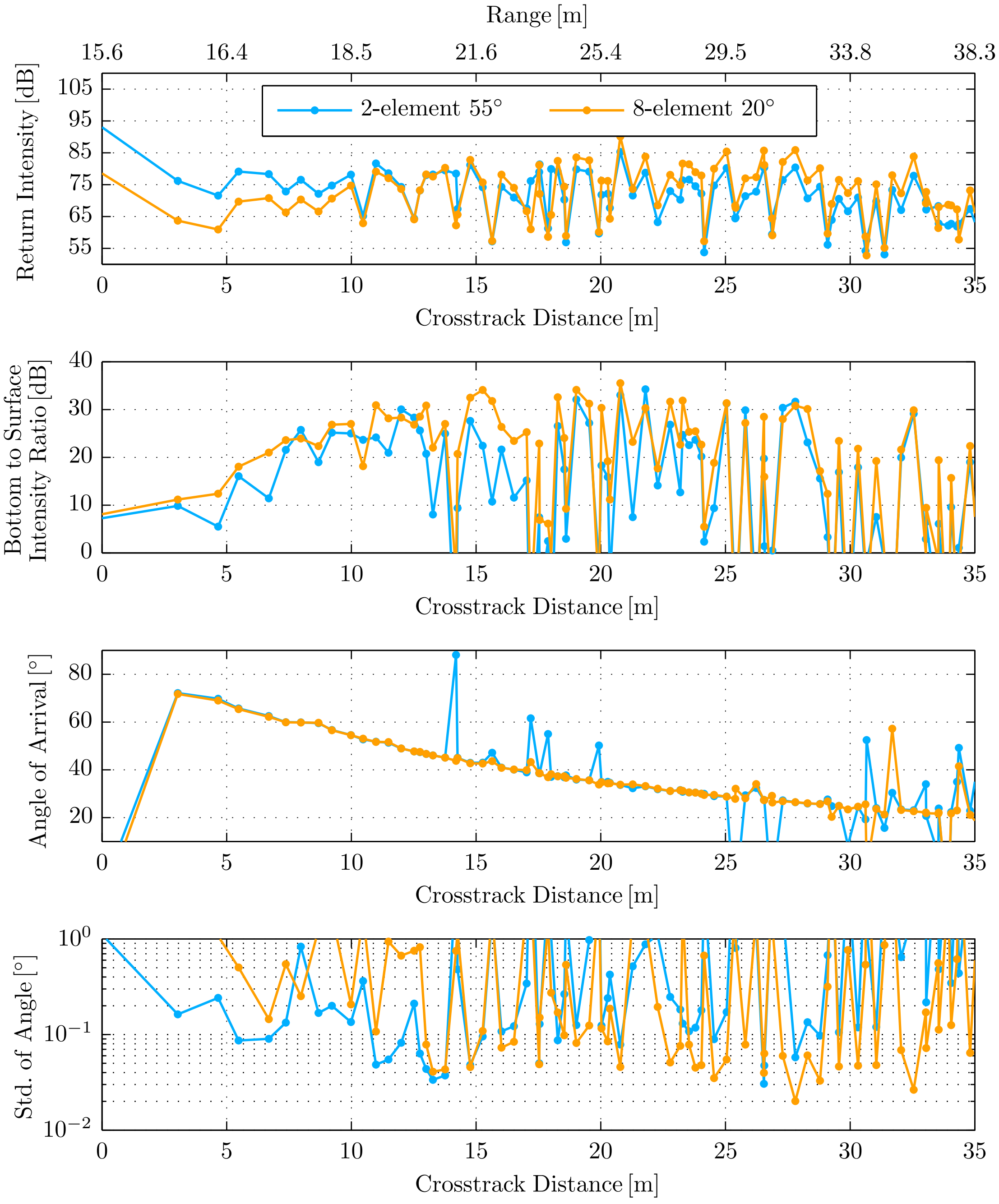

Figure 8.10: Two solution TLS AOA results for scenario B using 2-element and 8-element transmit illumination.

Through an examination of Figure 8.9 the following points, both in support of and in opposition to intensity separation as a means of improving SBS performance, are made:

1. The 8-element pattern performs better beyond 12 m in that it generates a smoother angle response in the presence of multipaths when the TLS AOA algorithm is seeking only one solution, $M = 1$. This observation suggests the 8-element pattern attenuates the intensity of multipath interference, which can be considered a form of intensity separation.
2. At the 10 m mark the angle variance is the same for both patterns; the 2-element pattern has higher return intensity, while the 8-element pattern has higher return separation.
3. At the 13 m mark the return intensity is the same for both patterns, however the 8-element pattern has much higher return separation and a lower angle variance.
4. Beyond 22 m the 8-element pattern exhibits consistent lower angle variance likely owing to its higher backscatter intensity.
5. Between 0 m and 10 m the 2-element pattern has a higher return intensity, while the 8-element pattern has a higher return separation. The 2-element pattern outperforms the 8-element pattern in terms of exhibiting lower angle variance.

When a two solution TLS AOA method is used with both the 2-element and 8-element illumination beampattern the results are similar in that the 8-element pattern produces a smoother angle response, as seen in Figure 8.10. Several spots where multipath interference produced a strong outlying angle solution have disappeared.

The conclusion from this experiment is that intensity separation appears to help, however its effectiveness is difficult to quantify because it overlaps with increased return intensity. In future experiments if the 8-element weights were adjusted such that $\sum a_i^2 = 2$, the amount of acoustic energy generated by the 8-element beampattern would be equivalent to the 2-element pattern.[5] A comparison of the intensity separation with these equivalent energy weights would be more easily conducted.

8.2.3 Scenario C

The situation presented by scenario C is very similar to that of scenario B. The simulations in Chapter 5 predicted less return separation in scenario C, and possibly some visible nulls in the surface return caused by the 8-element beampattern. The experimental data shows high variability in the return separation, which is likely caused by the pool wall grouts being better scatterers than the pool wall tiles. Because of this variability in the scatterer strength quite often either a surface wall or a bottom wall grout backscatter dominates the return. With this in mind Figure 8.11 becomes easier to navigate.

The most interesting section of this figure is the 15 m to 20 m cross-track distance where the return intensity of the two patterns is similar and alternating. In this region, the standard deviation of the angle solutions also alternates, however the 8-element pattern has fewer large outliers as seen in the angle of arrival plot of Figure 8.11. Just as in scenario B, the 8-element pattern produces smoother angles and reduced angle variance in the far crosstrack region, at the expense of increased variance at near crosstrack distances of 0 m to 12 m.

---

[5] For the two beampatterns to have equivalent power the sum of the squares of their coefficients, found in Table 8.1, must be equal. For the 2-element beampattern $\mathbf{a} = [1, 1]$ hence the condition $\sum a_i^2 = 2$.

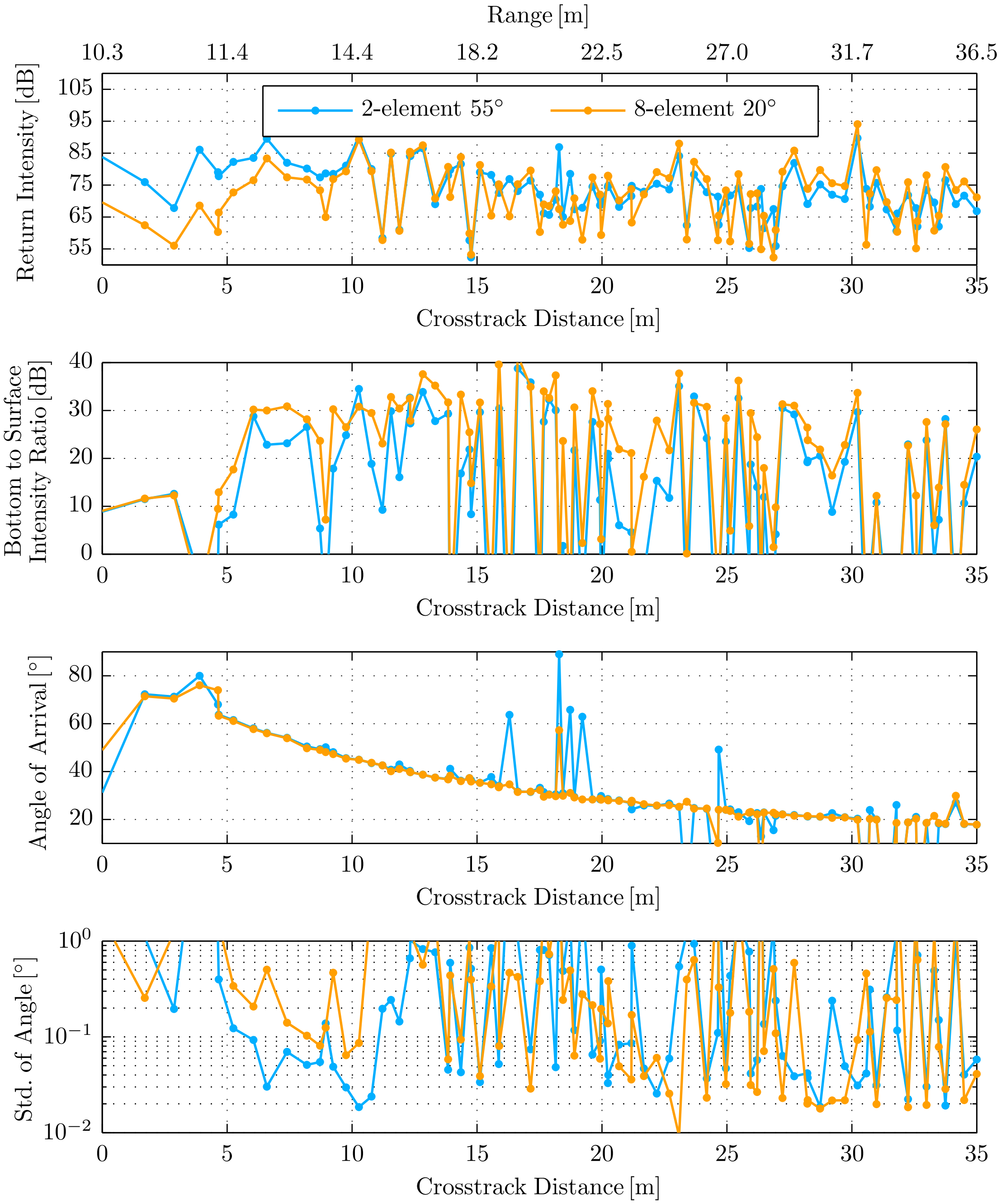

Figure 8.11: Two solution TLS AOA results for scenario C using 2-element and 8-element transmit illumination.

8.3 Conclusion

The combination of increased power and directivity afforded by the use of more elements to illuminate the sea bottom conclusively reduces angle variance and improves SBS bathymetry. In all the experiments conducted here the 8-element pattern outperformed the 2-element pattern, with the expected exception of regions close to nadir where energy has been traded for longer range performance. It is more difficult to quantify the benefits of increasing bottom-surface separation afforded by the 8-element pattern, although it does appear to reduce the number of outlying angle solutions in scenarios where multiple multipaths are present, in excess of the number of angle of arrival solutions being sought.

The high variability in return intensity due to the much higher target strength of the pool grout versus the pool tile makes the analysis in this chapter more difficult. Specifically, at any point in time the grout return of one wall may dominate the tile return of the other wall regardless which was illuminated more intensely. It has been observed in these experiments that the pool grout has a target strength 20 dB to 25 dB stronger than the pool tile.

To solve this the recommendation is to conduct future experiments at a facility with a homogeneous wall, such as a poured concrete barrier. Alternatively, a bring your own wall approach could be used where a long bubble wrap or plexiglass wall is placed in the pool in-front of the actual pool wall. It remains to be determined if the target strength of such a wall would be more consistent, and the wall could be mounted to be sufficiently stationary.

SBS systems inherently feature multiple elements, which are used to solve for multiple angles of arrival on the receive side, therefore there is a substantial opportunity to use all these elements on transmit and improve SBS performance by increasing power and directivity. There is no doubt that the 8-element transmit beampattern provides superior performance.

Chapter 9

Conclusions

Swath bathymetry sidescan (SBS) and the angle-of-arrival processing typical of these systems has the capability to produce much higher resolution three dimensional imagery and bathymetry than traditional beamformed approaches. However, the performance of these high resolution sysems is limited by *signal-to-noise ratio* (SNR) and they are also susceptible to multipaths. This thesis explored two methods for increasing SNR and mitigating multipath interference for SBS systems.

Using simulations it was first established that an increase in SNR is beneficial to SBS angle-of-arrival processing. The SNR increase was accomplished through binary coded pulse transmission and pulse compression. Several different codes were evaluated and match filtering was used to maximize the resulting SNR. Mismatched filtering was also introduced and shown to reduce sidelobes at the cost of a slight reduction in SNR.

Following the simulations, real world SBS experiments were devised and conducted and it was shown that in practice pulse compression increased the SNR almost exactly as predicted through simulations. It was also shown, via simulation and experiments that this increase in SNR did in fact reduce the variance of the resulting angle-of-arrival solutions.

The combination of transmit steering and beam shaping afforded by the 8-element linear angle-of-arrival array was shown to increase both power in the water and the directivity of the transmit acoustic radiation. Transmit energy was redistributed to produce higher backscatter intensity at crosstrack distances by sacrificing energy in the near nadir region in order to reduce the variance in the angle of the return over the majority of the swath and also extend the maximum operating range. Beam shaping also reduced the intensity of interfering multipaths and in some cases mitigated them entirely. In high multipath environments angle-of-arrival can be overwhelmed when the number of simultaneous arrivals, caused by direct paths or multipaths, exceeds the number of solutions the processing is capable of providing. Shaping of the transmit beam was shown to extend the useful range of SBS systems in high multipath environments through the suppression of interfering multipaths.

The improvement in achievable SNR and the reduction in multipath interference provided by the contributions in this thesis further strengthen the increasing impact that SBS systems and angle-of-arrival based processing, as an alternative to beamforming, are having in underwater three dimensional imaging and mapping. A beautiful example of what is now possible with SBS systems is shown on the next page. The image is a 3D point cloud image of the HMCS Mackenzie generated by the 3DSS-EX450 using the methods described in this thesis. The impressive spatial resolution of the Mackenzie image cannot be achieved using existing beamforming sonar systems.

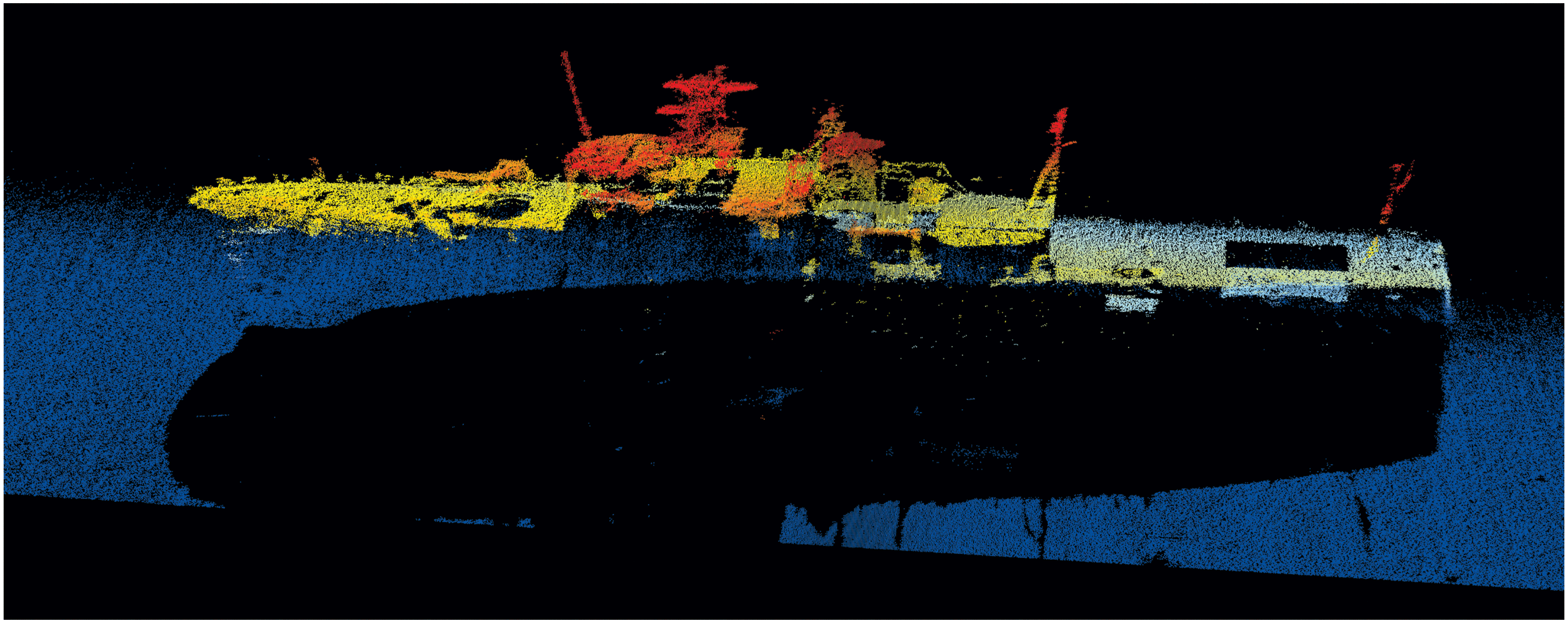

Figure 9.1: HMCS Mackenzie an artificial reef near Sidney, BC imaged with the prototype sonar.

References

[1] National Physical Laboratory, UK, “Underwater acoustics technical guides: Speed of sound in pure water,” 2000.

[2] “Oceanus,” The Illustrated Magazine of Marine Science, vol. 20, Spring 1977. Cover.

[3] A. Hilar, Sonar: Detector of Submerged Submarines. Office of the Chief of Naval Operations, 1946.

[4] G. L. Frost, “Inventing schemes and strategies: The making and selling of the fessenden oscillator,” Technology and Culture, vol. 42, no. 3, pp. 462–488, 2001.

[5] P. Wille, Sound images of the ocean in research and monitoring. Berlin New York: Springer, 2005.

[6] A. D’Amico and R. Pittenger, “A brief history of active sonar.,” Aquatic Mammals, vol. 35, no. 4, 2009.

[7] M. A. Ainslie, Principles of Sonar Performance Modelling. Springer, 2010.

[8] D. Zimmerman, “Paul langevin and the discovery of active sonar or asdic,” Northern Mariner, vol. 12, no. 1, pp. 39–52, 2002.

[9] F. Duck, “Icebergs and submarines: The genesis of ultrasonic detection,” SCOPE Institute of Physics and Engineering in Medicine, pp. 46–50, Sep 2008.

[10] W. Chesterman, P. Clynick, and A. Stride, “An acoustic aid to sea bed survey,” Acustica, vol. 8, pp. 285–290, 1958.

[11] A. Stride, “A linear pattern on the sea floor and its interpretation,” Journal of the Marine Biological Association of the United Kingdom, vol. 38, no. 02, pp. 313–319, 1959.

[12] “Side-scan sonar systems product survey.” Accessed: 2014-02-18.

[13] J. Hersey, H. Edgerton, S. Raymond, and G. Hayward, “Sonar uses in oceanography,” in Instrument Society of America Conference, 1960.

[14] MIT Museum, Massachusetts Institute of Technology, “Klein side scan sonar: A world leader in ocean exploration,” 2008.

[15] P. Denbigh, “Phase only side-scan sonar for underwater mapping,” Acoustic letters, vol. 1, pp. 84–87, 1977.

[16] P. Denbigh, “A bathymetric side-scan sonar,” in Proceedings of the Ultrasonics International 79 Conference, pp. 321–326, May 1979.

[17] P. Denbigh, “Swath bathymetry: principles of operation and an analysis of errors,” IEEE Journal of Oceanic Engineering, vol. 14, pp. 289–298, Oct 1989.

[18] P. Denbigh, “Stereoscopic visualization and contour mapping of the sea bed using a bathymetric sidescan sonar (bass),” Radio and Electronic Engineer, vol. 53, no. 7.8, pp. 301–307, 1983.

[19] R. Cloet, S. Hurst, C. Edwards, P. Phillips, and A. Duncan, “A sideways-looking towed depth-measuring system,” Journal of Navigation, vol. 35, no. 03, pp. 411–420, 1982.

[20] H. Matsumoto, “Characteristics of seamarc ii phase data,” IEEE Journal of Oceanic Engineering, vol. 15, pp. 350–360, Oct 1990.

[21] P. Kraeutner and J. Bird, “Principal components array processing for swath acoustic mapping,” in OCEANS ’97. MTS/IEEE Conference Proceedings, vol. 2, pp. 1246–1254 vol.2, Oct 1997.

[22] P. Kraeutner and J. Bird, “Beyond interferometry, resolving multiple angles-of-arrival in swath bathymetric imaging,” in OCEANS ’99 MTS/IEEE Riding the Crest into the 21st Century, vol. 1, pp. 37–45 vol.1, Oct 1999.

[23] P. Kraeutner, Small Aperture Acoustic Imaging using Model Based Array Signal Processing. PhD thesis, Simon Fraser University, February 1998.

[24] J. Bird and P. Kraeutner, “Imaging methods and apparatus using model-based array signal processing,” Oct. 10 2000. US Patent 6,130,641.

[25] E. Weisstein, “Normal equation,” 2014.

[26] J. Bird and P. Kraeutner, “Cramer-rao bound investigation of swath bathymetry accuracy,” in OCEANS, 2001. MTS/IEEE Conference and Exhibition, vol. 3, pp. 1640–1647 vol.3, 2001.

[27] R. Dicke, “Object detection system,” January 1953. 2624876.

[28] C. Cooke, “The early history of pulse compression radar-the history of pulse compression at sperry gyroscope company,” Aerospace and Electronic Systems, IEEE Transactions on, vol. 24, pp. 825 –833, nov 1988.

[29] W. Siebert, “The early history of pulse compression radar-the development of an/fps-17 coded-pulse radar at lincoln laboratory,” Aerospace and Electronic Systems, IEEE Transactions on, vol. 24, pp. 833 –837, nov 1988.

[30] P. Stevenson and D. Hall, “Characteristic p-e and s-e relationships of hard pzt ceramics under high drive conditions,” in Applications of Ferroelectrics, 1996.

ISAF '96., Proceedings of the Tenth IEEE International Symposium on, vol. 1, pp. 313 –316 vol.1, aug 1996.

[31] R. Urick, Principles of Underwater Sound. New York, NY, USA: McGraw-Hill, 3rd ed., 1983.

[32] R. Barker, "Group synchronizing of binary digital systems," in Communication theory, pp. 273–287, 1953.

[33] K. Griep, J. Ritcey, and J. Burlingame, "Poly-phase codes and optimal filters for multiple user ranging," Aerospace and Electronic Systems, IEEE Transactions on, vol. 31, pp. 752 –767, april 1995.

[34] S. Zoraster, "Minimum peak range sidelobe filters for binary phase-coded waveforms," Aerospace and Electronic Systems, IEEE Transactions on, vol. AES-16, pp. 112 –115, jan. 1980.

[35] J. Cilliers and J. Smit, "Pulse compression sidelobe reduction by minimization of lp-norms," Aerospace and Electronic Systems, IEEE Transactions on, vol. 43, pp. 1238 –1247, july 2007.

[36] M. Cohen, M. Fox, and J. Baden, "Minimum peak sidelobe pulse compression codes," in Radar Conference, 1990., Record of the IEEE 1990 International, pp. 633 –638, may 1990.

[37] J. Jedwab, "What can be used instead of a barker sequence?," 2007.

[38] M. Golay, "Sieves for low autocorrelation binary sequences," Information Theory, IEEE Transactions on, vol. 23, pp. 43 – 51, jan 1977.

[39] P. Borwein, R. Ferguson, and J. Knauer, "The merit factor problem," Number theory and polynomials, p. 52, 2000.

[40] M. Amin Nasrabadi and M. Bastani, “A survey on the design of binary pulse compression codes with low autocorrelation,” 2010.

[41] R. Kristiansen, “On the aperiodic autocorrelation of binary sequences,” 2003.

[42] N. Levanon and E. Mozeson, Radar Signals. New York, NY, USA: Wiley, 1st ed., 2004.

[43] C. Nunn, “Constrained optimization applied to pulse compression codes and filters,” in Radar Conference, 2005 IEEE International, pp. 190 – 194, may 2005.

[44] R. Urick, Principles of Underwater Sound. 3rd ed., 1983.